ICNF2025 Abstracts

International Conference on Noise and Fluctuations

XXVII edition (June 17-20, 2025)

Taormina (ME), Italy

Preface

This document lists all abstracts accepted for presentation at the ICNF2025 conference in Taormina.

The eight (8) invited contributions are listed first (from INV01 to INV08).

Then we list the regular contributions, indexed based on the technical area, that is:

- BI - Biological Systems (from BI01 to BI08)
- CS - Circuits and Systems (from CS01 to CS04)
- ED - Electron Devices (from ED01 to ED13))
- IN- Instrumentation (from IN01 to IN05)
- MR – Materials and Reliability (from MR01 to MR03)
- QN – Quantum Noise and devices (from QN01 to QN08)
- TS-Theory and Stochastic Processes (from TS01 to TS05)

Index

Invited contributions

Biological Systems (BS)

Circuit and Systems (CS)

Electron Devices (ED)

Materials and Reliability (MR)

Quantum Noise and Devices (QN)

Theory and Stochastic Processes (TS)

Random Telegraph Noise Complexity Originates from Electrostatic Interactions and Defects Motion

Francesco Maria Puglisi

DIEF, Università di Modena e Reggio Emilia, Modena, Italy - francescomaria.puglisi@unimore.it

Abstract: Random Telegraph Noise (RTN) is known to show complex instabilities. Their origin is here traced back to the combination of *i*) the Coulomb interaction between defects due to trapped charge therein and ii) the defects' field-assisted motion. Strikingly, we observe that unstable RTN with complex time evolution, conventionally though to be involving several defects, can result from the activity of one single defect moving within the oxide.

Keywords: Random Telegraph Noise, Coulomb interaction, traps, defects, drift-diffusion, RRAM.

Introduction RTN is one of the most critical reliability issues in electron devices. Its typical switching between two (or more) current levels is attributed to charge trapping/de-trapping at defects [1]. Complex/unstable RTN has been reported and associated to Coulomb interactions between traps [1-2]. Here we show via Monte-Carlo physics-based simulations of HfO_2-based cells that charge trapping and defects motion together are the main source of RTN complexity. We show that significant instability can result from the motion of even just one defect and that complex RTN, observed in experiments and hard to analyze, is not due to the concurrent action of many defects, as commonly thought, but is explained by trapping/de-trapping at an individual defect moving in the dielectric under the action of the local field, in turn perturbed by trapped charge at other defects, resulting in a complex electrodynamic setup and, thus, complex RTN.

Simulations We performed kinetic Monte-Carlo (kMC) simulations on a TiN/(4nm)HfO_2/TiN cell (area = 25 nm^2 - Fig. 1a). Oxygen vacancies (V) and ions (O) are included being the main defects in HfO_2 [3], and are uniformly distributed in space and energy (Fig. 1b). In MIM cells, the overall leakage current is dominated by trap-assisted tunneling (TAT) at Vs (Fig. 2b), which can quickly capture/emit charges. Although Os (slower than Vs) do not contribute to leakage, trapped charge therein locally perturbs the potential and modulates leakage, promoting RTN. kMC 3D simulations were run using Ginestra® to simulate RTN including defects motion. The parameters used are in Fig. 1c, and are consistent with DFT values [4] that allow reproducing the switching characteristics and retention of RRAMs [5]. We include Schottky and thermionic emission, direct and Fowler-Nordheim tunneling, TAT with trap-to-trap contribution, and the trapped charge in the Poisson equation. In HfO_2, Os were shown both experimentally and by simulations [4] to move via interstitial jumps driven by electric field and temperature (V^+s motion is negligible due to their higher diffusion barrier [4]) and this mechanism is crucial in explaining switching in RRAMs [5]. The rate of the process [5] is:

$$R_D(x,y,z) = \nu_o e^{-\frac{E_{A,D} - k_D F_{EFF}(x,y,z)}{k_B T(x,y,z)}}$$

with F_{EFF} the electric field at the defect. At each instant of time, R_D probabilistically determines if a defect motion event is to happen. To picture the effect of defect motion on RTN, we labeled each instant at which any defect motion is detected as t_1, …, t_n, Thus, we identified n windows, each with a given length (Δt_1, …, Δt_n) and defects spatial configuration (C_1, …, C_n).

Results First, we performed a simulation of the cell in Fig. 1a, that includes four Os and a handful of Vs, without including defect motion. We observed a 4-level RTN which corresponds to the modulation of the TAT (driven by Vs) induced by charge capture/emission at O#1 and #2 (Fig. 2a). O#3 and #4 do not contribute as their average τ_c or τ_e are larger than the simulation

time. The simulated RTN shows no instabilities since, though defects interact with each other and modulate TAT, the number of all possible defects charge configurations cannot change over time as defects do not move. Since RTN properties (ΔI, τ_c, τ_e) strongly depend on the mutual distance between traps, when defects motion is included (Fig. 2b) such properties will change in a complex way according to the evolution of the defects spatial configuration. Usually, a complex RTN trace like that in Fig. 2b is associated to the overlapped action of many slow defects (O, in this case), since the RTN shows many distinct current levels. From the analysis of the RTN signal we identified 28 O motion events each determining a certain configuration of defects persisting for a given time window and associated with a specific RTN behavior. In Fig. 3, we show the RTN chunks in window 10 and 27, in which the change in RTN properties is clear. Defying common thinking, the time domain analysis of the charge states of O^0 #1 and #2 (Fig. 3) reveals that RTN in both windows is caused by the same O (#2). In Fig. 3 we depicted the 2D potential along the horizontal planes passing through the V that is responsible for most of the total leakage, for window 10 and 27. When O#2 is closer to such V (window 10), the local potential at that V is lower, causing a severe perturbation of the RTN properties [6].

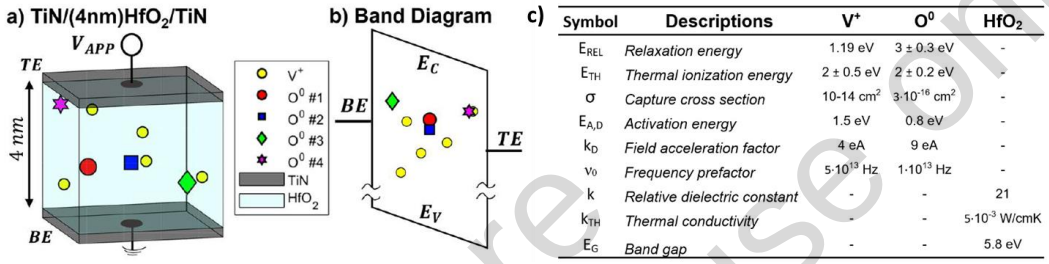

Symbol	Descriptions	V^+	O^0	HfO_2
E_{REL}	*Relaxation energy*	1.19 eV	3 ± 0.3 eV	-
E_{TH}	*Thermal ionization energy*	2 ± 0.5 eV	2 ± 0.2 eV	-
σ	*Capture cross section*	10-14 cm^2	$3 \cdot 10^{-16}$ cm^2	-
$E_{A,D}$	*Activation energy*	1.5 eV	0.8 eV	-
k_D	*Field acceleration factor*	4 eA	9 eA	-
ν_0	*Frequency prefactor*	$5 \cdot 10^{13}$ Hz	$1 \cdot 10^{13}$ Hz	-
k	*Relative dielectric constant*	-	-	21
k_{TH}	*Thermal conductivity*	-	-	$5 \cdot 10^{-3}$ W/cmK
E_G	*Band gap*	-	-	5.8 eV

Fig. 1(a) MIM structure employed for kMC simulations and (b) its band diagram. Main defects and materials parameters used in simulations taken from [R] and references therein.

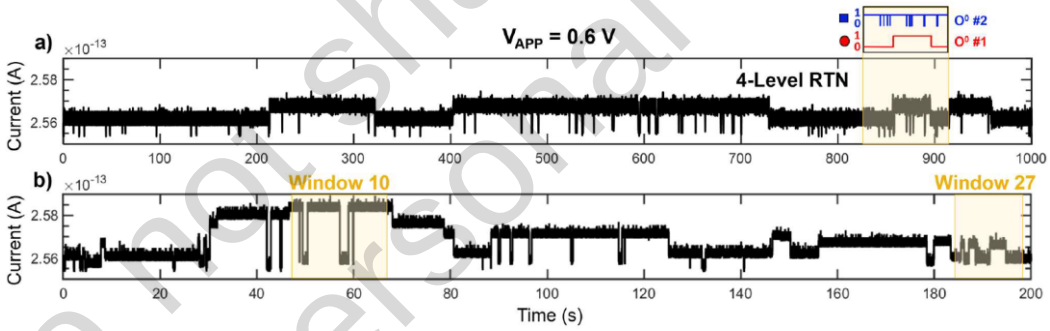

Fig. 2: Simulated RTN w/o (a) and w/ (b) defects motion. Yellow bands in (b) highlight window 10 and 27.

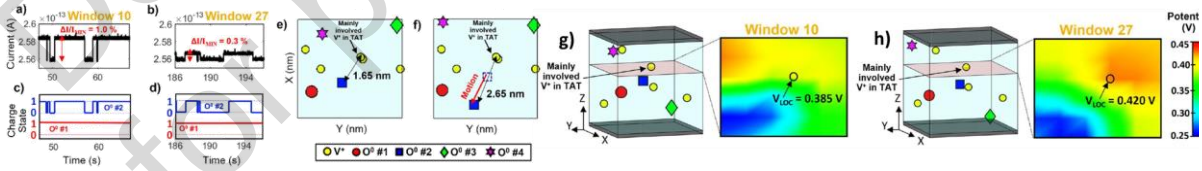

Fig. 3: RTN chunks in window 10 (a) and 27 (b), along with their respective O charge states (c) and (d), their XY views (e) and (f), and their horizontal plane 2D potential maps (g) and (h).

Acknowledgments S. Vecchi (Applied Materials) is acknowledged for critical simulations results.

References

[1] F. M. Puglisi et al., IEEE T-ED, vol. 62, no. 8, pp. 2606–2613, 2015.
[2] F. M. Puglisi et al., Solid. State. Electron., vol. 125, pp. 204–213, 2016.
[3] L. Vandelli et al., IEEE T-ED, vol. 58, no. 9, pp. 2878–2887, 2011.
[4] A. S. Foster et al., Phys. Rev. Lett., vol. 89, no. 22, 2002.
[5] A. Padovani et al., IEEE T-ED, vol. 62, no. 6, pp. 1998–2006.
[6] S. Vecchi et al., ESSDERC 2022, Milan, Italy, 2022, pp. 368-371.

Modeling and Predicting Noise-Induced Failure Rates in Ultra-Low-Voltage SRAM Bitcells Affected by Process Variations

L. Van Brandt[1], M. Bonnin[2], M. Banaszeski da Silva[3], P. Bolcato[4], G. Wirth[5], D. Flandre[1] and J.-C. Delvenne[1]

[1]ICTEAM Institute, UCLouvain, Louvain-la-Neuve, Belgium

[2]Department of Electronics and Telecommunications, Politecnico di Torino, Turin, Italy

[3]Department of Electronics and Computing, Universidade Federal de Santa Maria, Santa Maria, Brazil

[4]Siemens DISW-ICS-CICV, Meylan, France

[5]Electrical Engineering Department, Universidade Federal do Rio Grande do Sul, Porto Alegre, Brazil

leopold.vanbrandt@uclouvain.be

Abstract: Stability of ultra-low-voltage SRAM bitcells in retention mode is threatened by two types of uncertainty: process variability and intrinsic noise. We assess their combined effects with SPICE transient noise simulations. A predictive stochastic nonlinear model, fully characterizable from conventional deterministic SPICE simulations, is presented and exploited.
Keywords: Ultra-Low-Voltage SRAM, Noise-Induced Failures, Stochastic Modeling

Introduction The functionality of SRAM bitcells must be statistically guaranteed and thereby predicted. We study the combined effects of process variations and noise in a unified SPICE simulation framework. We present a general stochastic model of nonlinear bistable systems, leveraged to analytically calculate the *mean transition time* or *time to failure* ($MTTF$).

Transient Noise Simulations and Bit Flips
One typical transient simulation of a bit-flip caused byy intrinsic transistor noise is shown in Figure 1(a). The bit-flip mechanism in SRAM bitcells is better understood within the mathematical formalism of nonlinear dynamical systems (state space depicted in Figure 1(b)).

Stochastic Nonlinear Dynamical Modeling
An SRAM bitcell in retention is assimilated to an autonomous stochastic nonlinear dynamical system, with stochastic state-space representation (to be understood in Itô's sense):

$$\frac{\mathrm{d}\boldsymbol{v}}{\mathrm{d}t} = \boldsymbol{h}(\boldsymbol{v}) + \boldsymbol{\sigma}(\boldsymbol{v})\boldsymbol{w}(t). \tag{1}$$

Extended Eyring-Kramers Formula, Results and Discussion

$$MTTF \approx 2\pi\sqrt{\tau_0\,\tau_{\mathrm{M}}}\,\frac{\sigma_0}{\sigma_{\mathrm{M}}}\,\exp\left(\frac{\mathcal{U}(\Delta\tilde{v})}{\frac{1}{2}\sigma_{\mathrm{M}}^2}\right)\exp\left(-2\left(\frac{1}{\sigma_{\mathrm{M}}^2}-\frac{1}{\sigma_0^2}\right)\overline{\mathcal{U}}\right) \tag{2}$$

has been used to predict the noise-induced transition rate ($1/MTTF$), accounting for both nonlinear SRAM dynamics and state-dependent noise intensity and hence has shown high accuracy (Figure 2). All the quantities involved in (1) and (2) are explained in the reference.

(a)

(b)

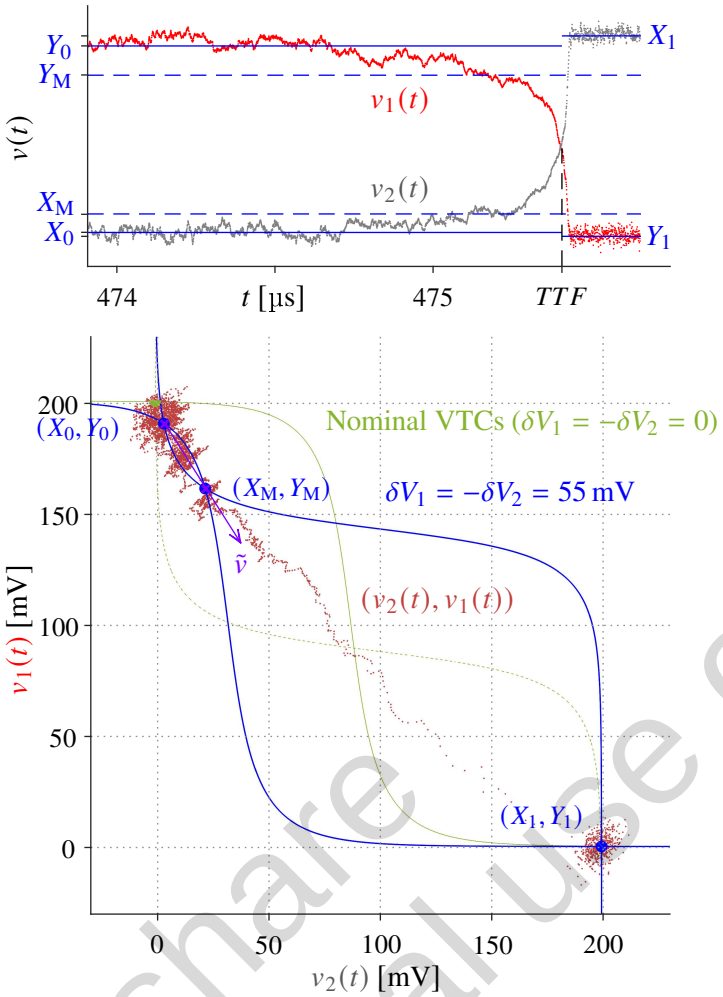

Figure 1: (a) Transient simulation of a noise-induced bit flip (failure) in the 6T SRAM bitcell (under process variations) in retention. (b) State trajectory of the bit flip of (a) in the state space.

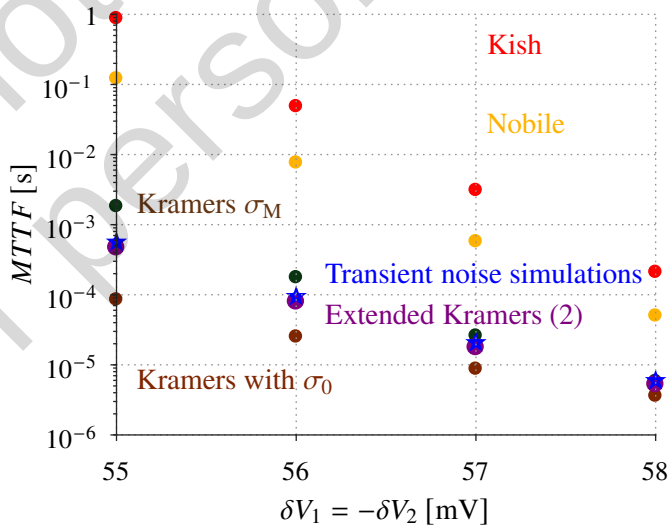

Figure 2: $MTTF$ empirically estimated from transient noise simulations (like Figure 1(a)) compared to the predictions of the analytical formulas.

Reference

L. Van Brandt *et al.*, "Modeling and Predicting Noise-Induced Failure Rates in Ultra-Low-Voltage SRAM Bitcells Affected by Process Variations". *IEEE Transactions on Circuits and Systems I: Regular Papers*, Volume 72, Issue 3, March 2025, pp. 989 - 1002.

Investigating anyon fractional statistics via noise measurements

M. Ruelle[1], H. Bartolomei[1], M. Kumar[1], E. Frigerio[1], E. Baudin[1], J.-M. Berroir[1], B. Plaçais[1], A. Cavanna[2], U. Gennser[2], Y. Jin[2], G. Ménard[1], G. Feve[1]

[1]Laboratoire de Physique de l'Ecole Normale Supérieure, ENS, Université PSL, CNRS, Sorbonne Université, Université paris Cité, F-75005 Paris, France
[2]Centre de Nanosciences et de Nanotechnologies (C2N), CNRS, Université Paris-Saclay, 91120 Palaiseau, France
email address : gwendal.feve@phys.ens.fr

Abstract: We investigate the fractional statistics of anyons in a fractional quantum Hall conductor by performing noise measurements at the output of a quantum point contact (QPC). Generating a dilute beam of anyons towards a QPC, we observe negative cross-correlations of the current fluctuations, which is a signature of a bunching mechanism specific to anyons. By measuring quantitatively the evolution of the cross-correlations with the emitted anyon current, we confirm the value of the exchange phase of $\pi/3$ for anyons at the filling factor 1/3.

Keywords: Anyons, Quantum Hall effect, Fractional statistics, Braiding phase

Anyons are quasiparticles obeying fractional statistics, in between bosons and fermions, that arise in two-dimensional systems [1,2]. The fractional statistics implies that when moving an anyon adiabatically in a loop around a second one (a process called a braiding operation), the wavefunction describing the system acquires a non-trivial braiding phase. Experimentally, anyons appear as the elementary excitations of fractional quantum Hall (FQH) fluids, topological phases emerging when a strong perpendicular magnetic field is applied to a two-dimensional electron gas. In such phases, the bulk of the material becomes insulating and electronic transport occurs through chiral and ballistic one-dimensional edge channels. Tunneling between opposite edge channels can take place at a quantum point contact (QPC), a constriction of the FQH fluid that is implemented using metallic gates deposited on top of the electron gas. For anyons, the dominant mechanism for particle transfer is not the direct tunneling of the incoming excitations, but rather a time-domain braiding process between the incoming excitations and particle-hole excitations created at the QPC [3,4,5].

I will present how anyon braiding can be probed from the measurement of current noise correlations [6,7,8]. Noise measurements at the output of a partitioner (here the QPC), a technique also called two-particle interferometry, has been used to probe the tendency of particles to aggregate in larger packets (bunching) or on the contrary to exclude each others (antibunching). I will show that when a dilute stream of anyons is emitted towards a QPC, a specific bunching mechanism shows up that is directly related to the braiding properties of anyons. This anyon bunching results in the observation of negative cross-correlations of the current fluctuations at the output of the QPC. These negative cross-correlations not only illustrate the braiding properties of anyons but they can also be used to determine quantitatively the anyon braiding phase [6,7,8,9,10], which we find to be equal to $2\pi/3$ for the FQH state at filling 1/3, as predicted [6]. In contrast, when electrons (fermions) are generated towards the QPC, conventional fermionic antibunching is observed resulting in the suppression of the output current correlations.

References

[1] B. I. Halperin, Phys. Rev. Lett. **52**, 1583–1586 (1984).
[2] D. Arovas, J. R. Schrieffer, F. Wilczek, Phys. Rev. Lett. **53**, 722–723 (1984).
[3] Lee, JY.M., Sim, HS, Nature Communications **13**, 6660 (2022).
[4] J.Y. Lee, C. Han, H.S. Sim, Phys. Rev. Lett. **125**, 196802 (2020)
[5] C. Mora, arXiv:2212.05123 (2022)
[6] B. Rosenow, I. P. Levkivskyi, B. I. Halperin, Phys. Rev. Lett. **116**, 156802 (2016).
[7] H. Bartolomei et al. Science **368**, 173-177 (2020).
[8] M. Ruelle et al., Phys. Rev. X **13**, 011031 (2023).
[9] P. Glidic et al., Phys. Rev. X **13**, 011030 (2023).
[10] J.-Y. M. Lee et al., Nature 617, 277 (2023).

Monitoring charge noise in superconducting circuits via photon emission

Joachim Ankerhold

Institute for Complex Quantum Systems and IQST, Ulm University, Germany
joachim.ankerhold@uni-ulm.de

Abstract: Recently, in extending set-ups of circuit quantum electrodynamics (cQED), superconducting devices combining dc-voltage biased Josephson junctions and microwave cavities have turned out as versatile and remarkably simple platforms to explore light-matter interaction (Josephson Photonics). The emission of microwave photons directly reflects the statistics of charge carriers and thus offers elegant means to monitor charge noise which is notoriously difficult to access otherwise. Stabilizing phase diffusion via injection locking provides another interesting setting, where phase slips arise and leave their imprint in the radiation. I will provide an overview of the theoretical framework and discuss recent developments.

Keywords: Quantum noise, superconducting circuits, Josephson photonics, quantum bits

Quantum Supremacy Challenged: Instantaneous Noise-based Logic

Nasir Kenarangui, Arthur Powalka and Laszlo B. Kish

Department of Electrical and Computer Engineering, Texas A&M University, College Station, TX 77843-3128, USA

INVITED TALK

Abstract: Instantaneous Noise-Based Logic (INBL) has emerged as a classical alternative to quantum computing, challenging the concept of "quantum supremacy" without the need for quantum hardware. INBL demonstrates an exponential increase in computational power, similar to quantum computers, with a factor of O(2^*M*) growth in computing speed (*M* is the number of physical qubits), at the same order of hardware complexity. We discuss three applications, including exponential phonebook searches (number or name lookup) and the Deutsch-Jozsa quantum algorithm, as illustrations.

Keywords: Product of noises, superposition, Hilbert space, random telegraph waves.

Introduction The term "quantum supremacy" refers to the theoretical advantage that quantum computers hold over traditional, classical computers (based on the Turing machine model) for certain complex computational tasks. Specifically, quantum supremacy occurs when a quantum computer can solve a particular, challenging mathematical problem significantly (typically exponentially) faster than its classical counterpart. In such cases, the resources (hardware capacity and/or processing time) required by a classical computer increase exponentially compared to those needed by a quantum computer for the same task.

While we have been awaiting to see the realization of universal gate-based quantum computers leading to a factor of 2^N increase in computation speed at a given hardware complexity, the ongoing efforts to challenge quantum supremacy claims have led to a dynamic competition between quantum and classical computing algorithms. Classical algorithms have made significant strides in recent years, narrowing the gap with quantum computers and even surpassing some quantum supremacy claims [1-5].

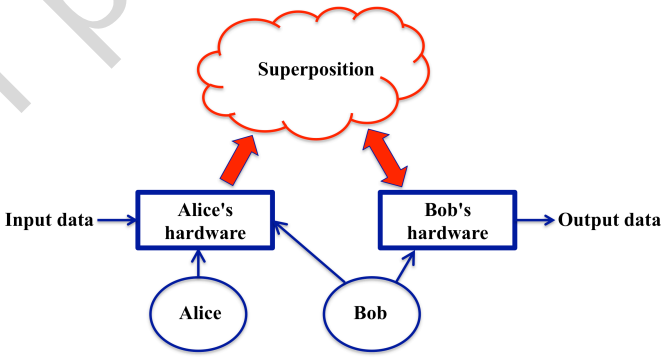

Fig. 1: Quantum computer scheme.

Figure 1 shows the outline of a generic quantum computer and its operation in a problem *implementer* (Alice) and *solver* (Bob) fashion. Alice implements the problem in the quantum computer and at certain tasks she may need a complexity that is exponential in *M* (e.g. when

filling in exponentially large, $N=2^M$, arbitrary databases). Depending on the input, she sets up the superposition with her hardware that provides the initial and boundary conditions for the wavefunction carrying the superposition that represents the data. Bob carries out the computation to solve the problem and does the measurements to output the results. He may execute the operations on the superposition by using some of the hardware components of Alice and his own extra hardware. The important feature of a useful quantum processor is that Bob's required computational complexity to obtain the results is only polynomial-in-M.

Noise-based logic (NBL) The noise-based logic implementation of the problem has similar features, except that the superposition is classical, moreover nonlinear processes (products) and a true random number generator are also involved in the process, see Figs 1,2.

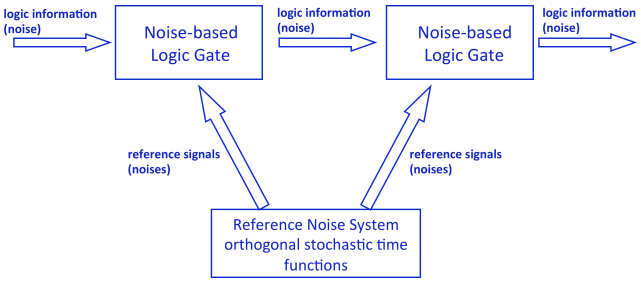

Fig. 2: Generic NBL scheme. The reference noises are distributed all over the system

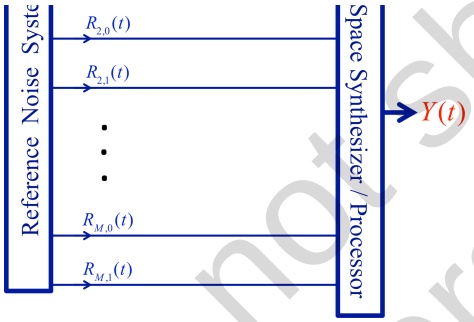

Fig. 3: The setup of the INBL scheme. Operations on the exponential superposition $Y(t)$ and the references noises $R_{i,j}(t)$.

Figure 3 shows Polynomial circuit illustration of the logic structure of the generic superposition synthesizer of Instantaneous Noise Based Logic. The output represents a superposition of $O(2^M)$ orthogonal product strings of random telegraph waves. We discuss three applications, where exponential speed increase is reached in a deterministic computing fashion [6-8].

References

[1] S. Chen, "Quantum Advantage Showdowns Have No Clear Winners", Wired, July 11, 2022, https://www.wired.com/story/quantum-advantage-showdowns-have-no-clear-winners/ .
[2] R. Brierley "Not so fast", Nature Phys. 17, 2021, 1073. https://www.nature.com/articles/s41567-021-01388-9
[3] E. Tang, "Quantum Principal Component Analysis Only Achieves an Exponential Speedup Because of Its State Preparation Assumptions", Phys. Rev. Lett. 127, 2021, 060503.
[4] E. Tang "A Quantum-Inspired Classical Algorithm for Recommendation Systems", Proc. of the 51st Annual ACM SIGACT Symposium on Theory of Computing, STOC 2019, 2019, 217–228. https://doi.org/10.1145/3313276.3316310

[5] M. Sparkes, "Google's claim of quantum supremacy has been completely smashed", New Scientist, July 3, 2024, https://www.newscientist.com/article/2437886-googles-claim-of-quantum-supremacy-has-been-completely-smashed/ .
[6] L.B. Kish, ""Quantum supremacy" revisited: Low-complexity, deterministic solutions of the original Deutsch-Jozsa problem in classical physical systems", R. Soc. Open Sci. 10, 2023, 221327, https://doi.org/10.1098/rsos.221327 ; arXiv:2210.07088
[7] L.B. Kish, W.C. Daugherity, "Entanglement, and Unsorted Database Search in Noise-Based Logic", Applied Sciences 9 (2019) 3029; open access: https://www.mdpi.com/2076-3417/9/15/3029/htm
[8] B. Zhang, L.B. Kish, C.G. Granqvist, "Drawing from hats by noise-based logic", International Journal of Parallel, Emergent and Distributed Systems 32 (2017), 244-251, http://dx.doi.org/10.1080/17445760.2016.1140168 ; http://arxiv.org/abs/1511.03552

The role of noise in biological systems: Using noise for overcoming malfunctions in biological systems

Yaron Ilan M.D.
Professor of Medicine, Faculty of Medicine, Hebrew University
Chairman, Department of Medicine, Hadassah Medical Center
Jerusalem, Israel

Noise is an essential part of the normal functioning of complex biological systems and is necessary for their proper operation. Biological systems are unpredictable due to the interactions among genes, proteins, and environmental factors. All biological processes are somewhat disordered: biochemical reactions are inherently random, leading to variations in the production of mRNAs and proteins. The variability in molecular traits comes from a mix of processes that amplify or reduce randomness. Defining, accurately measuring, and understanding cell-to-cell variation's random and predictable parts is challenging. The Constrained Disorder Principle (CDP) explains biological systems based on their inherent variability, bounded by dynamic boundaries that change in response to internal and external perturbations. Inter and intra-subject variability characterize all biological systems, making it difficult to provide a single diagnostic and therapeutic regimen to all patients and even the same patients over time. The dynamicity of the variability is also a significant challenge for personalizing therapies. The CDP-based second-generation artificial intelligence system is an outcome-based dynamic platform that incorporates personalized variability signatures into the therapeutic regimens and provides methods for improving the response and overcoming the loss of response to treatments. The signatures of the biological variabilities offer a method for identifying new biomarkers for early diagnosis, monitoring chronic disease, and evaluating the response to therapies.

Low-frequency noise in gas sensors

Wonjun Shin[1*]

[1]Department of Semiconductor Convergence Engineering, Sungkyunkwan University, Suwon 16419, Republic of Korea (swj0107@snu.ac.kr)

Low-frequency noise (LFN) has emerged as a critical factor in determining the detection limit, stability, and reliability of modern gas sensors. Although extensive efforts have been made to enhance the response, sensitivity, and selectivity of gas sensors by exploring various sensing materials and device architectures, systematic research on LFN remains comparatively limited. This work focuses on two pivotal aspects that govern LFN characteristics: (1) the intrinsic properties of the sensing material and (2) the type of sensor platform.

Sensing materials employed in gas sensors exhibit a wide range of electrical and physicochemical properties, which profoundly affect LFN generation mechanisms. For resistor-type gas sensors, where current passes directly through the sensing layer, amorphous or polycrystalline metal oxides often display large $1/f$ noise due to the abundance of grain boundaries and bulk defects. These defects can trap and release carriers, leading to significant current fluctuations in the low-frequency domain. In contrast, materials such as conducting polymers may experience adsorption–desorption noise that intensifies or diminishes in response to specific gas environments, thereby altering both the magnitude and spectral shape of the LFN. Two-dimensional materials—including graphene and transition-metal dichalcogenides—can exhibit even larger noise components arising from their high surface-to-volume ratio, as surface adsorption plays a dominant role in carrier fluctuations. Consequently, the choice and processing conditions (e.g., sputtering ambience, annealing temperature) of the sensing material are central to managing LFN, since these steps determine the density of defects, grain sizes, and surface adsorption kinetics.

Apart from the sensing material itself, the sensor platform architecture exerts a decisive influence on LFN (Fig. 1). In resistor-type gas sensors, any fluctuation caused by the sensing material (surface adsorption, bulk carrier recombination, interface states) directly translates into output noise. Moreover, if metal–semiconductor contacts form significant Schottky barriers, contact noise can become the dominant source of LFN. By contrast, thin-film transistor (TFT)-type sensors offer a gate-tunable conduction channel. Here, the LFN may originate primarily from channel–oxide interface traps (carrier number fluctuation) or grain boundary scattering in the semiconductor channel (mobility fluctuation), depending on the device's conduction mechanism. Finally, in horizontal floating-gate FET (HFGFET)-type sensors, the sensing material is physically separated from the transistor channel, effectively isolating the conduction in the FET from the noisy adsorptive processes. In systems where the sensing layer features significant resistance (e.g., WO_3), the local RC network can introduce Lorentzian-like noise components, making the LFN profile sensitive to gas adsorption kinetics.

Overall, LFN in gas sensors reflects an interplay between the innate properties of the sensing material and the architecture of the sensor platform (Table 1). Achieving optimal signal-to-noise ratios and low detection limits demands not only improved sensing materials with reduced defect densities but also careful engineering of the device structure to minimize or exploit LFN as needed. Consequently, a comprehensive understanding of both material-specific and platform-specific noise mechanisms is essential for next-generation gas sensors capable of highly sensitive, selective, and stable operation.

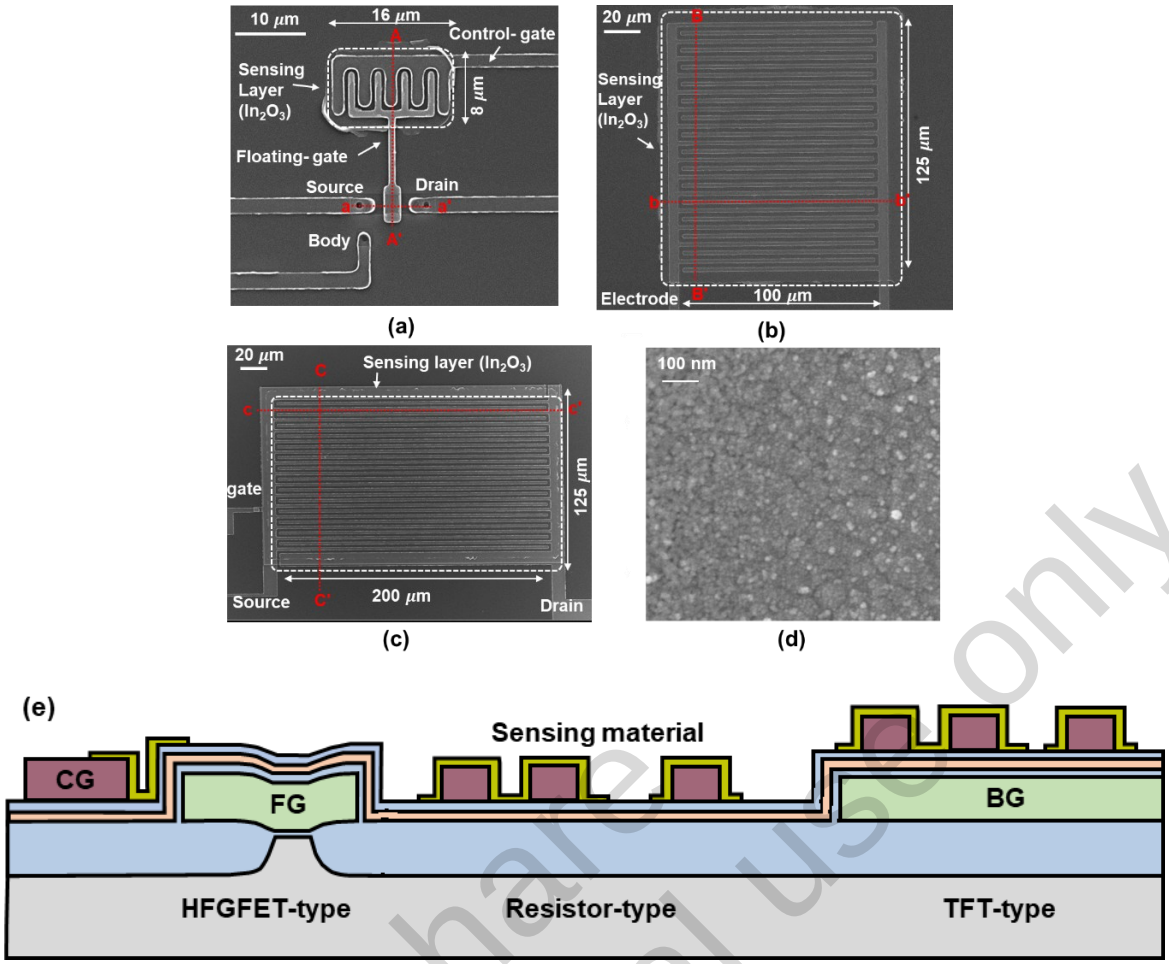

Fig. 1. Top SEM image of the (a) HFGFET-type, (b) resistor-type, and (c) TFT-type gas sensors fabricated on the same wafer. (d) Top SEM image of the sensing material. (e) Schematic illustration of the sensors.

Sensor type	Sensor structure	Characteristics	Noise generation mechanism	Notes related to noise
Resistor-type	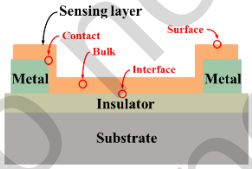	• A two-terminal device • Sensing material is used as a conductive channel	• Carrier number/mobility fluctuation at the bulk and surface of sensing material • Adsorption/desorption noise by gas molecules at the surface of sensing material • Potential barrier height fluctuation at metal-semiconductor (sensing material) contact	• Large noise magnitude • LFN characteristics highly affected by the sensing material deposition conditions and structures
TFT-type	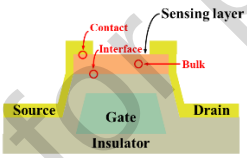	• A three-terminal device (Source, drain, and gate) • Sensing material is used as a conductive channel • Conductivity can be modulated by gate bias	• Carrier number fluctuation at the interface between gate insulator and sensing material • Carrier mobility fluctuation at the bulk of sensing material	• Large noise magnitude • LFN characteristics highly affected by the sensing material deposition conditions and interface quality between the sensing material and gate oxide
HFGFET-type	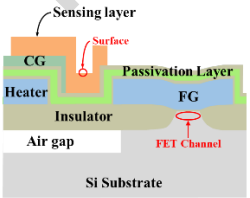	• A four-terminal device (Source, drain, body, and gate) • Sensing material and FET transducer is separated • Voltage applied to CG voltage is coupled to FG through the sensing material	• Carrier number/mobility fluctuation at the FET channel • Coupling voltage (CG to FG) fluctuation at the sensing material	• Low noise • LFN characteristics affected by FET channel (low resistance sensing materials) and sensing material deposition conditions (high resistance sensing materials) • Further reduction of LFN by optimizing the transducer (buried channel structure)

Table 1 Summary of representative sensor platforms (Resistor-type, TFT-type, and HFGFET-type), indicating potential origins of low-frequency noise (red circles) and corresponding noise generation mechanisms.

Environmental noise challenges for the Virgo detector

Maria Concetta Tringali[1], Vincenzo Dattilo[1], Irene Fiori[1], Federico Paoletti[2],

[1]European Gravitational Observatory (EGO), I-56021 Cascina, Pisa, Italy

[2]INFN, Sezione di Pisa, I-56127 Pisa, Italy

maria.tringali@ego-gw.it

Abstract - The Virgo interferometer is part of the international gravitational wave detector network and requires extreme sensitivity to detect spacetime distortions from astrophysical events. Environmental noise originating from natural and human-made sources poses a major challenge, especially in the low-frequency band. These disturbances can couple into the detector via seismic, acoustic, or electromagnetic paths. Virgo employs extensive environmental monitoring and mitigation strategies, including noise search campaigns and site protection. This contribution summarizes key environmental noise sources, coupling mechanisms, and the actions taken to preserve interferometer performance efforts that are crucial for current observations and future detectors.

Keywords: gravitational waves, interferometer, environmental noise, seismic noise, acoustic noise, infrastructure noise

Introduction - Gravitational waves (GWs), predicted by Einstein's General Theory of Relativity, are ripples in spacetime generated by accelerated massive objects such as compact binary coalescences or supernovae. Since 2015, their direct detection has opened a new era of observational astronomy. The Virgo interferometer [1], located near Pisa (Italy), is a 3-km-long laser Michelson interferometer that, together with LIGO [2] and KAGRA [3], forms a worldwide network of GW observatories. Detecting a GW requires measuring differential arm length variations smaller than 10^{-19} m, a technological challenge that demands extreme isolation from all forms of noise. Among the various limitations affecting the detector sensitivity, environmental noise plays a major role, especially in the low-frequency band (< 100 Hz), which is crucial for detecting signals from coalescence of binary compact objects and other astrophysical sources.

Figure 1: Aerial view of the Virgo gravitational wave interferometer.

Environmental Noise at Virgo - Environmental noise at the Virgo site originates from both natural and anthropogenic sources. Natural contributions include seismic ground motion (e.g. oceanic microseisms), wind, thunderstorms, and geomagnetic activity. Anthropogenic noise sources include road traffic, construction works, industrial operations, and observatory site infrastructure like HVAC systems, vacuum pumps, and electronic equipments [4]. These disturbances can affect the detector sensitivity by coupling through seismic, acoustic, and electromagnetic paths. Even sources several kilometers away, such as wind farms or elevated highways, can produce detectable signals close to the detector. To track these effects, Virgo uses an extensive network of environmental sensors, including seismometers, microphones, magnetometers, weather stations, and slow probes. This monitoring infrastructure is essential for diagnosing anomalies and guiding mitigation strategies [5].

Case Studies - Several notable cases highlight the impact of environmental noise on Virgo's operation. During the O3 observing run, high wind speeds and intense sea activity were correlated with increased low-frequency noise and a reduction in detector duty cycle. Wind speeds above 50 km/h, for example, were associated with a >4 Mpc drop in the Binary Neutron Star (BNS) detection range . Lightning strikes also generate broadband electromagnetic transients that are detected by magnetometers and produce sharp glitches in the GW channel. These disturbances excited mechanical resonances of the mirror suspensions, leading to a minute-long loss in sensitivity [6]. Anthropogenic sources such as heavy vehicles and nearby excavation work have also been shown to increase seismic noise in the 1–10 Hz range [7].

Toward a Quieter Site - Preserving a low-noise environment is a long-term goal for Virgo. Virgo has implemented targeted interventions to mitigate the infrastructure noise: vibration isolation for HVAC units, replacement of noisy fans, use of acoustic dampers, and optimization of infrastructure layout to avoid direct seismic paths. Agreements with the Italian Air Force have established permanent no-fly zones over the site. Environmental impact studies and negotiations with local stakeholders help to manage industrial activities and future developments around the detector.

Conclusions - Environmental noise represents a significant challenge in the quest to detect gravitational waves. Understanding and mitigating its effects is essential to improving the sensitivity and robustness of the Virgo interferometer. The ongoing efforts in monitoring, characterization, and site protection provide a valuable foundation for the future of gravitational wave astronomy.

References

1. Virgo Collaboration, "Advanced Virgo: a second-generation interferometric gravitational wave detector", Classical and Quantum Gravity, 2014, 32, 2, 024001.
2. LIGO Scientific Collaboration, "Advanced LIGO", Classical and Quantum Gravity, 2015, 32, 7, 074001.
3. KAGRA Collaboration, "Interferometer design of the KAGRA gravitational wave detector", Phys. Rev. D, 2013, 88, 4, 043007
4. Fiori, I. et al, "Environmental Noise in Gravitational-Wave Interferometers", Handbook of Gravitational Wave Astronomy. Springer, Singapore, 2022.
5. Fiori I. et al., "The Hunt for Environmental Noise in Virgo during the Third Observing Run", Galaxies. 2020; 8(4):82.
6. F Acernese et al, "The Virgo O3 run and the impact of the environment", 2022 Class. Quantum Grav. 39 235009.
7. Ruggi P., "Excavator injecting noise near the central building", https://logbook.virgo-gw.eu/virgo/?r=48311

Towards Sensing Protein Interactions and Dynamics via 1/f Noise in Graphene Field-Effect Transistors

M. Fomin[1], F. Steinbach[1], D. Pustovyi[2], N. Füllbrunn[3], K. Tanzusch[3], C. You[3], C. Ungermann[3], S. Vitusevich[2], M. Petrychuk[2], C. Meyer[1]

[1]School of Mathematics/Computer Science/Physics, Institute of Physics, University of Osnabrück, Germany
[2]Institute of Biological Information Processing (IBI-3), Forschungszentrum Jülich, Jülich, Germany
[3]Department of Biology/Chemistry and Center of Cellular Nanoanalytics, University of Osnabrück, Germany
email address: fsteinbach@uni-osnabrueck.de

Abstract: Graphene-based field-effect transistors (GFETs) offer a highly sensitive platform for detecting biomolecular interactions. We investigate how the protein dynamics influence the flicker (1/f) noise of GFETs. By functionalizing the graphene surface with a DOPC lipid monolayer, Ypt7 and the HOPS tethering complex, we register distinct changes in the 1/f noise spectrum. In yeast cells, Ypt7 is recruited to vacuoles and binds the HOPS complex to mediate membrane fusion. Ypt7 immobilization significantly increased the noise, while subsequent HOPS binding considerably reduced 1/f noise almost to its initial level, reflecting altered dynamic properties. These findings demonstrate that 1/f noise spectroscopy provides valuable insights into protein interactions, offering a label-free, real-time method for biosensing applications.

Keywords: GFET, 1/f noise, Ypt7, HOPS complex, biosensors, charge carrier fluctuation

Introduction Graphene-based field-effect transistors (GFETs) offer an ultra-sensitive platform for biosensing and for detecting molecular interactions [1]. Usually, molecular interactions are investigated by measuring changes in drain current as a result of the gate voltage response due to the attachment/detachment of proteins or due to conformational changes of the attached protein. It should be emphasized that the function of proteins is often governed by their dynamics. In this work, we present our results on transport and noise properties of GFETs with proteins demonstrating a novel approach to study protein interactions using the 1/f noise power spectral density of the GFETs.

Materials and methods The fabrication process and characterization of liquid-gated GFET devices are described in detail in [2]. To prevent desintegration of proteins due to strong hydrophobic interactions, we form a monolayer of 1,2-dioleoyl-sn-glycero-3-phosphocholine (DOPC) lipids on the graphene surface (Fig. la). Subsequently we introduce Ypt7 in its GTP-bound active state into the lipid monolayer (Fig. lb). As the last step, we add a protein complex (HOPS), that is recruited and bound by Ypt7 (Fig. le).

For electrical characterization, current-voltage (I-V) transfer characteristics were measured to evaluate the transistor behavior after each functionalization step. Low-frequency noise spectra were measured using a low-noise amplifier and a spectrum analyzer, with the devices biased in a liquid-gated configuration. The power spectral density of the voltage fluctuations was recorded in a frequency range from 1 Hz to 10 kHz.

Results and discussion I-V transfer characteristics and noise spectroscopy were used for monitoring molecular adsorption effects. It is shown that the lipid monolayer had very small influence on the charge neutrality point (CNP), confirming its zwitterionic nature. At the same

time a drop in transconductance was registered, suggesting minor modifications to charge transport properties.

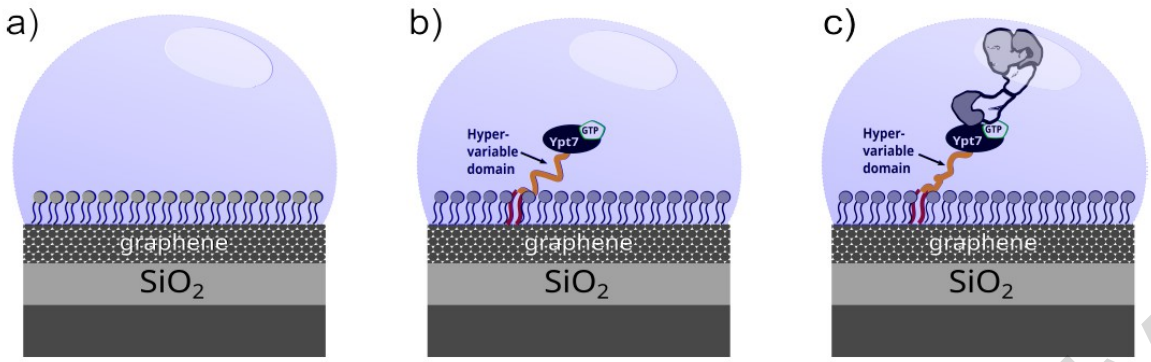

Figure 1: Schematic representation of the stepwise functionalization of the graphene-based field-effect transistor (GFET) biosensor. (a) Formation of a lipid monolayer (DOPC) on the graphene surface. (b) Immobilization of Ypt7, interacting with the lipid mono layer. (c) Binding of the HOPS complex to Ypt7, leading to conformational changes affecting the charge carrier dynamics in the graphene channel.

Simultaneously, the normalized noise spectral density S_I/I^2 increased slightly, which can be explained considering the additional capacitance introduced by the lipid layer. Upon Ypt7 immobilization, a substantial rise in 1/f noise was recorded, with a small shift in CNP and a partial transconductance recovery. The subsequent addition of HOPS led to a significant reduction in 1/f noise, restoring it to levels similar to the lipid-functionalized state. This suggests that HOPS binding influences Ypt7's dynamics in a way that protein properties can be studied using charge or mobility fluctuations depending on the underlying mechanism.

The observed changes in 1/f noise provide insight into how protein dynamic processes modulate the response signal of the graphene channel. While shifts in the charge neutrality point (CNP) were minimal, highlighting that the CNP position is less sensitive for sensing in this context, significant changes in noise spectra were detected. The pronounced increase in noise after Ypt7 attachment indicates enhanced dynamic charge exchange activity. Despite the short Debye length imposed by the HEPES buffer, and the fact that the HOPS complex resides outside this range, its binding resulted in a decrease of the power spectral density of the noise by more than one order of magnitude. This suggests that changes of protein dynamics are transduced to the graphene surface. These findings underscore the potential of noise spectroscopy for monitoring protein interactions without external labeling, offering sensitivity to biomolecular processes that extend beyond traditional electrostatic sensing mechanisms.

Conclusion This study highlights the capability of 1/f noise analysis in GFET-based biosensors to detect and characterize biomolecular interactions. The registered changes in the noise spectra upon Ypt7 functionalization and HOPS attachment demonstrate that low-frequency noise is more sensitive to dynamic molecular processes than traditional CNP-based measurements. These findings reinforce the role of electrical noise as a functional readout for biosensing applications.

References

[1] V.Kammarchedu et al., “Recent advances in graphene-based electroanalytical devices for healthcare applications”,Nanoscale, vol.16, 2024, pp.12857-12882.
[2] M. Fomin et al., “Liquid-Gated Graphene Field-Effect Transistors for Biosensing on Lipid Monolayers”. Phys. Status Solidi B, vol. 260, n.12, 2023, pp. 2300324-1-6.

The effects of examination methods on describing the scale-free nature of human locomotor activity

K. P. Komáromi[1], B. Maczák[1], G. Vadai[1]

[1]Department of Technical Informatics, University of Szeged, Szeged, Hungary
vadaig@inf.u-szeged.hu

Abstract: Although human dynamics exhibit scale-independent properties, conflicting models have emerged from the statistical analyses of different actigraphic or mobility datasets beyond the power law distribution. We show in the case of human locomotor activity, that both the non-standardized activity determination methods and statistical or model fitting approaches could affect the conclusions, while they have no effect on its universal, 1/*f*-based spectral characteristics.

Keywords: actigraphy, scale-free nature, 1/*f* noise, human dynamics

Introduction Human dynamics exhibit scale-free characteristics in both spatial movement data and locomotor activity measurements. However, statistical analyses of different datasets have led to conflicting models beyond the commonly observed power law distribution. Locomotor activity is often quantified in medical research using so-called actigraphs, devices that measure the acceleration of the wrist and compress it to an activity value for every epoch (non-overlapping, consecutive timeslots, typically of 1 minute). However, the methods used to derive activity values vary significantly across manufacturers and are not disclosed properly. Consequently, differently produced activity signals are often analyzed without a sufficient description of the underlying methodology. Additionally, statistical methods for analyzing the device-dependent activity data are not standardized in the literature either. While all related studies separate activity signals into active and passive periods and examine the distribution of their durations, they differ in key aspects, such as the threshold used for separating the periods, the type of distribution function (Probability Density Function - PDF, Complementary Cumulative Distribution Function - CCDF) used for examining the durations, the fitting method (least squares, maximum likelihood) and its range, the selection of fitted distributions, and the approach used for determining the most suitable one [1,2]. In contrast, as we previously showed, the spectra of both acceleration signals measured on the wrist for several days, and the activity signals derived from them follow a universal, 1/*f* noise-based spectral characteristic – representing the spectral scale-free property –, independent of the actigraphic methodology [3].

Results To demonstrate how the conclusions depend on the way of processing actigraphic signals, we compared the distributions of datasets generated in various ways for the same movements. By complementing our previous work [4] with an expanded comparison of additional methods and a more detailed examination of the effects of individual parameters, we showed that both the different activity determination methods and the threshold rule separating activity signals to active and passive periods potentially influence the distribution we determine for the same motion. When we used a threshold greater than the mean of the data, the distribution appeared more likely to follow truncated power law. This result is consistent with the literature: studies that determined the best fitting model other than power law or truncated power law (or exclusively fitted these) used a threshold less than or equal to the mean.

Our aim was to further investigate the impact of different statistical approaches found in the relevant studies on model fitting. We found that factors such as the number of bins used for PDF, data pooling, fitting techniques, and the choice of goodness-of-fit metrics all influence the

results. Fig 1. shows that the choice of *xmin* has a significant effect: most frequently lognormal distribution was identified as the best fit when fitting over the entire range, but as *xmin* increased – meaning the fit focused more on the tail –, the truncated power law became dominant, and when only the tail was fitted, the stretched exponential emerged as the prevailing model.

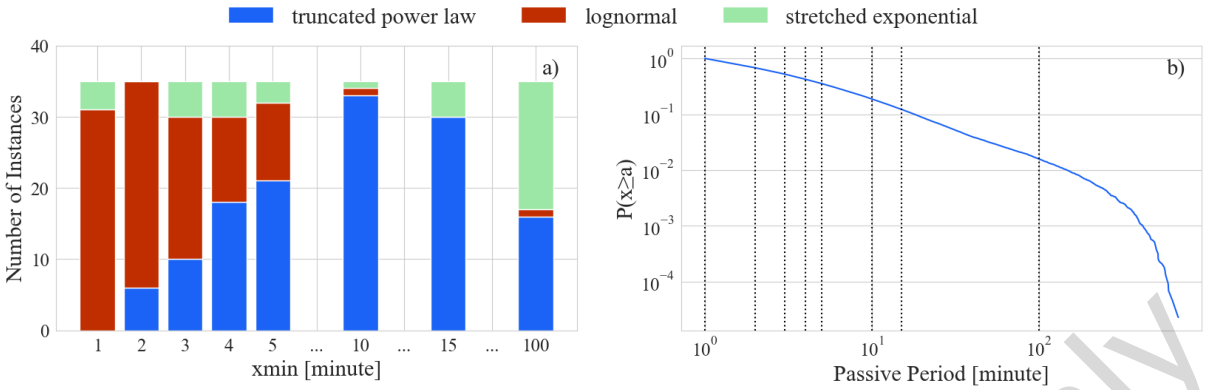

Fig. 1: a) The distribution of the best-fitted models for the pooled passive periods of activity data generated using 35 different activity calculation methods as a function of changing *xmin*. b) An example for the CCDF of passive periods pooled over the 42 subjects for a given type of activity data, and the fitting regions determined by *xmin*.

Finally, using specific combinations of different activity determination methods and threshold rules from various studies, we demonstrated in Fig. 2 a) that the shape of the distribution varies substantially for the same data. The best-fitting models also differed, but in different ways depending on *xmin*. While these differences together greatly affect the results, the spectra of the same activity values depicted in Fig. 2 b) follow universal 1/*f* noise-based characteristics. Since the spatial motion has the same spectral characteristics [5], these results suggests that the scale-free nature of human dynamics can be examined more robustly in the frequency domain.

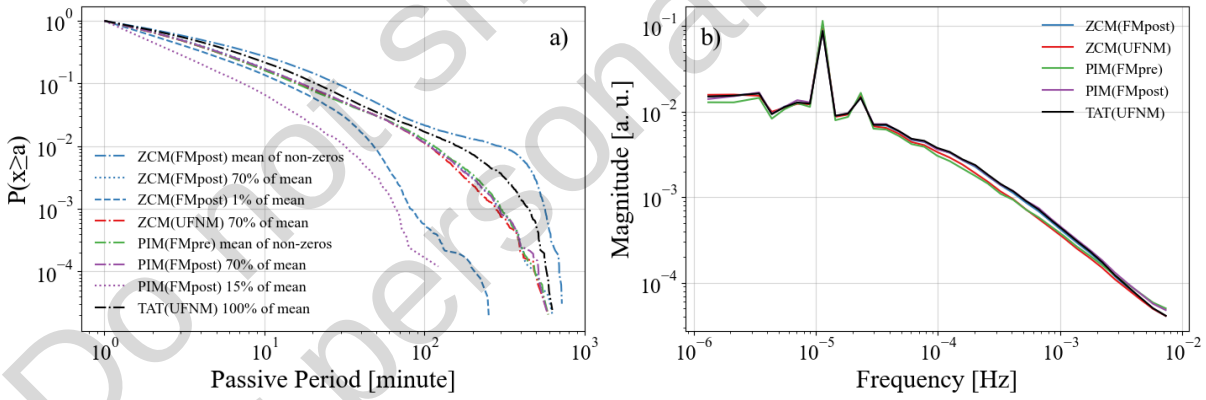

Fig. 2: a) The CCDF of passive periods for the different types of activity determination methods and threshold values found in the literature pooled over the 42 subjects. b) The PSD of the same type of activity signals, each of them ensemble-averaged over the subjects (for details, see [3]).

References

[1] J. J. Chapman et al., „Quantification of free-living activity patterns using accelerometry in adults with mental illness", *Scientific Reports* 7, 43174 (2017)
[2] M. Hirose et al., „Altered distribution of resting periods of daily locomotor activity in patients with delayed sleep phase disorder", *Frontiers Psychiatry* 13, 933690 (2022)
[3] B. Maczák et al., „General spectral characteristics of human activity and its inherent scale-free fluctuations", *Scientific Reports* 14, 2604 (2024)
[4] B. Maczák et al., „Different Aspects of the Scale-Free Nature of Human Activity – Examination of Its Spectral and Statistical Properties", *26th Int. Conf. Noise Fluct.*, Grenoble, France (2023).
[5] B. Maczák et al., „The Noise of Our Daily Motion: General Spectral Characteristics of Human Mobility and Activity", *Fluctuation and Noise Letters* (2024)

Phase structure of conduction in ion channels

W.A.T. Gibby[1], D.G. Luchinsky[1,2], I.A. Khovanov[3], P.V.E. McClintock[1]

[1]Department of Physics, Lancaster University, Lancaster LA1 4YB, UK.

[2]KBR, Inc., Ames Research Center, Moffett Field, CA 94035, USA

[3]School of Engineering, University of Warwick, Coventry CV4 7AL, UK

p.v.e.mcclintock@lancaster.ac.uk

Abstract: We study Coulomb blockade phenomena in biological ion channels and their condensed matter counterparts. Our aim is to reveal new features as well as to further demonstrate the significance of Coulomb blockade for noise-driven ionic transport. We have found a novel phase diagram describing ionic conduction that is closely analogous to its electronic counterpart (Coulomb diamonds). We use it to gain insight into the fundamental nature of the ionic conduction properties.

Keywords: Ionic Coulomb blockade, biological ion channel, nano-channel, ionic current.

Introduction: Biological ion channels are fundamental to living organisms and are extensively targeted in pharmacology for the development of channel-specific drugs. It is well known that the biomimetic approach is leading to the successful design of highly functionalised pores. Despite significant recent advances, the understanding, prediction, and control of charge transport in these channels still presents formidable challenges in both nanotechnology and biophysics. Recent research has identified critical gaps in our understanding of ionic conduction in nano-channels, particularly in the areas of correlated transport and the conditions required to enhance the selection of specific ions.

Among the phenomena believed to underpin the selectivity and conductivity properties of nano-channels, ionic Coulomb blockade (ICB) stands out as one of the most important [1]. It is the ion-related counterpart of electronic Coulomb blockade, which controls transport in quantum devices, and which is widely observed in man-made nanostructures. The phenomenon arises due to the extremely small capacitance of the system on the nanoscale. As a result, both the electrostatic energy and Coulomb charging energy can easily exceed the thermal energy, fundamentally altering the ways in which charge carriers interact with the channel. The total energy $\mathcal{E}$ of an ion in a channel may be written

$$\mathcal{E} = \frac{(nzq + Q_{\rm ex})^2}{2C_{\rm dot}} = U_{\rm c}(n_{\rm ex} \pm nz)^2, \quad \text{where} \quad U_{\rm c} = \frac{q^2}{2C_{\rm dot}} \gg k_{\rm B}T. \tag{1}$$

Here $z = 1$ and $q = -e$ for electronic Coulomb blockade, while $z = 1, 2, \ldots$ and $q = \pm e$ for ICB, where e is the elementary charge, and n is the number of mobile charges; $Q_{\rm ex} = n_{\rm ex}e$ is an externally controlled charge, either on the channel wall in the ionic case, or induced by the gate voltage on the quantum dot in the electronic case. Thus, in these systems the conducting device can accommodate only a small, discrete, number of charged particles.

So studies of ICB in these channels promise to illuminate their structure-function relationships including their remarkable selectivity between particular ions, whether of different valence or alike. The results should be equally applicable to biological and artificial channels.

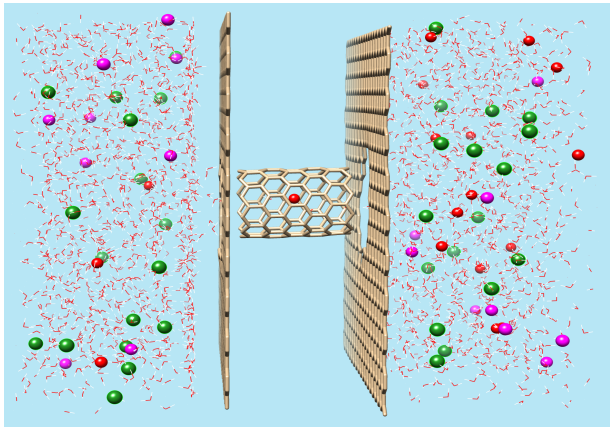

Figure 1: The model: a carbon nantube shielded by graphene sheets, with water and Ions. Potassium ions are shaded red, chloride ions are shaded green, and magenta balls represent sodium ions. Carbon atoms and connecting bonds are shaded light brown. Water bonds are shown by red (oxygen) and white (hydrogen) sticks.

Materials and methods: We use all-atom molecular dynamics simulations to investigate ionic conduction in a short, single-wall, charged, carbon nanotube (CNT) [5]. It mimics the selectivity filter of a biological K^+ ion channel, as shown in Fig. 1. It includes graphene sheets, and a CNT connecting two bulk solutions with water molecules and ions. The simulations were performed with GROMACS software using the NPT ensemble with a 2 fs time step. The potential of the mean force was calculated using the well-tempered metadynamics approach.

Results: We have extended the investigation [5] to include variation of the bias voltage. We find that it produces a complex phase structure, *ionic Coulomb Diamonds*, closely analogous to its electronic counterpart [3]. This structure provides novel insight into transport through these channels, in that gaps (blockade) in conduction are observed as a function of bias and gate voltage. We then further investigate its properties through the use of a rigorously-derived statistical theory [2]; which calculates ionic conduction through the lens of particle number fluctuations and the Green-Kubo relations [4],

$$\chi \propto \frac{\partial \langle zn \rangle}{\partial \Delta\bar{\mu}}. \tag{2}$$

Here, $\Delta\bar{\mu}$ is the difference in excess chemical potential energy between bulk and pore i.e. the non-polar and electrostatic (Born and Debye-Hückel) contributions to the solvation free energy in the pore and bulk. Finally, we discuss the importance of these results within the context of narrow biological ion channels.

This work was supported: by a Leverhulme Trust Research Project Grant [RPG-2017-134]; and by the Engineering and Physical Sciences Research Council (UK) [grant number EP/M015831/1].

References

1. I. K. Kaufman et al., “Coulomb blockade model of permeation and selectivity in biological ion channels,” New J. Phys., vol. 17, no. 8, 2015, pp. 083021.
2. W. A. T. Gibby et. al., “Physics of selective conduction and point mutation in biological ion channels,” Phys. Rev. Lett., vol. 126, 2021, pp. 218102.
3. C. Beenakker, “Theory of Coulomb-blockade oscillations in the conductance of a quantum dot,” Phys. Rev. B, vol. 44, no. 4, 1991, pp. 1646–1656.
4. R. Kubo, “The fluctuation-dissipation theorem,” Reps, Progr. Phys., vol. 29, no. 1, 1966, pp. 255.
5. W. A. T. Gibby et. al., ”Ionic Coulomb blockade controls the current in a short narrow carbon nanotube”, J. Chem. Phys. vol. 161, 2024.

Challenges of assessing fluctuations in actigraphic acceleration data under sleep and wakefulness

B. Maczák[1], Cs. G. Horváth[2], B. Rozner[3], S. Kim[2], R. Bódizs[2], G. Vadai[1]

[1]Department of Technical Informatics, University of Szeged, Szeged, Hungary
[2]Institute of Behavioural Sciences, Semmelweis University, Budapest, Hungary
[3]Institute for Biology, University of Veterinary Medicine, Budapest, Hungary
maczak@inf.u-szeged.hu

Abstract: After we successfully described the $1/f$ noise-based universal spectral characteristics of multi-day human locomotor activity, we now assessed the challenges one may encounter if examining wrist acceleration instead of the classical activity data separately for sleep and wakefulness within days. Our findings highlight that spectral characteristics during sleep are highly sensitive to acceleration measurement errors, preprocessing techniques, and sleep interval definitions, underscoring the need for careful methodological considerations.

Keywords: actigraphy, $1/f$ noise, human dynamics, sleep and wakefulness

Introduction Actigraphy is widely utilized in medical fields (e.g., somnology or psychiatry) to quantify human locomotor activity, however, its methodology lacks standardization: the way the measurement devices (actigraphs) compress the acceleration of the wrist preprocessed in a given way into minute-wise activity values can differ greatly across manufacturers. As we previously demonstrated in a comparative study [1], this variation can compromise the comparability and reproducibility of scientific works. The scale-free nature of human locomotor activity has been examined mostly with Detrended Fluctuation Analysis (DFA) in addition to standard statistical methods, mainly for diagnostic purposes, and separately for sleep and wakeful intervals within a day [2,3]. Moreover, these studies have almost exclusively analyzed activity data from devices of different manufacturers. Previously, we have found that the Power Spectral Density (PSD) of multi-day activity signals follow a universal spectral characteristic – containing $1/f^{\alpha}$ ($\alpha \approx 1$) noise – independent of the actigraphic methodology and discovered that even the raw acceleration of the wrist can be described in the same way [4, 5]. The latter is particularly relevant since actigraphs capable of storing raw triaxial acceleration have recently become available. In this work, we present how this new opportunity of analyzing acceleration data – that is especially beneficial in assessing higher-frequency fluctuations – introduces new challenges and factors in the analysis of within-day fluctuations under sleep and wakeful states that can significantly impact results if not handled properly.

Results We examined triaxial acceleration data from healthy subjects recorded on their non-dominant wrists using GENEActiv devices at 100 Hz sampling rate. Although accelerometers in actigraphs are factory-calibrated, the remaining per-axis errors (scale, offset, orthogonality) result in stepwise offset differences in the magnitude of acceleration. We analyzed the impact of deterministic errors on the spectra by applying our postcalibration algorithm [6], as seen in Fig. 1 a). While the slope of the spectra remained $\alpha \approx 1$ during wakefulness after postcalibrating, the slope changed from $\alpha \approx 1$ to $\alpha \approx 0$ during sleep as seen in subplot b), indicating that the steeper spectrum in the latter case is merely an artifact of measurement error. We also found that this whitening of the spectrum happens only if the examined sleep interval did not contain parts of higher activity, which in fact could be rather considered states of wakefulness. Consequently, the analysis was sensitive to how sleep intervals were identified (based on EEG and GGIR R package), as seen by comparing Fig. 1 b) and c).

Acceleration and activity data of all types remained correlated ($\alpha \approx 1$) during wakefulness. However, while the spectra whitened ($\alpha < 1$) for activity data during sleep, the same was observed for only those acceleration signals, where the effect of Earth's gravity was eliminated from the magnitude data (UFNM, ENMO, FMpre, HFMpre) as seen in Fig. 2, where the effect of postcalibration can also be observed. In contrast, we found $\alpha > 1$ during sleep for per-axis accelerations that contain direction-specific information, irrespective of postcalibration.

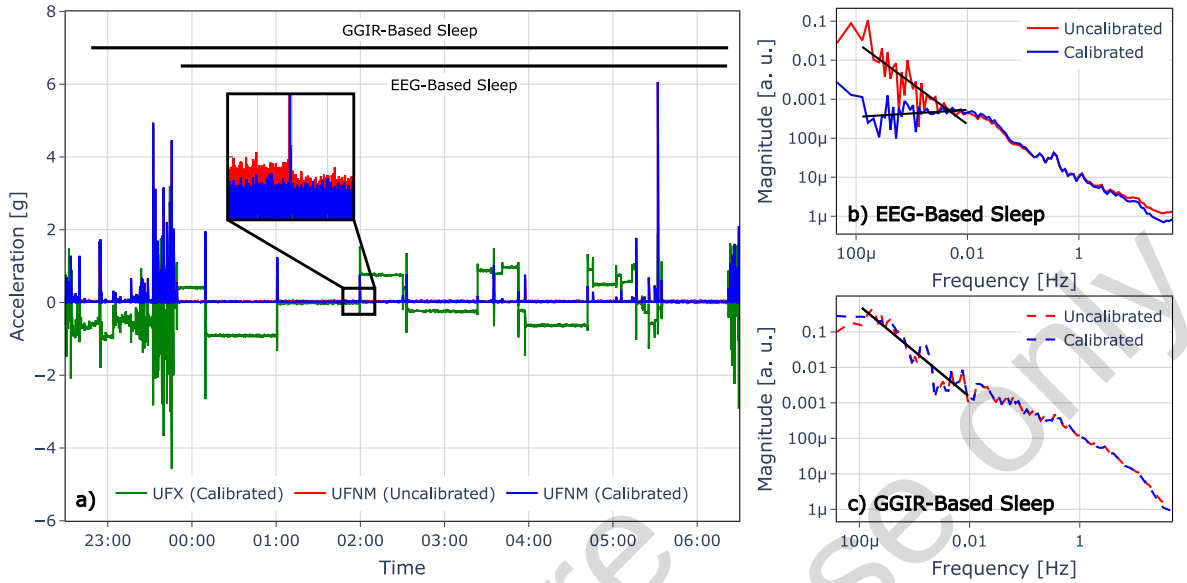

Fig. 1: a) For an exemplary subject, one night of x-axis acceleration, and normalized magnitude of acceleration (see [1] for details) data before and after postcalibration, and the sleep intervals. b-c) The PSD (filtered using the Daniell method [4]) of the normalized acceleration before and after postcalibration for the EEG (b) and van Hees algorithm-based (c) sleep intervals. The trend of the spectra between 10^{-4} and 10^{-2} Hz is depicted as black lines.

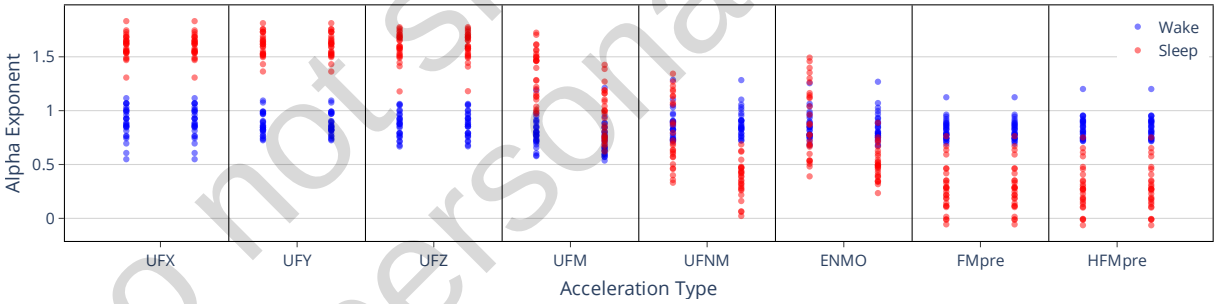

Fig. 2: The α exponents measured during sleep and wakefulness for the different acceleration preprocessing techniques (see [1] for details). Groups separated by vertical lines contain two columns: exponents before (left) and after postcalibration (right). Each column consists of one sleep and wake exponents (red and blue dots) for each of the 27 subjects, averaging over 5 sleep and wakeful intervals.

References

[1] B. Maczák et al., „Detailed analysis and comparison of different activity metrics", *PLOS ONE* 16, e0261718 (2021)
[2] O. Minaeva, et al., „Fractal motor activity during wakefulness and sleep: a window into depression recency and symptom recurrence", *Psychological Medicine* 54, 4429–4437 (2024)
[3] P. M. Holloway. et al. „Complexity analysis of sleep and alterations with insomnia based on non-invasive techniques", *Journal of The Royal Society Interface* 11, 20131112 (2014).
[4] B. Maczák et al., „General spectral characteristics of human activity and its inherent scale-free fluctuations", *Scientific Reports* 14, 2604 (2024)
[5] B. Maczák et al., „Revealing the Generality of 1/*f* Noise Based Spectral Characteristics of Human Activity Across Different Datasets", *26th International Conference on Noise and Fluctuations*, Grenoble, France (2023).
[6] D. Faragó et al., „Enhancing Accuracy in Actigraphic Measurements: A Lightweight Calibration Method for Triaxial Accelerometers", *IEEE Access* 12, 38102-38111 (2024)

Detrended Moving Average Cross-Correlation Analysis of Interaural Interaction in Contralateral Suppression

Sinyoung Lee, Ken Kiyono

Graduate School of Engineering Science, Osaka University, Osaka, Japan

lee.sinyoung.es@osaka-u.ac.jp

Abstract: Some individuals experience difficulty understanding speech in noisy environments despite having normal hearing. This may be related to hidden hearing loss or auditory processing disorder. Ability of attention on a particular sound in a noisy environment is potentially related to the cochlear efferent system. Contralateral masking, mediated by the medial olivocochlear reflex, affects auditory perception by modulating sound detection in the ipsilateral ear. This study investigates interaural interaction during contralateral suppression of distortion-product otoacoustic emissions (DPOAEs) using detrended moving average cross-correlation analysis (DMCA). Sound in both ears was recorded in normal-hearing subjects while applying pink noise as a contralateral masker. Results indicate that the masking sound is transmitted to the opposite ear only in the low-frequency range (10–100 Hz) during contralateral suppression. These findings provide insight into auditory processing mechanisms and their physiological implications.

Keywords: Distortion-Product Otoacoustic Emissions, Contralateral Masking, Cochlear efferent system

Some people may have difficulty understanding speech, especially in noisy environments, despite having normal hearing levels in standard hearing tests. These difficulties may be due to hidden hearing loss or auditory processing disorder. The cocktail party effect, which refers to the ability to focus attention on a particular stimulus in a noisy environment, is thought to be mediated by the cochlear efferent system. Furthermore, contralateral masking is a phenomenon that occurs due to the medial olivocochlear reflex, in which a masker (i.e., noise) presented to the contralateral ear affects the ability to detect a sound in the ipsilateral ear [1]. To evaluate the cochlear efferent system and the medial olivocochlear reflex non-invasively, contralateral suppression of otoacoustic emissions (CSOAE), which are sounds generated by the active cochlea and emitted toward the ear canal, has been studied [2]. Several studies have examined the correlation between the magnitude of CSOAE and the results of speech discrimination tests in noisy environments. However, interaural interaction during CSOAE measurement has not been sufficiently evaluated [3]. Since sound stimuli, which can be louder than environmental noise, are applied to both ears during CSOAE measurement, the stimuli could be transmitted to the opposite ear through bone conduction [4]. Furthermore, contralateral suppression might alter background noise in the ear canal, thereby improving listening in noisy environments. In this study, interaural interaction during the measurement of contralateral suppression of distortion-product otoacoustic emissions (DPOAEs), a type of otoacoustic emission used for objective hearing tests, was evaluated using detrended moving average cross-correlation analysis (DMCA) [5] of the sound recorded in both ear canals.

In our measurements, sound in both ear canals was recorded in subjects with normal hearing and no history of ear disease. DPOAEs were measured using a probe composed of two separate transducers and one microphone (ER-10C, Etymotic Research). A compound sound, consisting

of two pure tones represented by sinusoidal waves, was generated by each transducer, and the sound in the ipsilateral ear canal was recorded by the microphone. The measurement system was validated to ensure that distortion-product components were not produced by the system itself. Pink noise (1/f noise) was applied as a contralateral masking noise using another probe inserted into the contralateral ear canal. The amplitude of the contralateral stimulus was adjusted so that the noise level in LAeq (Equivalent Continuous A-weighted Sound Pressure Level) was approximately 30 dB higher than the background noise level in the ear canal before contralateral stimulation. Subjects sat in a soundproof room and remained relaxed during the measurements. For comparison, DPOAEs were also measured in the same ear without contralateral stimulation. Sound in both ears was recorded simultaneously during the measurement. Each measurement lasted 2 seconds, and the sampling frequency of the recording was 100 kHz.

Cross-correlation between the sound recorded in both ears was analyzed using DMCA, which is a method for characterizing the cross-correlation between two non-stationary time series. The process involves calculating moving averages over a sliding window, removing local trends, and then computing the cross-correlation function. DMCA is widely used in fields such as biosignal analysis to detect hidden relationships in complex systems. Compared to standard correlation measures, DMCA provides a more accurate assessment of dependencies in time series with non-stationary behavior.

As shown in Fig. 1, our analysis results show that the contralateral masking sound using 1/f noise is transmitted to the ipsilateral ear only in the low-frequency range (10 Hz to 100 Hz) when DPOAE level was suppressed by contralateral masking noise. The magnitude of contralateral suppression and information contained in the sound from both sides of ears might be changed by varying the ipsilateral and the contrealateral stimulus. It will evaluated and its physiological interpretation will be discussed.

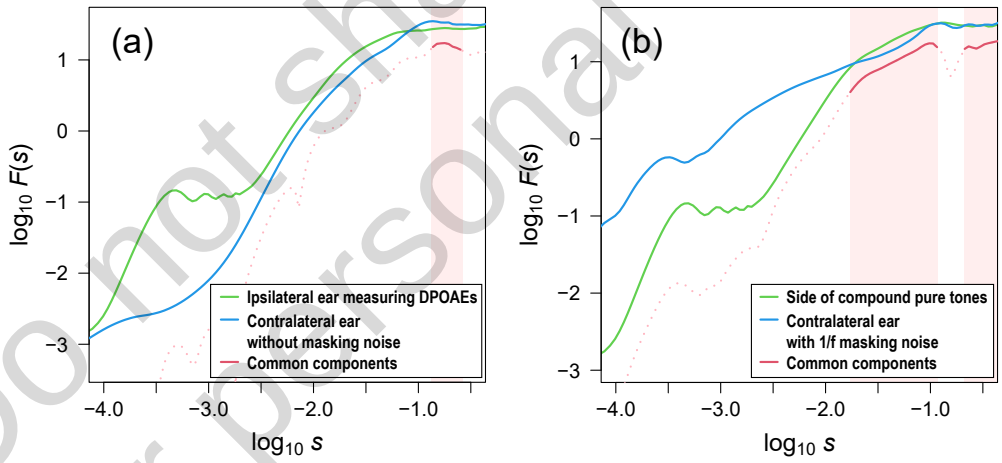

Figure 1: DMCA results: (a) without contralateral masking noise and (b) with 1/f contralateral masking noise. Common components were observed in the area shaded in pink.

References

1. J.M. Aronoff *et al.*, "Contralateral masking in bilateral cochlear implant patients: a model of medial olivocochlear function loss."*PloS one*, vol. 10 (2015), e0121591.
2. R.R. Ciuman, "The efferent system or olivocochlear function bundle - fine regulator and protector of hearing perception."*International journal of biomedical science : IJBS*, vol. 6 (2010), pp. 276-288.
3. Y. Shi *et al.*, "Effects of interaural intensity and time disparity on transient evoked otoacoustic emissions", Hearing Research, vol. 110 (1997), pp. 259-265.
4. S. Stenfelt, "Model predictions for bone conduction perception in the human", Hearing Research, vol. 340 (2016), pp. 135-143.
5. A. Nakata *et al.*, "Generalized theory for detrending moving-average cross-correlation analysis: a practical guide." Chaos, Solitons & Fractals: X, vol. 3 (2019): 100022.

Decorrelation of the Mean-Variance Correlation in Heart Rate Variability via the q-Logarithmic Transform

Ken Kiyono, Keisuke Hiroya, Sinyoung Lee

Graduate School of Engineering Science, Osaka University, Osaka, Japan

kiyono.ken.es@osaka-u.ac.jp

Abstract: In biological signal time series, the local mean and local variance often exhibit correlation (mean-variance correlation). However, conventional time series analysis, which is based on weakly stationary linear stochastic processes, does not fully account for this phenomenon. For instance, heart rate variability (HRV) is widely used to assess autonomic nervous function, yet typical HRV indices assume the absence of mean-variance correlation. In this study, we propose a novel approach for evaluating and characterizing mean-variance correlation using the *q-logarithmic transformation*. Originally introduced in non-additive statistical mechanics, this transformation bridges additive ($q = 0$) and multiplicative ($q = 1$) processes. By adjusting the parameter q, mean-variance correlation can be decoupled. The effectiveness of this method was validated using synthetic *1/f fluctuation* data and real HRV data. When applied to actual HRV data, the estimated q values were non-integer, demonstrating the practical utility of this method in analyzing non-stationary biological signals.

Keywords: $1/f$ fluctuation, Long-range cross-correlation, volatility clustering, Box-Cox transformation

In time series data of biological signals, the phenomenon of correlation between the local mean and local variance, known as the mean-variance correlation, is frequently observed. However, this phenomenon is not fully accounted for in the conventional framework of time series analysis, which is based on the assumption of weakly stationary linear stochastic processes. For instance, heart rate variability (HRV) contains crucial information related to autonomic nervous system function and disease prognosis [1]. However, commonly used HRV indices are defined under the assumption that mean-variance correlation is absent. In other words, the baseline variability of the time series and the fluctuations in local variance have been considered independent stochastic processes.

In this study, we propose the application of the q-logarithmic transformation for characterizing mean-variance correlation. The q-logarithmic transformation, defined as

$$\ln_q x := \frac{x^{1-q} - 1}{1 - q}, \tag{1}$$

where q is a real-valued parameter, was originally introduced in the field of non-additive statistical mechanics by Tsallis [2]. This transformation serves as an operation bridging the gap between additive ($q = 0$) and multiplicative ($q = 1$) processes. The q-logarithmic transformation can be applied to an operation called the q-product, defined as

$$x \otimes_q y := \left[x^{1-q} + y^{1-q} - 1\right]^{\frac{1}{1-q}}, \tag{2}$$

where variables connected by the q-product can be decomposed into sums through the q-logarithmic transformation [3]. This is analogous to the conventional logarithm ($q = 1$), where the logarithm of a product is equal to the sum of logarithms.

Notably, the q-logarithmic transformation shares the same mathematical form as the transformation used in the Box-Cox method [4]. Although the Box-Cox transformation is primarily employed to normalize asymmetrically skewed distributions, we demonstrate that adjusting the parameter q in the q-log transformation, when applied to a time series, effectively decouples mean-variance correlation. The optimal value of q is determined by identifying the point at which the cross-correlation between the observed time series and its absolute difference becomes uncorrelated.

HRV is widely known to exhibit long-term correlation characteristics, such as *1/f fluctuations* [5]. In this study, we further clarify that applying the q-logarithmic transformation to time series data with such long-term correlations effectively removes mean-variance correlation.

To validate the effectiveness of the proposed method, we generated synthetic time series $\{x_n\}$ exhibiting mean-variance correlation by applying a q-exponential function, defined as

$$\exp_q x := [1 + (1 - q)x]^{\frac{1}{1-q}}, \tag{3}$$

to numerically simulated 1/f fluctuations, as shown in Fig. 1. The long-term cross-correlation characteristics between $\{x_n\}$ and its absolute difference $|x_n - x_{n-1}|$ were then evaluated using *detrended moving-average cross-correlation analysis* (DMCA), a technique suitable for analyzing non-stationary time series [6]. Specifically, since both $\{x_n\}$ and $|x_n - x_{n-1}|$ exhibit long-term correlation in the case of $1/f$ fluctuations, DMCA was used to analyze these characteristics in detail.

Our numerical experiments confirmed that the proposed method can accurately estimate the true pre-set value of q. Furthermore, when applied to real HRV time series, the estimated q values were found to be non-integer, demonstrating the practical applicability of the method.

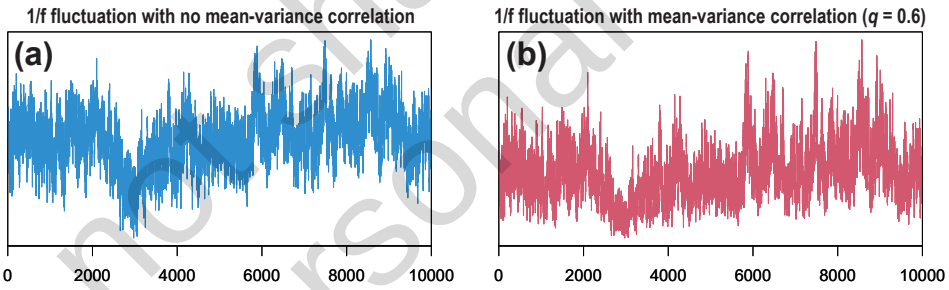

Figure 1: (a) Sample time series of 1/f fluctuations. (b) Time series obtained by applying a q-exponential transformation with $q = 0.6$ to (a). While (a) exhibits no mean-variance correlation, (b) does.

References

1. R. Sassi *et al.*, "Advances in heart rate variability signal analysis: joint position statement by the e-Cardiology ESC Working Group and the European Heart Rhythm Association co-endorsed by the Asia Pacific Heart Rhythm Society." Ep Europace 17.9 (2015): 1341-1353.
2. C. Tsallis, "Possible generalization of Boltzmann-Gibbs statistics." Journal of statistical physics 52 (1988): 479-487.
3. T. Yamano, "Some properties of q-logarithm and q-exponential functions in Tsallis statistics." Physica A: Statistical Mechanics and its Applications 305.3-4 (2002): 486-496.
4. G.E.P Box and D.R. Cox. "An analysis of transformations." Journal of the Royal Statistical Society Series B: Statistical Methodology 26.2 (1964): 211-243.
5. M. Kobayashi and T. Musha, "1/f fluctuation of heartbeat period." IEEE transactions on Biomedical Engineering 6 (1982): 456-457.
6. A. Nakata *et al.*, "Generalized theory for detrending moving-average cross-correlation analysis: a practical guide." Chaos, Solitons & Fractals: X 3 (2019): 100022.

Preservability and fluctuation of the biding activity of sugar chains to influenza viruses

M. Hinatsu[1], M. Mineta[2], H. Hiramatsu[2], V. R. Kudkyal[1], K. Hayashi[2], T. Kawahara[1,2*]
S. Nakakita[3], Y. Watanabe[4], T. Ono[5], Y. Kanai[6], K. Matsumoto[7]

[1]Graduate School of Engineering, Chubu University, Kasugai, Japan
[2]College of Life and Health Sciences, Chubu University, Kasugai, Japan
[3]Life Science Research Center, Kagawa University, Kagawa, Japan
[4]Graduate School of Medical Sciences, Kyoto Prefectural University of Medicine, Kyoto, Japan
[5]Graduate School of Engineering Science, Osaka University, Osaka, Japan
[6]International Center for Synchrotron Radiation Innovation Smart, Tohoku University, Sendai, Japan
[7]SANKEN, Osaka University, Osaka, Japan
*E-mail: toshi@fsc.chubu.ac.jp

Abstract: A worldwide outbreak of influenza is the most feared potential public health emergency of international concern. The spread of influenza A virus variants requires continuous monitoring given the high mutation rate of the virus. For the actual application of bio sensors, they will be preserved for a few years. In this paper, we will discuss about the preservability for the sugar chain probes using pyrenylated sialylglycopeptide (P-SGP) and neoglycoprotein. The relative errors in the binding activity will also be addressed, depending on the preparation process for the sugar chain probes.

Keywords: influenza virus, host specificity, sugar chain, bio sensor, preservability

Introduction Influenza is a zoonotic disease [1] and its worldwide outbreak is the important target in the area of public health. Influenza viruses have the capability of pandemic with high mutation rate. Therefore, in order to realize early infection control, an ultra-sensitive sensor that detects early mutations, including infectivity, is required. Therefore, we have developed electrical detection systems using graphene field-effect transistors [2]. Whether the influenza virus infects humans or birds depends on the difference in the binding position of sialic acid (Sia) in the sugar chains on the host cell surface, which is the binding partner of the viral protein hemagglutinin (human receptor: Siaα2-6Galactose, bird receptor: Siaα2-3Galactose). Thus the sugar chains can be used as one of the detection molecueles for the host change mutations in the sensor systems [3].

Now, in response to the recent spread of the new coronavirus (SARS-CoV-2), a simultaneous corona and influenza test kit has been developed, and due to the convenience of the facilities used, the storage period is just under two years. As the actual application of bio sensors for the continuous monitoring, they will be preserved for a few years. Therefore, in this paper, we prepared a sugar chains probes on the ELISA plate to examine the preservability of the probes in the sensor systems. Since molecular size is important in electrical detection, we used pyrenylated Sialylglycopeptide (P-SGP), which has pyrene attached to the end of SGP, comparing with the BSA-SGP, where bovine serum albumin (BSA) used as the scaffold. The relative errors in binding activity fluctuations will also be addressed here. Comparing with BSA-SGP, P-SGP can display smaller relative errors as long time stability.

Materials and methods For the ELISA, P-SGP and BSA-SGP were used as sugar chains. They were applied as the detection molecules on the plate at concentrations of 1 μg/mL to 15.6 ng/mL, and then dried dried with the cleaning process and refrigerated for several months. Human and avian viruses, A/Kobe/536/2011 (H1N1) at 8.9×10^5 PFU/mL and A/swan/shimane/1120Y18/2015 (H5N3) at 1.6×10^5 PFU/mL, respectively, were dropped onto the plate. The binding activity was measured by the absorbance at 490 nm using an iMark Microplate Absorbance

Reader (Bio-Rad) with the virus antibody and color-developing molecule.

Results Figure 1 (a) shows the biding activity between P-SGP and viruses after 12 months of storage. In the figure, the red line indicates the binding activity to human viruses, and the blue line indicates the binding activity to avian ones. Thus we can recognize the host selectivty of each viruses and are suceeded in the preservation. On the other hand, Fig. 1 (b) shows the degradiation for the bindign activity of the BSA-SGP with the preservation for 4 months. There are small difference in the binding activity with sugar chains concentration of 1 μg/mL and slight large deviation. It, however, seems to be slight difficult to recognize the host selectivity of viruses at the low concentrations.

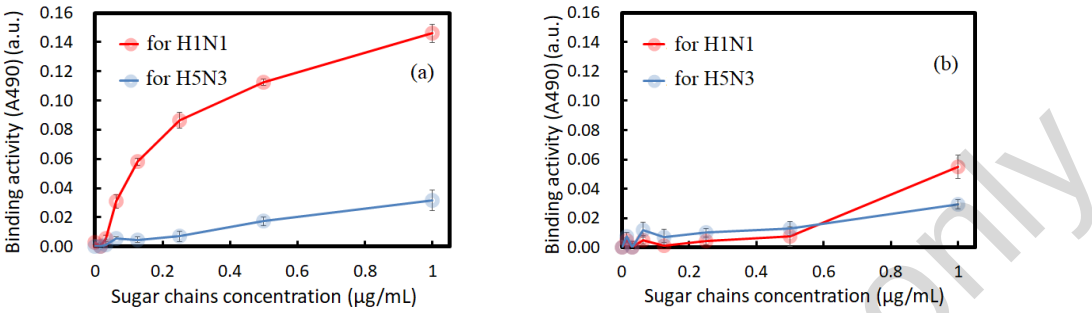

Fig. 1: Sugar chains concentration dependence of binding activity of sugar chains to the viruses with the preservation for 12 months for P-SGP (a), and 4 months for BSA-SGP (b).

Now, we try to discuss about this degradation using the fluctuation in the binding activity and the AFM observations of the sugar chains during the preservation. Fig. 2 shows the relative errors of the binding activity for BSA-SGP for 4 month later. The wider range relative errors can be observed for BSA-SGP comparing with that for P-SGP. Next, we will show the AFM observation for the sugar chains on the plate during the preservation. Fig. 3 shows representative sugar chains of P-SGP with the concentration of 1 ng/mL, and their height distribution. The sugar chains have approximately the height of 3 nm and the many sugar chains seem to have the standing conformation. On the other hand, the height of the BSA-SGP is around 3 nm, which is the same height to the schafold of BSA. Therefore, the sugar chains does not have the standing conformation. For the preservation in the dry condition, the sugar chains could be adhesive to the BSA molecules. It might be the reason for the degradation. Partially broken sugar chains show the large relative errors as the fluctuation and cause the degradation of the binding activity.

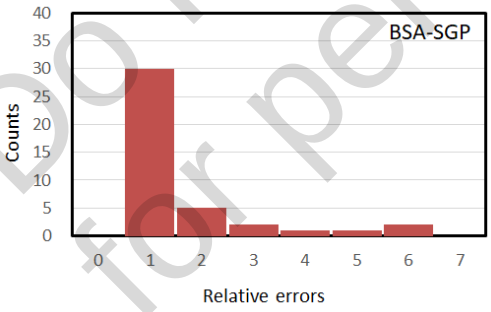

Fig. 2: Relative errors of the binding activity with the 4 month preservation for BSA-SGP.

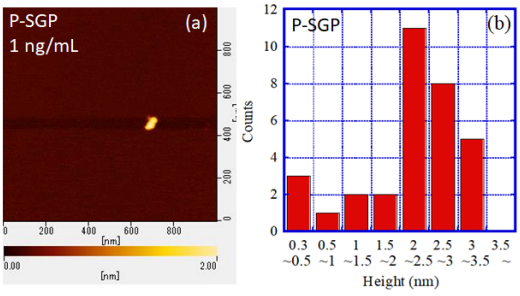

Fig. 3: Representative AFM image for P-BSA during the preservation (a), and the height distribution of sugar chain probes (b).

References

[1] T. P. Peacock et al., "The global H5N1 influenza panzootic in mammals", Nature, vol. 637, 2025, pp. 304-313.

[2] T, Ono et al., "Challenges for Field-Effect-Transistor-Based Graphene Biosensors", Materials, vol. 17, n. 2, 2024, 333.

[3] T. Kawahara et al., "Effective binding of sugar chains to influenza virus on the surface by bovine serum albumin localization", Jpn. J. Appl. Phys., vol. 58, 2019, SIID03.

The Correlation Coefficient Analysis based on Electrocardiographic and Photonic measurements

Matti Huotari[1,]

[1]Faculty of Information Technology and Electrical Engineering, University of Oulu, Oulu, Finland
email matti.huotari7@gmail.com

Abstract: Electrocardiography (ECG), Photoplethysmography (PGG), and here also Mobile Elite heart rate variability HRV with CorSense device measurements were taken into consideration for opportunity to realize a practical, cheap, and easy health condition detection for cardiovascular diagnosis. PPG could be applied for measuring the physiological state of individuals along their ages to connect healthcare applications also with other biosensors. Determination of heart rate variability (HRV), pulse rate variability (PRV) or heart rate fluctuation (HRF) requires accurate and precise measurement of inter beat intervals (IBI) in the ECG, PPG, or in Mobile Elite captured signal. In the measurements, the signals were mathematically collinear and synchronous which happen when PPG, ECG, and Elite HRV based data is simultaneously sampled and recorded. For both ECG. PPG, and Mobile Elite HRV based IBI can be analyzed by the linear correlation analysis. This technique is for any series of pulsed time signals from any source. Here the results visualization is based on the precise and accurate data on the variance inflation factor (VIF). The analysis provides that extra or lagging heart beats were cancelled. Then the data is highly correlated with each other based on the correlation coefficient (R_2). VIF is very informative factor on the linearity. The statistics of slope and correlation coefficients were as a measure for IBIs captured the signals. Because we two or even three dependent variables of IBIs this can provide an elimination of the independent variable (time) for estimating the signal content in the biomedical signal recordings..

Keywords: ECG, PPG, VIF

Introduction ECG is the golden standard signal in the healthy heart measurements, it is used as a reference for the heart rate, heart rate variability, and overall diagnosis. However, precise and accurate PPG sensors responses typically use ECG signals as a reference for dynamic inter pulse interval (IBI) comparison in relation to continuous uses PPG as well ECG could be applied for measuring the physiological state of individuals along their ages. Determination of heart rate variability (HRV), pulse rate variability (PRV) or heart rate fluctuation (HRF) are easily captured nowadays to determine inter beat intervals (IBI) in the ECG, PPG, or in Mobile Elite captured signal.

Materials and methods This study is aimed to propose an accurate system by examining nonlinear dynamics of PPG, ECG, and CorSense Mobile Elite application for HRV determination based on inter beats intervals (IBI). ECG is an electrophysiological signal measured over body whereas PPG is photonic intensity change caused by blood content and volume pulses in small blood vessels and capillaries of the upper skin based on tissue absorption, its scattering, and also photonic transmission properties as a function of wavelength. The ECG electrodes were place the subject's chest and the PPG sensor was placed on the tip of the right and left hand forefingers. CorSense is located on the tip of the left hand forefinger for detect automatically the heart pulse after connecting to Mobile Elite HRV app. This is designed in the measurements. CorSense uses sensitive motion detection for powered automatically on the device and detect a heart pulse without buttons. The high resolution ECG and PPG data were collected with means of the corresponding amplifiers with the sampling rate of 1 kHz.

The lower sampling frequency would be reflected as an error on the correlation plots. The ECG electrodes were the monitoring disposable INTCO sensors. These sensors measure one channel high resolution ECG with three lead electrodes with the amplitude resolution of 16 bit ADC. The PPG sensor is the reflective one.

Results As a reference the Figures shows two analysis results (Fig. 1 & Fig.2).

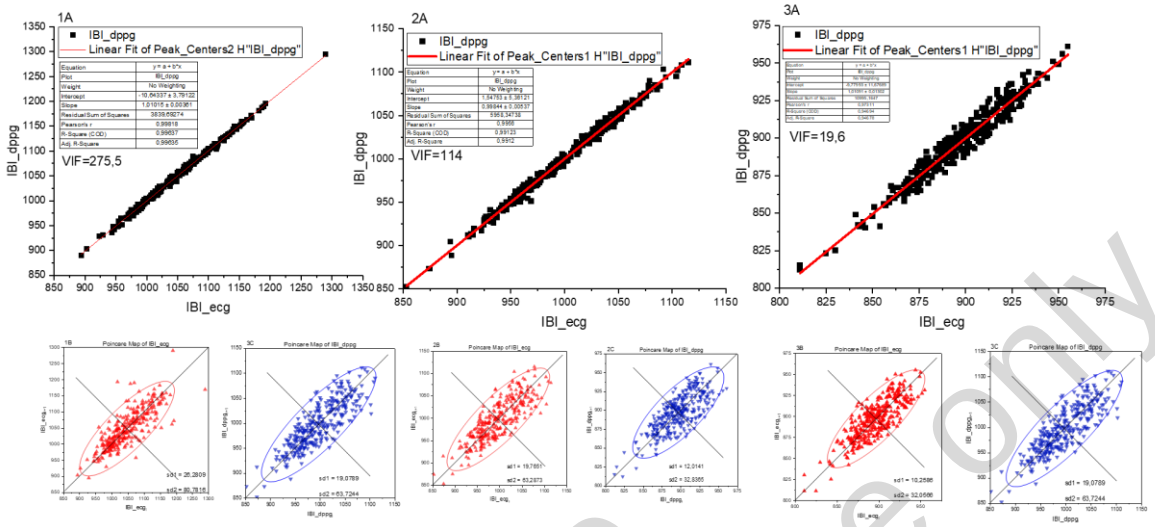

Fig. 1 A male, in supine (1A), sitting (2A), and standing (3A), and corresponding ECG (red), and PPG (blue) Poincaré plots with the parameters sd1 and sd2, the age 66 years.

Figures 1 and 2 show the results of two males with age 66 and 76, respectively.

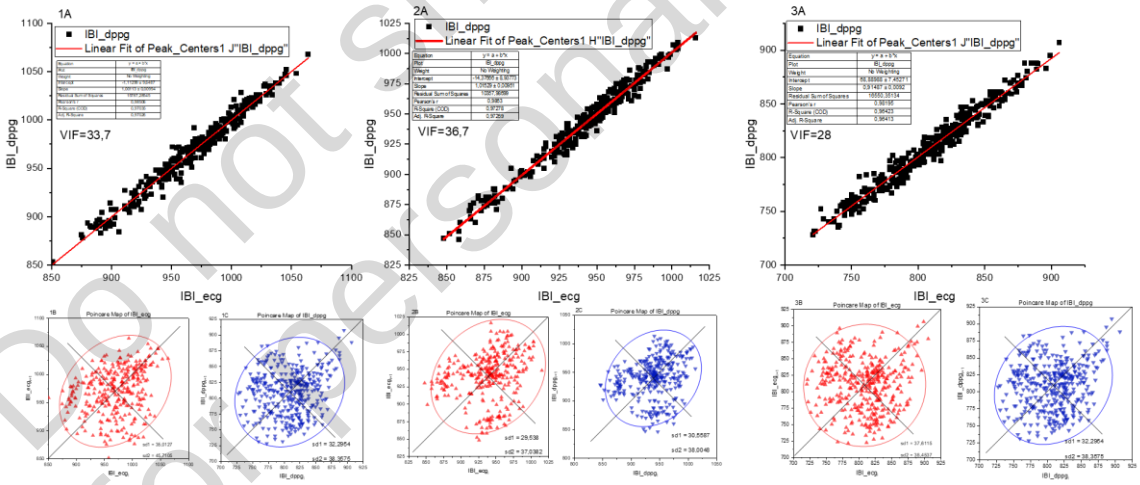

Fig. 2 A male, in supine (1A), sitting (2A), and standing (3A), and corresponding ECG (red), and PPG (blue) Poincaré plots with the parameters sd1 and sd2, the age 76 years.

References

[1] M.P. Tarvainen, P.O. Ranta-aho, P.A. Karjalainen, An advance detrending method with application to HRV analysis, IEEE Transactions on Biomedical Engineering 49 (2) (2002) 172–175.
[2] A.C. Hoog, Y. Mai Y, M. Peltokangas, S. Leonhardt, N. Oksala, A. Vehkaoja. Accuracy of heart rate variability estimated with reflective wrist-PPG in elderly vascular patients. Sci Rep. Apr 14; 11(1):8123. (2021).

Noise-Coupled Memristor Cellular Neural Networks

D. Prousalis[1], V. Ntinas[1], C. Theodorou[2], I. Messaris[1], A. S. Demirkol[1], R. Tetzlaff[1]

[1] Dresden University of Technology (TUD), Dresden, Germany

[2]Univ. Grenoble Alpes, Univ. Savoie Mont Blanc, CNRS, Grenoble INP, CROMA, Grenoble, France

dimitrios.prousalis@tu-dresden.de

Abstract: This study examines the dynamics of Memristor Cellular Neural Networks (M-CellNNs) with noisy interconnection weights. We investigate the impact of noise from synaptic memristors in two coupled cells and demonstrate their effectiveness in modeling the predator-prey system, a fundamental application of coupled M-CellNN cells.

Introduction: Bio-inspired networks mimic biological structures to develop adaptive and efficient technologies. Synapses, key components of such networks, enable signal transmission, learning, and memory through synaptic plasticity. Memristors replicate synaptic functions, attractive for bio-inspired network development [1]. IoT systems generate massive data that overwhelm traditional computing architectures due to the von Neumann bottleneck. CellNNs, performing parallel processing via local cell interactions, offer a solution for tasks like image processing [2]. M-CellNNs enhance efficiency by using memristors in cells and synapses, reducing memory needs and enhancing functionality [3]. Noise in memristors, caused by inherent non-idealities, may result in unpredictable weight update. This work builds on the framework from [4], examining the impact of noise and variability in coupled M-CellNN cells through a minimal case study of two coupled cells.

Noisy M-CellNN: M-CellNN usually consist of two-dimensional spatially distributed arrays of locally coupled cells, see Fig. 1a. During M-CellNN operations, non-volatile memristors act as tunable resistors, preprogrammed to the desired conductance and maintaining their state throughout operation while being subject to noise. The dynamics of certain M-CellNN can be analyzed through a set of coupled Stochastic Differential Equations (SDEs), $\tau_c \dot{\mathbf{x}} = -\mathbf{x}+\mathbf{A}\mathbf{y}+\mathbf{B}\mathbf{u}+\mathbf{z}$, where $\mathbf{x}$ represents the cell states, m and n denote the number of rows and columns, respectively, $\mathbf{y}$ the cell outputs, $\mathbf{u}$ the input, $\mathbf{z}$ the threshold, and τ_c corresponds to the integration time of the cell state. The matrices $\mathbf{A}, \mathbf{B}$ are sparse, representing the synaptic feed-forward and feedback coupling parameters, and consist of both deterministic and stochastic components. The circuit implementation of each network cell is depicted in Fig. 1b, where, v_{xij} represents the capacitor voltage. The feedback synaptic current i_a^{ij} is the sum of all currents from the neighbors and the self-feedback current. The elements of $\mathbf{A}$ and $\mathbf{B}$ represent the conductance of the memristive synapses. The output voltage is given by: $y_{ij} = \frac{1}{2}\left(|v_{ij}+v_s| - |v_{ij}-v_s|\right)$, where v_s represents

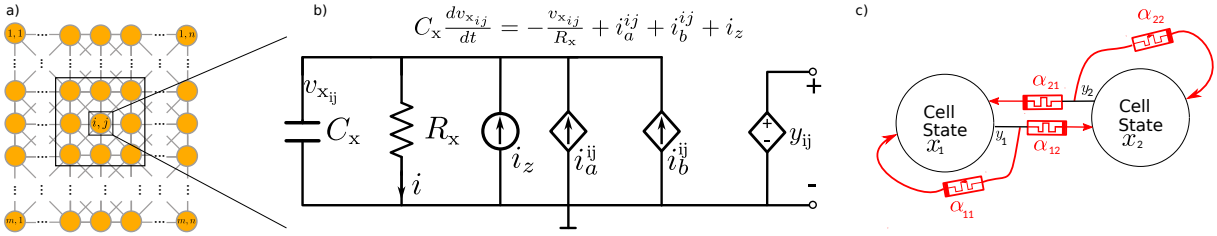

Figure 1: a) M-CNN as an $m \times n$ grid, b) circuit schematic of a cell, and c) two coupled M-CNN cells from Eq. 1.

the saturation voltage. The current i_b^{ij} corresponds to the feedforward current and depends on the input voltages of the neighboring cells. The current component, i_z is the threshold.

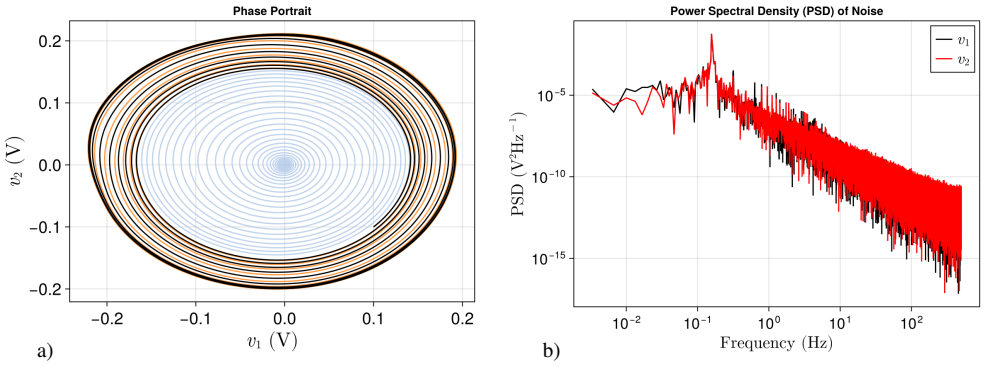

Figure 2: a) Phase portraits of the non-noisy system, i.e. $D = 0$, for three different simulations and for varying values of $\tilde{i}_a^{ij}$. The case with $\sigma_a = 0$ is shown in black, while in blue, the states converge to a stable equilibrium, and in orange, the variability leads to oscillations. For both blue and orange cases, $\sigma_a = 0.1$. The initial conditions are $v_1 = 0.1V$ and $v_2 = -0.1V$. b) Simulation results of the system for $D = 0.01$, where $N = 300$. PSD of the noise on the variables v_1 and v_2.

Two coupled M-CellNNs: Here, we use a physics-based model of Valence Change Memory devices [5] as synaptic elements to analyze M-CellNNs performance under realistic hardware conditions. By studying the minimal case of two coupled M-CellNNs, we demonstrate how variations in physical parameters and noise affect memristor operation, offering insights to enhance M-CellNN robustness and efficiency, see Fig. 1c. We model device-to-device variability by defining the weight components, $\tilde{i}_a^{ij}$ as Gaussian distributions with variances σ_a. The dynamics of two coupled M-CNNs are descibed by the following SDEs

$$\begin{aligned}\tau_c \dot{v}_1 &= -v_1 + R_x \tilde{i}_a^{11}(y(v_1), N_{\mathrm{d},1}) - R_x \tilde{i}_a^{12}(y(v_2), N_{\mathrm{d},2}) + R_x \hat{i}_a^{11} + R_x \hat{i}_a^{12} \\ \tau_c \dot{v}_2 &= -v_2 + R_x \tilde{i}_a^{22}(y(v_2), N_{\mathrm{d},2}) + R_x \tilde{i}_a^{21}(y(v_1), N_{\mathrm{d},1}) + R_x \hat{i}_a^{22} + R_x \hat{i}_a^{21},\end{aligned} \tag{1}$$

where $\tau_c = R_x C_x = 1, R_x = 16, 24k\Omega$, $N_{\mathrm{d},1} = N_{\mathrm{d},2} = 38.4x10^{23}\mathrm{m}^{-3}$, denotes the memristor inner states. The noise in the synapses is a Gausian White Noise (GWN), hence $\tilde{i}_a^{ij} = \sqrt{2D}\xi(t)$ and D denotes the noise strength and $\langle \xi(t) \rangle = 0$. We incorporate experimental insights on memristor noise behavior, including noise strength's variability etc. In Fig. 2a, we present simulations of the non-noisy system, $D = 0$. The stability of the equilibrium point varies depending on the combinations of the $\tilde{i}_a^{ij}$ elements. For $D = 0.01$, Fig. 2b shows the Power Spectrum Density of the noise on v_1 and v_2 across 300 simulations, highlighting non-GWN behavior.

Conclusions: This work explores the dynamics of M-CellNNs under noisy memristive weights, focusing on a minimal case of two coupled cells. By integrating memristive synapses, we analyze how noise and variability influence network behavior. These insights contribute to the development of robust, noise-tolerant M-CellNN architectures.

References

1. A. Mehonic et al., "Memristors—from in-memory computing, deep learning acceleration, and spiking neural networks to the future of neuromorphic and bio-inspired computing," Advanced Intelligent Systems, vol. 2, no. 11, p. 2000085, 2020.
2. L. Chua and L. Yang, "Cellular neural networks: theory," IEEE TCAS, vol. 35(10), pp. 1257–1272, 1988.
3. R. Tetzlaff et al., "Theoretical foundations of memristor cellular nonlinear networks: Memcomputing with bistable-like memristors," IEEE TCAS I: Regular Papers, vol. 67(2), pp. 502–515, 2020.
4. D. Prousalis et al., "Stochastic template in cellular nonlinear networks modeling memristor induced synaptic noise". In Proc. of the 18th ACM NANOARCH Article 23, pp. 1–3, 2024.
5. V. Ntinas et al., "A Simplified Variability-Aware VCM Memristor Model for Efficient Circuit Simulation," 2023 19th SMACD, Funchal, Portugal, 2023, pp. 1-4,

Design and optimization of stochastically driven multi degrees of freedom energy harvesters using equivalent circuits and swarm intelligence algorithms

K. Song[1], M. Bonnin[1], F. Traversa[2], F. Bonani[1]

[1]Deptartment of Electronics and Telecommunications, Politecnico di Torino, Turin, Italy

[2]Memcomputing Inc, CA, US

michele.bonnin@polito.it

Abstract: Energy harvesters are stochastically driven electromechanical systems designed to capture ambient energy and convert it into usable electrical power. However, their performance often suffers from inefficient energy transfer due to impedance mismatches between the mechanical and electrical domains. Inspired by similar problems in RF engineering, we reformulate the design of energy harvesters as a broadband filtering problem, considering the mass-spring systems as mechanical filters. Through the derivation of an equivalent circuit model and frequency domain analysis, we develop a semi-analytical formula to predict the harvested power. To optimize performance, we apply a swarm intelligence algorithm – specifically, flock of starlings optimization – resulting in significantly improved efficiency over traditional, single-degree-of-freedom, harvesters.
Keywords: Energy harvesting, random vibrations, equivalent circuits, swarm intelligence algorithms, flock of starlings optimization

Introduction: Energy harvesting refers to a set of technical solutions to design systems capable of self-powering, or at least recharging their internal batteries, by capturing ambient energy from the surrounding environment, such as random mechanical vibrations.
One of the primary performance limitations of energy harvesters for ambient mechanical vibrations is the suboptimal energy transfer from the mechanical source to the electrical load, often resulting from an impedance mismatch between the mechanical and electrical domains [1,2].
Drawing inspiration from similar problems in RF engineering, we approach the design of efficient energy harvesters as a broadband filtering problem. We model the mass-spring system responsible for harvesting vibrational kinetic energy as a passband filter. It is well established in circuit theory that broadband filters can be constructed using reactive elements arranged in a ladder topology. Therefore, we consider a chain of mass-spring pairs that forms a multi-degree-of-freedom mechanical resonator, which, through mechanical-to-electrical analogies, is transformed into a ladder network of LC resonators arranged in a Cauer topology.

Materials and Methods
We consider the multi degrees of freedom (DoF) energy harvester schematically represented in Fig. 1. Using mechanical-to-electrical analogies, we replace mechanical quantities like position, velocity, forces and so on, with equivalent electrical quantities, like charge, currents, voltages etc., deriving the equivalent circuit for the harvester shown in Fig. 2.
The transfer function $H(f) = \hat{V}_{in}/\hat{V}_{out}$ for the equivalent circuit is easily calculated for any number of stages in the ladder of LC networks. Assuming that the input force $f_{in}(t)$ modeling mechanical vibrations is a random force with power spectral density (PSD) $S_{in}(f)$, the PSD for

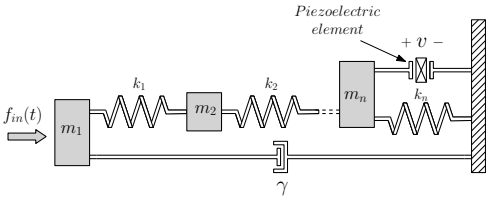

Figure 1: Schematical representation of a multi-degree-of-freedom energy harvester.

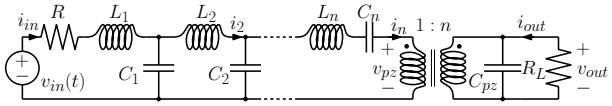

Figure 2: Equivalent circuit for the multi-degree-of-freedom energy harvester.

the output voltage is:

$$S_{out}(f) = |H(f)|^2 S_{in}(f) \tag{1}$$

The total power is given by the integral of $S_{out}(f)$ over all frequencies, and it is used as the goal function for the flock of starlings optimization algorithm [3].

Results

We have used the total harvested power as the goal function for the flock of starlings optimization of the equivalent circuit representing the multi-degree-of-freedom energy harvester. The objective is to find the parameters L_1, $C_1, \ldots, L_n, C_n$ in the ladder of LC circuits that maximize the harvested power. Because the goal function is known only through the solution of an integral equation, closed form, analytical formulas for the harvested power and its derivatives are not available. Therefore, gradient based methods are ill-suited for the problem.

Fig. 3 shows the result of the optimization for the harvester with two degrees-of-freedom. The flock-of-starlings method proves efficient and well suited to the problem. We have applied the flock-of-starlings optimization method to harvester with up to four degrees-of-freedom, proving that increasing the number of mass-spring pairs doubles the scavenged power with respect to a single degree of freedom system.

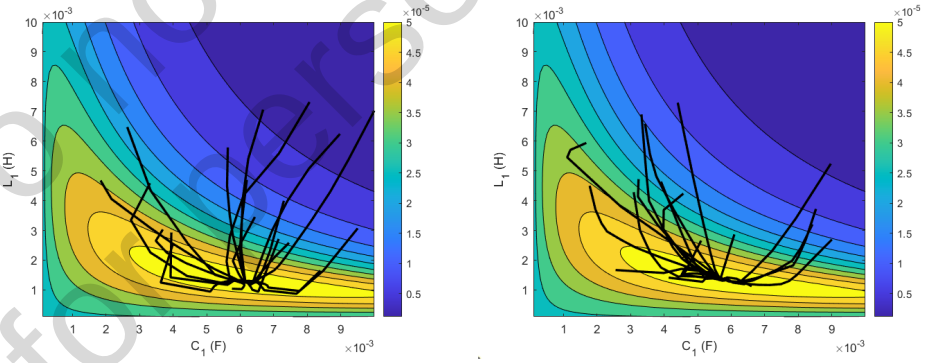

Figure 3: Trajectories of the flock-of-starlings optimization in the parameter space for a two DoF energy harvester.

References

1. M. Bonnin et al., “Leveraging circuit theory and nonlinear dynamics for the efficiency improvement of energy harvesting”, Nonlinear Dynamics, vol. 104, no. 1, , 2021, pp. 367-382.
2. K. Song et al., “Stochastic analysis of a bistable piezoelectric energy harvester with a matched electrical load”, Nonlinear Dynamics, vol. 111, 2023, pp. 316991-17005.
3. N. Netjinda et al, “Particle swarm optimization inspired by starlings flock behavior,” Applied Soft Computing, vol. 35, 2015, pp. 411–422.

Link between Continuous and Discrete Descriptions of Noise in Nonlinear Resistive Electrical Components

L. Désoppi[1], B. Reulet[1]

[1]Département de physique, Université de Sherbrooke, Sherbrooke QC, Canada

lucas.desoppi@usherbrooke.ca

bertrand.reulet@usherbrooke.ca

Abstract: We reconsider the modeling a nonlinear resistive electrical component using two models: i) a continuous description based on a stochastic differential equation with a white thermal Gaussian noise; ii) a discrete, shot noise model based on a Markovian master equation. We show that thermodynamics imposes in i) the use of the Hänggi-Klimontovich (H-K) prescription when the noise depends on bias voltage, and implies a generalized Johnson-Nyquist relation for the noise where the differential conductance is replaced by the ratio mean current over voltage. In ii) we show that the discrete description compatible with thermodynamics leads to the continuous one of i) with again the H-K prescription. Here the generalized Johnson-Nyquist relation for noise is recovered only at low voltage, when the continuous description is valid.
Keywords: Shot Noise, Hänggi-Klimontovich Prescription, Johnson-Nyquist Relation, Brillouin Paradox

Introduction. Models of noise in resistive electrical components must be compatible with thermodynamics, otherwise they lead to unphysical predictions such as the Brillouin paradox [4], an incarnation of Maxwell's demon in electronic systems. So far, two main models have been mostly considered: the Johnson-Nyquist model and the shot noise model. While the former is valid only for linear resistors, the latter approach makes it possible to describe nonlinear components, but at the cost of greater theoretical difficulty.
In this work, we reconsider the possibility of modeling a nonlinear resistor by means of Gaussian white noise. The use of stochastic differential equations in the presence of multiplicative noise then raises the question of the choice of an interpretation, the most common being those of Itō and Stratonovich [5]. We show that, in line with a previous study, such an approach is possible, but provided that we use the H-K prescription, and impose a generalized Johnson-Nyquist relation. The calculation is carried out for a resistive component in parallel with a linear capacitor. Two versions of the Brillouin paradox are then presented, considering either a deviation from the generalized Johnson-Nyquist relation, or a prescription different from that of H-K.
Two questions then arise: how should the use of the H-K prescription be interpreted? To what extent should the generalized Johnson-Nyquist relation be verified? To answer these two questions, we establish a link between the previous approach and the shot noise model. To do this, we write a master equation, which is suitably expanded to derive a Fokker-Planck equation, establishing the diffusion approximation of the shot noise. The latter depends on a parameter $\tilde{\alpha} \in [0, 1]$ linked to causality. We show that the choice $\tilde{\alpha} = 1/2$, discussed earlier, avoids the appearance of the Brillouin paradox, and corresponds exactly to H-K's prescription. Finally, we show that the local detailed balance (LDB) condition implies that the generalized Johnson-Nyquist relation must be asymptotically verified.

Continuous, Gaussian Noise Model. Let us consider a resistive element in parallel with a

capacitor C. The charge across the capacitor is denoted Q_t and the voltage U_t. If we model the resistive element using Gaussian white noise (derived from a Wiener process W_t), the voltage U_t satisfies a stochastic differential equation (SDE) of the form

$$C\mathrm{d}U_t = -\mathcal{I}(U_t)\mathrm{d}t - \mathcal{J}(U_t)\mathrm{d}W_t, \tag{1}$$

where $\mathcal{I}(u)$ gives the deterministic $I(V)$ curve, and $\mathcal{J}(u)$ describes the multiplicative noise, depending on the bias voltage. This SDE can be associated with a Fokker-Planck equation with prescription $\alpha \in [0,1]$ ($\alpha = 0$ and $1/2$ correspond to Itō and Stratonovich prescriptions respectively). At thermal equilibrium, the probability current must vanish, and the probability distribution must follow the Maxwell-Boltzmann statistic, i.e. $P_{\mathrm{eq}}(u) \propto \exp(-Cu^2/2k_{\mathrm{B}}T)$ (k_{B} being the Boltzmann constant and T the temperature). The combination of these two conditions leads to the following equation :

$$-\mathcal{I}(u) + \mathcal{J}(u)\mathcal{J}'(u)(\alpha-1)/C + u\big(\mathcal{J}(u)\big)^2/(2k_{\mathrm{B}}T) = 0. \tag{2}$$

We must also take into account the fact that the choice of capacitor is independent of the choice of resistive component. Thus, the functions $\mathcal{I}(u)$ and $\mathcal{J}(u)$ should not depend on C. Due to equation (2), choosing $\alpha \neq 1$ enforces the linearity of the resistor, that is $\mathcal{I}(u) = Gu$ for a certain conductance $G > 0$, and implies the usual Johnson-Nyquist relation $\mathcal{J}(u) = \sqrt{2k_{\mathrm{B}}TG}$ [1]. However, the possibility $\alpha = 1$ remains, directly leading to the generalized Johnson-Nyquist relation $\mathcal{J}(u) = \sqrt{2k_{\mathrm{B}}T\mathcal{I}(u)/u}$, and to the condition $\mathcal{I}(u)/u > 0$. Taking $\alpha = 1$ corresponds to the H-K prescription, already encountered for modeling fluctuations in a mesoscopic heat-engine [3].

Discrete, Shot Noise Model. When the noise generated by the resistor is modeled by a Markov jump process, the voltage takes discrete values $u_n = q_{\mathrm{e}}n/C$, with $n \in \mathbb{Z}$ with a probability $P(u_n, t)$ which obeys (writing $u = u_n$ and $v = q_{\mathrm{e}}/C$) [1, 2] :

$$\begin{aligned}\dot{P}(u,t) = {} & \lambda_-\big(u-(\tilde{\alpha}-1)v\big)P(u+v,t) + \lambda_+\big(u+(\tilde{\alpha}-1)v\big)P(u-v,t) \\ & - \Big[\lambda_+(u-\tilde{\alpha}v) + \lambda_-(u+\tilde{\alpha}v,t)\Big]P(u,t).\end{aligned} \tag{3}$$

Here $\lambda_\pm(u)$ are the jump rates, which satisfy the Local Detailed Balance condition $\lambda_+(u)/\lambda_-(u) = \mathrm{e}^{q_{\mathrm{e}}u/k_{\mathrm{B}}T}$. The parameter $\tilde{\alpha} \in [0,1]$ describes the causality: $\tilde{\alpha} = 0$ corresponds to the jump depending on the initial state only, while for $\tilde{\alpha} = 1$ only the final state matters. Expanding equation (3) up to order two in v yields a Fokker-Planck equation with the correspondence $\alpha = 2\tilde{\alpha}$. The midpoint rule $\tilde{\alpha} = 1/2$ is necessary to avoid Brillouin paradox [1, 2], and corresponds to the H-K prescription $\alpha = 1$, in agreement with the result of the preceding section. The noise is given by $\mathcal{J}(u) = \sqrt{q_{\mathrm{e}}\mathcal{I}(u)\coth(q_{\mathrm{e}}u/2k_BT)}$ with $\mathcal{I}(u) = q_{\mathrm{e}}[\lambda_+(u) - \lambda_-(u)]$. The generalized Johnson-Nyquist relation is verified only at low voltage $|u| \ll k_BT/q_{\mathrm{e}}$.

References

1. J. L. Wyatt Jr *et al.* "Nonlinear Device Noise Models: Satisfying the Thermodynamic Requirements", IEEE Transactions on Electron Devices, vol. 46, n. 1, 1999.
2. N. Freitas *et al.* "Stochastic Thermodynamics of Nonlinear Electronic Circuits: A Realistic Framework for Computing Around kT", Phys. Rev. X 11, 031064 (2021).
3. B. Sothmann *et al.* "Rectification of thermal fluctuations in a chaotic cavity heat engine", Phys. Rev B 85, 205301 (2012).
4. L. Brillouin. "Can the Rectifier Become a Thermodynamical Demon?", Phys. Rev. 78, 627 (1950).
5. N. G. van Kampen, Stochastic Processes in Physics and Chemistry. New York: North–Holland, 1992.

Thermodynamically consistent noise modeling in nonlinear circuits

M. Bonnin[1], J.-C. Delvenne[2], L. Van Brandt[2], F. Traversa[3], F. Bonani[1]

[1]Department of Electronics and Telecommunications, Politecnico di Torino, Turin, Italy

[2]ICTEAM, Université catholique de Louvain, Ottignies-Louvain-la-Neuve, Belgium

[3]Memcomputing Inc, CA, US

michele.bonnin@polito.it

Abstract: Traditional attempts to extend the Nyquist-Johnson formula for thermal fluctuations to nonlinear dissipative elements have led to thermodynamically inconsistent models. In this work, we present a Langevin model for thermal noise in nonlinear dissipative elements, that is fully consistent with the laws of thermodynamics. The model accurately predicts the Boltzmann-Gibbs distribution at thermal equilibrium and ensures zero expected voltages and currents, thereby resolving the well-known Brillouin paradox and confirming compliance with the second law of thermodynamics.
Keywords: Thermal noise, nonlinear resistors, Johnson-Nyquist formula

Introduction. The renowned Nyquist-Johnson formula for thermal noise, established more than a century ago, describes the random electrical noise generated by the thermal motion of charge carriers (typically electrons) in a linear conductor or resistor due to its temperature. This formula can be derived by starting with the deterministic equation for a first-order circuit containing a linear resistor, adding a noise term to account for thermal fluctuations, and ultimately deriving a Langevin-type equation. However, when a similar approach is applied to circuits with nonlinear resistors, inconsistencies with fundamental principles of statistical mechanics and thermodynamics emerge [1].

One of the most significant contradictions is the Brillouin paradox. Due to incorrect modeling of thermal noise, a nonlinear element, such as a diode, appears to rectify its own thermal fluctuations, enabling the extraction of energy from a system at thermal equilibrium. This results in a violation of the second law of thermodynamics, effectively creating a perpetual motion machine [2].

In this work, we propose a model for thermal noise in nonlinear circuit elements that is consistent with the fundamental laws of statistical mechanics and thermodynamics. Using a first-order circuit as an example, we demonstrate that the proposed model correctly predicts that, at thermal equilibrium, the state variable follows a Boltzmann-Gibbs distribution. We also show that the model resolves the Brillouin paradox, proving that the expected voltages and currents are null. Finally, we show that the novel formula reduces to the Nyquist-Johnson formula in the limit of a linear resistor, confirming that the latter is a special case of the new model.

Materials and Methods. We consider the first order circuit shown in Figure 1 composed by the series connection between flux controlled voltage source, a current controlled nonlinear resistor, and a flux controlled nonlinear inductor. The random voltage source is a unit white Gaussian noise, modulated by a flux dependent function $h(\varphi)$ to be determined. This electrical network is the equivalent of a nonlinear Brownian ratchet system [3].

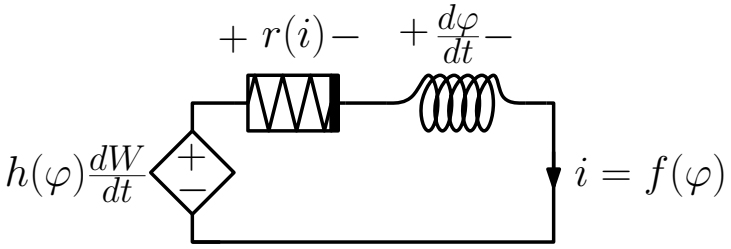

Figure 1: First order circuit used in the analysis

Results. Using Kirchhoff's voltage law, we derive the stochastic differential equation governing the circuit dynamics. This equation is interpreted as an Itô equation, and the corresponding Fokker-Planck equation is derived. The stationary solution is then obtained under the assumption of standard zero-flux conditions [4], yielding the following stationary probability distribution:

$$\rho_{st}(\varphi) = \frac{A}{h^2(\varphi)} \exp\left(-2 \int \frac{r(f(\varphi))}{h^2(\varphi)} d\varphi\right) \tag{1}$$

where A is a normalization constant. By requiring that the stationary distribution coincides with a Gibbs distribution, we determine the correct expression for the undetermined function $h(\varphi)$:

$$h(\varphi) = \left[-2 \exp\left(\frac{1}{kT} E(\varphi)\right) \int r(f(\varphi)) \exp\left(-\frac{1}{kT} E(\varphi)\right) d\varphi\right]^{1/2} \tag{2}$$

where $E(\varphi)$ represents the energy stored in the inductor.
Using (1) and (2), we can verify that the expected voltage across and the current through each element of the circuit are zero. Furthermore, it is possible to show that, for a linear resistor with the characteristic $v = Ri = Rf(\varphi)$, (2) reduces to $h(\varphi) = \sqrt{2kTR}$ which is the well-known Nyquist-Johnson formula.

References

1. J. Wyatt et al., "Nonlinear Device Noise Models: Satisfying the Thermodynamic Requirements", IEEE TRANSACTIONS ON ELECTRON DEVICES, vol. 46, n. 1, 1999, pp. 184-193.
2. L. Brillouin, "Can the Rectifier Become a Thermodynamical Demon?", Physical Review, vol. 78, 1950, pp. 627-628.
3. R.P. Feynman, "The Feynman Lectures on Physics", Vol. 1, Addison-Wesley, 1963.
4. C.W. Gardiner, "Handbook of Stochastic Methods", Springer, 2004.

Noise Propagation and Statistic Variability in MOSFETs Using Probability Density Functions

R. Chatzipantelis, L. Chevas, N. Makris, M. Bucher
School of Electrical and Computer Engineering, Technical University of Crete, 73100 Chania, Greece
mbucher@tuc.gr

Abstract: Probability density functions using stochastic methods [1] are shown to be an effective tool in the context of MOSFET noise and variability modeling. These methods are employed here in the context of the charge-based MOSFET model [2]. As an example, a Gaussian noise density function applied at the gate of a MOSFET causes a corresponding drain current noise, which may be expressed analytically as a function of inversion coefficient only. The same expression may be used to model drain current variability due to MOSFET parameters such as threshold voltage. The method shows promise in the variability modeling of MOSFETs and may complement traditional approaches [3][4].
Keywords: charge-based model, fluctuation, MOSFET, noise, probability density function, variability

Introduction: It is known that every power supply comes with its own type of noise, affecting the operation of electronics powered by it. In the case of a MOSFET, the working region is typically derived from the applied voltages. What happens if the gate voltage bias (V_G) is not constant, but follows a Gaussian type of noise $\left(V_G \sim \mathcal{N}\left(\mu_{V_G}, \sigma^2_{V_G}\right)\right)$?

Methods: The charge-based model provides us with the required equations to relate applied voltages to the mobile charge in the MOSFET channel and hence the drain current, transconductances, etc. The pinch-off voltage V_P depends on gate voltage V_G, threshold voltage V_{TO} and slope factor n as $V_P \approx \frac{V_G - V_{TO}}{n}$. Voltages are normalized to thermal voltage U_T as $u_P = \frac{V_P}{U_T}$ and $u_{S(D)} = \frac{V_{S(D)}}{U_T}$. The relationship among mobile charge and applied voltages is,

$$u_P - u_S = 2q_S + ln(q_S) \iff q_S = g_1(u_P - u_S) = \frac{1}{2} \cdot W(2e^{u_P - u_S}) \tag{1}$$

where q_S is the mobile (inversion) charge at the source and W is the $LambertW$ function. Since q_S is derived from u_P through the function g_1, it is obvious that the previous equation describes the inverse function of g_1, $u_P = g_1^{-1}(q_S) + u_S = 2q_S + ln(q_S) + u_S$.
The drain current of the MOSFET in saturation is then obtained as,

$$I_{Sp} = I_0 \cdot \frac{W}{L},\ i_f = \frac{I_D}{I_{Sp}} \text{ and } i_f = q_s^2 + q_s \iff q_S = g_2^{-1}(i_f) = \sqrt{\frac{1}{4} + i_f} - \frac{1}{2} \tag{2}$$

where $I_0(W/L)$ is the current normalization factor.
Using the change of variables technique the Probability Density Functions (PDF) of q_S and i_f are derived as such:

$$f_{q_S}(q_S) = \frac{1}{\sigma_{u_P}\sqrt{2\pi}} \cdot exp\left(-\frac{1}{2\,\sigma^2_{u_P}}\left(2q_S + ln(q_S) + u_S - \mu_{u_P}\right)^2\right) \cdot \frac{2q_S + 1}{q_S} \tag{3}$$

$$f_{i_f}(i_f) = \frac{1}{\sigma_{u_P}\sqrt{2\pi}} \cdot exp\left(-\frac{1}{2\,\sigma^2_{u_P}}\left(2\sqrt{\frac{1}{4} + i_f} + ln\left(\sqrt{\frac{1}{4} + i_f} - \frac{1}{2}\right) + u_S - \mu_{u_P} - 1\right)^2\right) \cdot \frac{1}{\sqrt{\frac{1}{4} + i_f} - \frac{1}{2}} \tag{4}$$

where μ_{u_P} and σ_{u_P} are the mean pinch-off voltage and its standard deviation. Hence f_{q_S} and f_{i_f} are analytical functions of i_f (or q_S) only. Note that if a perturbation is applied at the source, the same PDFs apply accordingly.

The main interest lies in the mean value and variance of these PDFs. Unfortunately, computing those integrals $\left(E[X], E\left[X^2\right], X = q_S, i_f\right)$ poses a significant challenge, therefore another method of obtaining these values must be used. Usually, the variance of our power source can be precisely measured, both μ_{V_G} and $\sigma^2_{V_G}$ are known, and μ_{u_P} and $\sigma^2_{u_P}$ can be computed as:

$$\mu_{u_P} = \frac{V_G - V_{TO}}{U_T \cdot n} = \overline{u_P},\ \sigma^2_{u_P} = \frac{\sigma^2_{V_G}}{(U_T \cdot n)^2} \text{ and } \overline{q_S} = \frac{1}{2}W\left(2e^{\mu_{u_P} - u_S}\right) = \frac{1}{2}W\left(2e^{\overline{u_P} - u_S}\right) \tag{5}$$

Having obtained the mean and the standard deviation of u_P, a Taylor and Delta Method approximation may be used to calculate the mean value and variance of q_S and i_f respectively:

$$\mu_{q_S} \approx \frac{1}{2}W\left(2e^{\mu_{u_P} - u_S}\right) + \frac{1}{4}\frac{W\left(2e^{\mu_{u_P} - u_S}\right)}{\left[W\left(2e^{\mu_{u_P} - u_S}\right) + 1\right]^3} \cdot \sigma^2_{u_P} = \overline{q_S} + \frac{1}{4}\frac{2\,\overline{q_S}}{\left[2\,\overline{q_S} + 1\right]^3} \cdot \sigma^2_{u_P} \tag{6}$$

$$\mathrm{Var}(q_S) \approx \left(\frac{1}{2}\frac{W\left(2e^{\mu_{u_P} - u_S}\right)}{W\left(2e^{\mu_{u_P} - u_S}\right) + 1}\right)^2 \cdot \sigma^2_{u_P} = \frac{1}{4}\left(\frac{2\,\overline{q_S}}{2\,\overline{q_S} + 1}\right)^2 \cdot \sigma^2_{u_P} \tag{7}$$

$$\mu_{i_f} \approx \mu^2_{q_S} + \mu_{q_S} + \sigma^2_{q_S} \iff \mu_{i_f} - \sigma^2_{q_S} = \mu^2_{q_S} + \mu_{q_S} \tag{8}$$

$$\mathrm{Var}(i_f) \approx \left(2\mu_{q_S} + 1\right)^2 \cdot \sigma^2_{q_S} = \left[4\left(\mu_{i_f} + \sigma^2_{q_S}\right) + 1\right] \cdot \sigma^2_{q_S} \tag{9}$$

Results: Figure 1 illustrates that the consideration of drain current (i_f) as a stochastic process -derived from the stochastic process of gate voltage (V_G) - can adequately predict the device variability, using the charge-based MOSFET model.

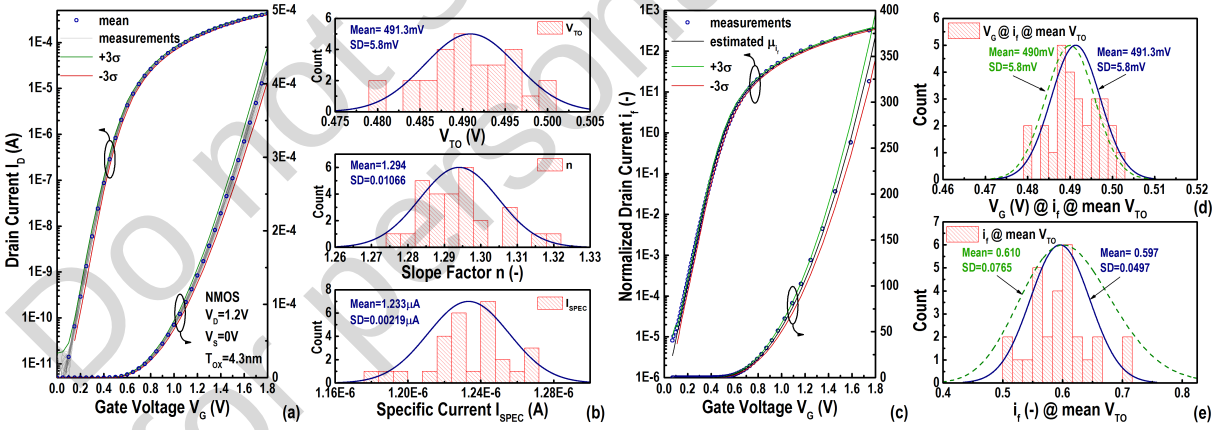

Figure 1: (a) 30 measured $I_D - V_G$ characteristics, mean and $\pm 3\sigma$. (b) Histograms of V_{TO}, n, I_{SPEC} (c) $i_f - V_G$ mean measured value, and estimated μ_{i_f} from (8) and σ_{i_f} from (9). (d) V_G histogram at threshold, with gaussian equivalent (reverse process $f_{i_f|approx}(i_f) \implies f_{V_G|approx}(V_G)$). (e) i_f histogram and corresponding gaussian at mean threshold with its stochastic counterpart.

References

[1] A. Papoulis, S. Pillai, Probability, Random Variables, and Stochastic Processes, McGraw Hill, 2002.

[2] C. Enz, E. Vittoz, Charge-based MOS Transistor Modeling, Wiley, 2006.

[3] C. C. McAndrew, "Efficient Statistical Modeling for Circuit Simulation", in Design of System on a Chip, Ed. R. Reis, J. Jess, Kluwer, 2004.

[4] R. Lavieville et al., "Statistical Characterization of Drain Current Local and Global Variability in sub 15nm Si/SiGe Trigate pMOSFETs", Proc. of ESSDERC, 2016, pp. 142-145.

X-Rays impact on Generation-Recombination Low-Frequency Noise components for advanced Si/SiGe:C HBTs

B. Sagnes[1], M. Bouhouche[1], A. Hoffmann[1], J. Boch[1], T. Maraine[1], S. Haendler[2], P. Chevalier[2], D. Gloria[2], F. Pascal[1]

[1]IES, University of Montpellier, CNRS, 34095 Montpellier, France
[2]STMicroelectronics, 850 rue Jean Monnet, 38926 Crolles Cedex, France

Abstract: This study presents an investigation of X-ray dose impact on Low Frequency Noise Generation-Recombination components for NPN Si/SiGe:C heterojunction bipolar transistors (HBTs) developed in two BiCMOS technologies. Generation-Recombination, G-R, components are examined in detail both before and after irradiation. Compact modelling for these excess noise components is established after X-ray exposure. They are studied over the irradiation process as a function of current biases and geometrical parameters to locate the noise sources. A thermal annealing process at two temperatures, 100°C and 130°C, is accomplished to investigate any possible healing effects on Low Frequency Noise spectra.

Keywords: Generation-Recombination Noise (G-R), Si/SiGe HBTs, Total Ionizing Dose (TID).

Introduction The main purpose of this work is to investigate the impact of X-Ray irradiations on advanced Si/SiGe:C HBTs supplied by STMicroelectronics (B9MW and B55 technologies). Low Frequency Noise (LFN) measurements are performed during the X-Ray irradiation process and, even if in the literature LFN is mainly associated with the study of the 1/f noise components, here we investigate the evolution of Generation-Recombination (G-R) components in terms of cut-off frequency and plateau magnitude of the lorentzian spectra.

For LFN measurements, HBTs are biased in a common emitter configuration. On-wafer contacts are established using coplanar probes. The input base current fluctuations are directly measured. The spectral density of the base current, S_{IB}, is measured using a low noise current-voltage amplifier (EG&G 5182) and a spectrum analyzer (HP 89410A). Spectra are measured in a frequency range of 10 Hz–100 kHz. The irradiations are performed using the X-ray facility from the University of Montpellier PRESERVE platform. Ten irradiation steps are performed until reaching a Total Ionizing Dose (TID) of 151 krad. During this study, the irradiation process is performed at room temperature on unbiased HBTs.

Pre-rad Low Frequency Noise In advanced Si based transistors, i.e. in nanoscale CMOS [1] or in advanced bipolar [2], the presence or not of G-R components is very often random and multi-parameter dependent: bias, temperature, geometry, technological step. To illustrate the dispersion in the LFN spectra induced by G-R components (“bumps”), we reported, in Fig. 1, spectra measured for the same base current on 6 dice of the same B55 HBT (A_E = 4.2 µm² and I_B = 100 nA). The 1/f noise component could be hidden by the presence of the G-R components. As reported in the inset of Fig. 1 (temporal domain), these G-R components are regularly associated with Random Telegraph Signal noise (RTS). Two G-R components are identified. The first one is detected around 20 Hz and the second one in the range of 200 Hz.

X-ray irradiations effects on G-R components After a TID of 26 and 91 krad, for B9MW and B55 respectively, 1/f noise components are systematically dominated by the presence of G-R components. An example is given in Fig. 2 for the B9MW technology. Evolution of the lorentzian parameters (cut-off frequency and plateau magnitude) versus bias and geometrical parameters can help to locate the traps responsible of the G-R components. After irradiation exposure, the modelled spectral density of the two G-R components is written as:

$$S_{I_{B_{post\_rad}}}^{G-R} = S_{I_{B_{pre\_rad}}}^{G-R} + \frac{A_1'}{1+\left(\frac{f}{f'_{c1}}\right)^2} + \frac{A_2'}{1+\left(\frac{f}{f'_{c2}}\right)^2} \quad (1)$$

where A_i' and f_{ci}' represent the induced G-R magnitude and cut-off frequency respectively after irradiation exposure.

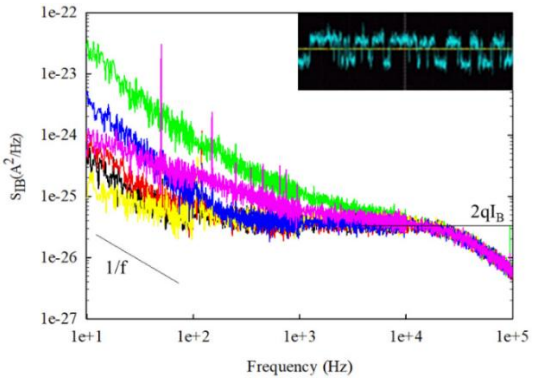

Fig. 1: Illustration of spectra dispersion for 6 HBTs with the same geometry of the B55 technology. Inset: time record showing a RTS signature.

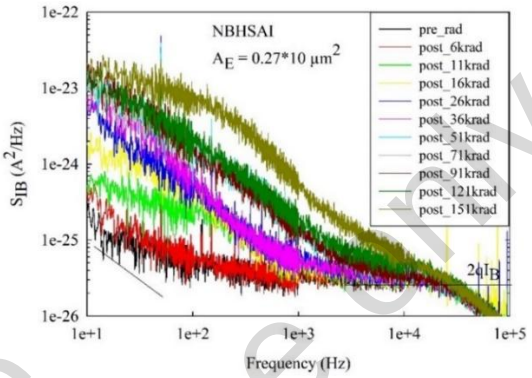

Fig. 2: Example of S_{IB} spectra for I_B = 100 nA, after X-ray exposure.

G-R parameters vs TID Independently to the irradiation dose, the spectra analysis resulted in two lorentzian at maintained stable f_c values (i.e. fc ~ 20 Hz and 200 Hz) for both technologies. Concerning the plateau, that means the two normalized lorentzian amplitudes, the B55 HBTs presented an independency to the irradiation dose by maintaining a stable magnitude level. On the other hand, a linear increase of the magnitude as a function of the dose characterizes the B9MW HBTs. This phenomenon can be related to the activation mechanism of new trap centres after each irradiation step.

G-R parameters vs base current and emitter geometries Plateau evolution as a function of base current bias and emitter geometries lead for the first lorentzian plateau to the model as followed:

$$A'_1 = K_{GR}\frac{1}{P_E}I_B^2 + K_{GR}{}'\frac{1}{P_E}I_B \quad (2)$$

as for the second lorentzian plateau magnitude, it is expressed as followed;

$$A'_2 = K_{GR}\frac{1}{P_E}I_B^{\alpha} + K_{GR}{}'\frac{1}{P_E}I_B \qquad (1 < \alpha < 2) \quad (3)$$

Annealing at 100 °C and 130 °C We observed a healing effect in the lorentzian spectra that led to a recovery of the G-R component for the higher cut-off frequency range. The healing effect recorded on the first G-R component is less important comparing to the second one. Since the annealing process is responsible for evacuating the induced trapped charges located in the E-B area, we can confirm that many trap centers are created in the oxides of the E-B junction.

References

[1] C. Theodorou and G. Ghibaudo, 25th International Conference on Noise and Fluctuations - ICNF 2019 - Neuchâtel (Suisse) (18-21 Juin 2019) DOI: 10.5075/epfl-ICLAB-ICNF-269239
[2] M. Seif, F. Pascal, B. Sagnes, A. Hoffmann, S. Haendler, P. Chevalier, D. Gloria, Microelectronics Reliability (2014) volume 54, n°9–10, p. 2171 - 2175 DOI: 10.1016/j.microrel.2014.07.027.

Gas sensing by flicker noise in Au-decorated graphene layers modulated by plasmonic resonance

J. Smulko, K. Drozdowska

Department of Metrology and Optoelectronics, Faculty of Electronics, Telecommunications and Informatics, Gdańsk University of Technology, Gdańsk, Poland
janusz.smulko@pg.edu.pl

Abstract: Flicker noise can be utilized for enhanced gas sensing by the sensors made of graphene flakes decorated with Au nanoparticles. Gas molecules adsorb-desorb in the vicinity of Au nanoparticles and generate low-frequency noise component - Lorentzian. Flicker noise can be observed in gas sensors due to relatively low resistance and high bias current exposing resistance fluctuations in graphene flakes. Au nanoparticles modify the observed flicker noise because of ambient gas molecules' continuous adsorption-desorption processes. This effect can be modulated by plasmonic resonance phenomena in Au nanoparticles when irradiated by adequate light wavelengths. The plasmonic resonance phenomena induce additional charge within Au nanoparticles, which can be transferred into the graphene layer. The charge transfer process depends on the ambient atmosphere around the irradiated nanoparticle, which can be utilized for gas sensing. We present some experimental results how this process can be enhanced to improve gas sensing by flicker noise measurements and analysis, considering its intensity and slope versus frequency.

Keywords: flicker noise, plasmonic resonance, gas sensing, graphene, noble metals

Introduction Gas sensing is a rapidly developing area investigating various materials and phenomena to reach gas sensors with high selectivity, sensitivity, and stability at reduced production costs and detection measurement [1,2]. It is not easy to achieve all these aims at the same time. One of the methods utilizes flicker noise measurements and is very efficient for low concentrations of gases [3,4]. Unfortunately, it suffers from limited selectivity and stability in time, and further enhancement is necessary. We propose utilizing Au nanoparticles with catalytic properties and enhancing gas sensing as presented elsewhere [5]. Au nanoparticles exhibit plasmonic resonance when irradiated by the light of selected wavelengths (e.g., yellow light), affecting flicker noise [6] and inducing gas sensing properties [7]. Typically, we consider the changes of optical parameters or current-voltage characteristics for gas sensing detection in such structures [8]. Our approach utilizes flicker noise that can be much easier measured than optical changes but is very sensitive to even subtle changes in ambient atmosphere of such gas sensor [9]. Moreover, the plasmonic resonance is introduced by light irradiation, using commercial LED as a light source what makes the sensing platform very convenient for mobile applications with limited energy consumption and low-cost sensor and measurement unit.

Materials and methods We considered the sensors prepared by ink-printing technology on the commercially available ceramic substrate with interdigitated electrodes. The sensors were printed using an ink comprised of graphene flakes, TiO_2 and Au nanoparticles. Such layer can be easily prepared by mixing the ingredients and printing on the interdigitated electrodes, and annealing at elevated temperature to stabilize its parameters. The layer comprises of three different components: graphene, Au nanoparticles, and TiO_2 nanoparticles. Each of these elements can be modulated by different irradiation: UV light enhancing graphene layer and TiO_2 nanoparticles, green light inducing plasmonic resonance in Au nanoparticles.

Results We observed the Lorentzian at low frequency range (f_c ~ 100 Hz) when the sample was at dark. Its intensity was sensitive to ambient atmosphere, and was reduced when we introduced oxidizing NO_2 gas (Fig. 1). The observed Lorentzian was sensitive to plasmonic resonance phenomena, induced by green light (515 nm) and taking place in Au nanoparticles. It disappeared at corner frequency f_c ~ 100 Hz, and shifter into higher frequencies (f_c ~ 800 Hz) but at lower intensity than observed at dark. Again, we noticed its further reduction when NO_2 gas was introduced. Our experimental studies confirmed gas sensitivity to other gases but of various intensity, and different impact of plasmonic resonance. We conclude that an impact of ambient gas and green light inducing plasmonic phenomena on the observed Lorentzian can be utilized to enhance gas detection. We underline that the Lorentzian was visible within a few months of experimental studies what makes the proposed method attractive for eventual practical applications. Additionally, we observed Lorentzian induced by UV irradiation at higher frequencies but related to photocatalytic properties of the introduced TiO_2 nanoparticles and photoactivation of graphene surface.

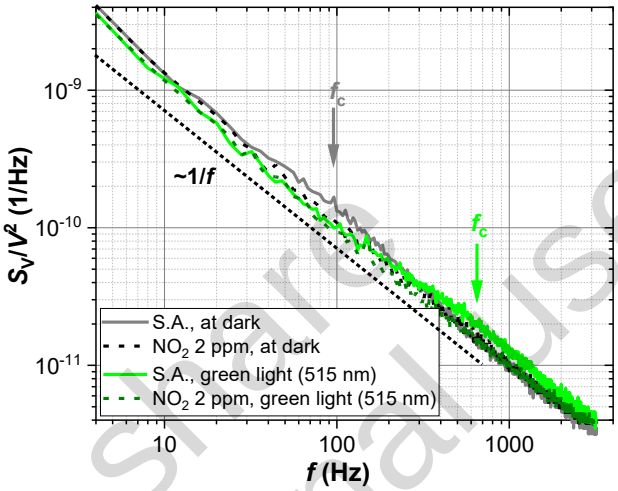

Fig. 1: Power spectral density of voltage fluctuations across the gas sensor $S_V(f)$ normalized to the square of its DC bias voltage V^2 versus frequency f with visible Lorentzians of corner frequency f_c.

References

[1] K. Zakrzewska, "Mixed oxides as gas sensors", Thin Solid Films, vol. 391, n. 2, 2001, pp. 229-238.
[2] G. Korotcenkov, "Gas response control through structural and chemical modification of metal oxide films: state of the art and approaches", Sensors and Actuators B: Chemical, vol. 107, n. 1, 2005, pp. 209-232.
[3] L.B. Kish, R. Vajtai, C.G. Granqvist, "Extracting information from noise spectra of chemical sensors: single sensor electronic noses and tongues", Sensors and Actuators B: Chemical, vol. 71, n. 1-2, 2000, pp. 55-59.
[4] A. Dziedzic, A. Kolek, B.W. Licznerski, Noise and nonlinearity of gas sensors–preliminary results. Proc. of the 22nd Int. Spring Seminar on Electronics Technology, Dresden-Freital, Germany, 18–20 May 1999.
[5] A.A. Balandin, "Low-frequency 1/f noise in graphene devices", Nature Nanotechnology, vol. 8, n. 8, 2013, pp. 549-555.
[6] J. Smulko, K. Drozdowska, A. Rehman, T. Welearegay, L. Österlund, S. Rumyantsev, P. Sai, "Low-frequency noise in Au-decorated graphene–Si Schottky barrier diode at selected ambient gases", Applied Physics Letters, vol. 122, n. 21, 2023.
[7] K.H. Park, S.H., Lee, C. Fàbrega, J.D. Prades, J.W. Jang, "Plasmon expedited response time and enhanced response in gold nanoparticles-decorated zinc oxide nanowire-based nitrogen dioxide gas sensor at room temperature", Journal of Colloid and Interface Science, vol. 582, 2021, pp. 658-668.
[8] V. Amendola, R. Pilot, M. Frasconi, O.M. Maragò, M.A. Iatì, "Surface plasmon resonance in gold nanoparticles: a review", J. Phys.: Condens. Matter, vol. 29, 2017, 203002.
[9] H. Hu, X. Yang, X. Guo, K. Khaliji, S.R. Biswas, F.J. García de Abajo, Q. Dai, "Gas identification with graphene plasmons", Nat. Commun., vol. 10, 2019, 1131.

The Stochastic Nature of Random Telegraph Noise

Francesco Maria Puglisi

DIEF, Università di Modena e Reggio Emilia, Modena, Italy - francescomaria.puglisi@unimore.it

Abstract: Lately, Random Telegraph Noise (RTN) has been deemed, via specific mathematical metrics, to be possibly deterministic-chaotic rather than stochastic, with severe implications for applications based on RTN stochasticity. Yet, this was claimed by analyzing a limited number of RTN traces. Here we analyze several RTN traces measured in different devices and conditions, mathematically generated traces, and traces resulting from advanced simulations of RTN in MIM structures. It is shown that the mathematical metrics employed to reveal the deterministic-chaotic nature of RTN are not robust enough to support that claim. Complex RTN is likely to result from inherently stochastic processes embedded in a deterministic multi-body system which could show stochastic chaos, but hardly any determinism.

Keywords: Random Telegraph Noise, stochastic, deterministic, chaotic, low-frequency noise, RRAM.

Introduction Random Telegraph Noise (RTN) measured in MOSFETs [1] and RRAMs [2] has recently been suggested to be not stochastic, as previously thought. By using specific metrics such as the correlation dimension in the context of the Grassberger-Procaccia method [1-3] and the Lyapunov spectrum [1-2], it was proposed that complex RTN could be deterministic-chaotic rather than stochastic [1-2]. This causes serious consequences for applications in which RTN's alleged true stochasticity is harnessed, e.g., true random number generators [4]. Yet, such a bold claim was derived by analyzing a very limited number of measured or mathematically generated RTN traces, undermining its strength. Here we analyze several RTN traces measured in different devices and conditions, mathematically generated RTN traces, and complex RTN resulting from advanced kinetic Monte-Carlo simulations of charge transport and trapping in MIM structures.

Experiments We measured, using a Keithley 4200-SCS, RTN traces in 28-nm bulk n-FinFETs, and HfO_2-based RRAMs. First, the device functionality was tested with I_D-V_G and I_D-V_D curves for FinFETs, and set/reset curves for RRAMs (not shown). Then, FinFETs at T = 30°C were biased at V_{GS} = 0.7V or 0.72V and V_{DS} = 0.5V, while the drain current was sampled every 7ms for 30s. RRAMs were driven in high resistive state using DC sweeps down to V_{RESET} = -0.9V, -1.0V or -1.1V and were then read at T ranging from 30°C to 70°C under a DC voltage V_{READ} ranging from 10mV to 50mV, with a sampling time of 2ms or 6ms for 20s or 60s, respectively.

Simulations Kinetic Monte-Carlo (KMC) 3D simulations were run using Ginestra® to simulate RTN in a TiN/(4nm)HfO_2/TiN cell. Oxygen vacancies (V, responsible for the current via trap-assisted tunneling - TAT) and ions (O, at which trapped charge can locally perturb the potential and modulate the current, promoting RTN [5]) are included. Defects and material parameters are consistent with earlier works [5]. We include Schottky and thermionic emission, TAT (with trap-to-trap contribution), direct and Fowler-Nordheim tunneling, and the trapped charge term in the Poisson equation [5]. In all simulations, the local field and temperature are used to evaluate the occupancy of defects and the current in the device. We also use mathematically-generated RTN using *i*) fixed dwell times, resulting in a non-chaotic deterministic RTN; *ii*) exponentially-distributed dwell times, resulting in a (pseudo-)random RTN.

Results We analyze each RTN trace by the equivalent phase space reconstruction as in [1-2], according to which the original system attractor and the reconstructed one are equivalent. The reconstructed attractor in the *m*-dimensional phase space (*m* being the embedding dimension) is used to calculate the correlation integral C_m for integer *m* up to 30. Using the Grassberger–Procaccia method, the slope, ν_m, of the linear part of C_m can be plotted vs. *m*, and it was suggested that if the curve saturates, the system is deemed to be chaotic. However, it has been

shown by counterexamples that this is not an actual law [3] which makes this method unsuitable to support claims about the stochastic or deterministic nature of RTN. Since another indication of (alleged) chaos is the presence of at least one positive Lyapunov exponent, we also calculated the highest Lyapunov exponent, L_m, for each *m*. By evaluating the above metrics on many RTN traces (measured, simulated, synthesized - with only some cases shown here, as full results will be shown in the full manuscript) discrepancies emerge. Specifically: *i*) both synthesized deterministic (Fig. 1 top-left) and (pseudo-)random (Fig. 1 bottom-left) RTN show a saturated ν vs. *m* curve and positive L_m, both suggesting chaos which yet is absent at least in the first signal; *ii*) RTN measured in n-FinFETs (Fig. 1 top-center) shows a saturated ν vs. *m* curve and negative L_m, thus the metrics are in contrast; *iii*) RTN measured in RRAMs (Fig. 1 bottom-center) always shows a saturated ν vs. *m* curve but L_m is found to be either positive or negative depending on the specific trace, which is again inconclusive; *iv*) simulations in which RTN results from trapping at just one isolated O ion (Fig. 1 top-right) show a non-saturated ν vs. *m* curve and positive L_m, with metrics again in contrast; while when multiple ions are present and sufficiently close to one another to influence each other's charge trapping dynamics, complex RTN emerge (Fig. 1 bottom-right) that show saturated ν vs. *m* curve and positive L_m, suggesting chaos. These discrepancies can be solved by recalling that *i*) those metrics are just indicative of chaos but not exact and, prominently, that chaos and stochasticity are not mutually exclusive (i.e., chaos is not necessarily deterministic) [3]; *ii*) RTN is due to tunneling, a purely quantum, thus stochastic, phenomenon; *iii*) defects electrostatic interactions set a complex multi-body problem [5], likely to show chaotic features, yet superposed to an inherent stochasticity for the above reasons. Complex RTN may thus be chaotic-stochastic, but hardly deterministic.

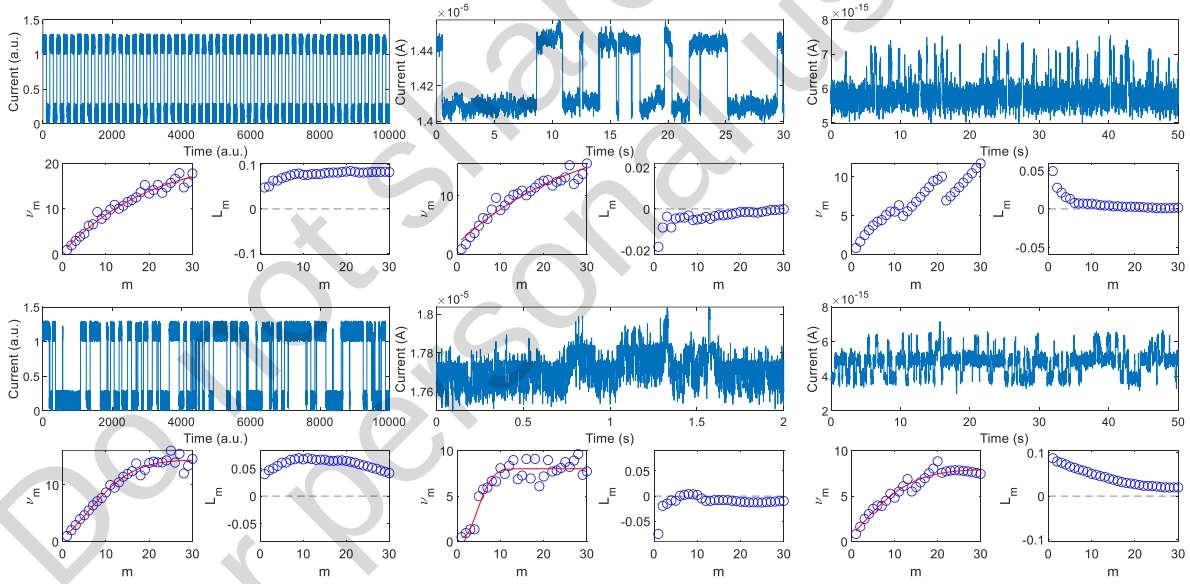

Fig. 1: RTN trace, ν vs. m curve and L_m vs. m curve for synthesized deterministic (top-left) and (pseudo-)random (bottom-left) RTN, RTN measured in n-FinFETs (top-center) and RRAMs (bottom-center), and simulated RTN with one isolated O ion (top-right) or multiple O ions (bottom-right).

Acknowledgments This study received funding from PNRR–M4C2INV1.5, NextGenerationEU - Avviso 3277/2021 - ECS_00000033 – ECOSISTER - Spoke 6 - CUP E93C22001100001.

References

[1] D. H. Tassis et al., IEEE EDL, vol. 38, no. 4, pp. 517-520, April 2017 - 10.1109/LED.2017.2672783
[2] S. G. Stavrinides et al., Chaos, Solitons & Fractals, vol. 160, 2022 (112224) - 10.1016/j.chaos.2022.112224
[3] M. Frey, Computational Stochastic Mechanics - Theory, Computational Methodology and Application, Elsevier Applied Science, London (1993)
[4] X. Li et al., Adv. Funct. Mater. 2021, 31, 2102172. - 10.1002/adfm.202102172
[5] S. Vecchi et al. IEEE T-ED, vol. 69, no. 12, pp. 6991-6998, Dec. 2022 - 10.1109/TED.2022.3213502

Low Frequency Noise Spectroscopy of GaAsBi QW Structures for NIR Light Sources

I. Pliaterytė[1], L. Dundulis[1], A. Špokas[2], A. Zelioli[2], M. Kamarauskas[2], A. Bičiūnas[2], J. Glemža[1], B. Čechavičius[2], S. Pralgauskaitė[1], R. Butkutė[2], J. Matukas[1]

[1]Institute of Applied Electrodynamics and Telecommunications, Vilnius University, Vilnius, Lithuania
[2]Center for Physical Sciences and Technology, Vilnius, Lithuania
sandra.pralgauskaite@ff.vu.lt

Abstract: Low frequency (10 Hz – 200 kHz) noise characteristics of GaAsBi light-emitting and laser diodes were investigated over the temperature range 159 K - 320 K. 1/*f*, $1/f^{\alpha}$, and Lorentzian type components make up the low frequency noise spectra of the investigated structures. Noise spectroscopy revealed that grown GaAsBi QW structures contain defects that redistribute current out of the active region of the diodes.

Keywords: GaAsBi, generation-recombination, LD, LED, NIR, noise, QW

Introduction Near-infrared (NIR) light sources in medical instruments (e.g., pulse oximeters) are highly significant. A specific radiation wavelength for such devices is very important, as there is a different penetration depth through the tissues for different wavelengths. However, the quality and lifetime of these devices used in the equipment are no less important.

Nowadays, light-emitting (LEDs) and laser diodes (LDs) are usually based on quantum structures, which increase efficiency and suppress radiation wavelength range. For a specific wavelength, which would be desirable to use in reflection mode pulse oximeters – 1100 nm, GaAsBi QW-based structures were investigated [1]. Peculiarities of GaAsBi QWs growth are low substrate temperature (<420 °C) and As to Ga beam equivalent pressure ratio is close to 1 [2,3]. These growth conditions cause a larger density of point defects and higher surface roughness, thus increasing the non-radiative recombination compared to the conventional AlGaAs quantum structures. Therefore, it is vital to investigate the influence of such defects and structural non-idealities on the electrical and optical characteristics of GaAsBi QW-based LEDs and LDs to increase the radiation efficiency and lifetime. Low frequency noise characteristics of semiconductor devices are very sensitive to the presence of various structural defects and imperfections and help clarify the origin of lower device quality or shorter lifetime [4,5].

Here, we present an investigation of low frequency noise characteristics of GaAsBi QW-based light-emitting diodes and laser diodes with the aim of finding out noise origins and give the feedback to technologists to improve the quality of GaAsBi QW structures.

Samples and methods Structures with GaAsBi rectangular quantum wells (RQWs) in the active region were grown using molecular beam epitaxy [1]. LDs and LEDs consisted of 3 and 5 RQWs, respectively, separated by GaAs barriers. The GaAsBi/GaAs active region was deposited at a substrate temperature of (340 – 360) C, while the cladding and contact layers were grown at a temperature typical for the growth of GaAs (440 – 580 °C). Radiation spectral peak positions of LEDs and LDs were registered in the range of (1070 – 1150) nm.

Current-voltage and low frequency (10 Hz – 200 kHz) electrical noise characteristics at forward and reverse bias have been measured at room temperature and over a temperature range from

159 K to 320 K. The absolute value of the spectral density of voltage fluctuation was calculated by comparing it to the reference resistance's thermal (Nyquist) noise [5].

Results Low frequency noise spectra of the investigated GaAsBi QWs-based LEDs and LDs comprise from $1/f$, $1/f^{\alpha}$, and Lorentzian type components both at forward and reverse bias. Clear Lorentzian-type bumps indicating intensive charge carrier generation and recombination processes were observed at specific current and temperature ranges, showing the activity of the charge carrier capture centers under these operation conditions. While $1/f$ and $1/f^{\alpha}$ type fluctuations were caused by the superposition of many generation and recombination processes of similar intensity through centers with widely distributed characteristic times.

A comprehensive investigation of current-voltage and noise characteristics of GaAsBi QWs-based LED structures under forward and reverse bias showed the correlation of noise intensity with the differential resistance, R_{diff}: for most samples, current fluctuation spectral density was proportional to the R_{diff}^{-2} (Fig. 1), what indicates deviation from an ideal *pn* junction, i.e., there is a current leakage channel, which redistributes current flow out of the active region.

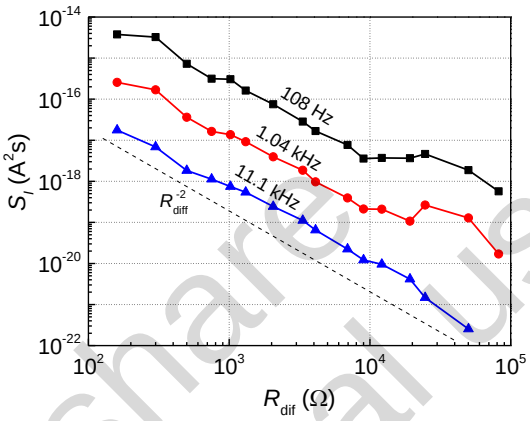

Fig. 1: Current noise spectral density dependency on the differential resistance of GaAsBi QWs-based LED measured at room temperature.

Low frequency noise spectroscopy revealed the activation energy of the observed active charge carrier capture centers of (0.31 – 0.33) eV, which can be caused by the lower growth temperature of the GaAsBi QWs. The adapted equivalent noise circuit for the investigated LD structure has shown that these defects are responsible for redistributing the flowing current between the active region and the adjacent layers of LD.

Summarizing, the low-frequency noise characteristics of the NIR LEDs and LDs based on GaAsBi QWs were investigated. It was found that structures contain the charge carrier capture centers formed by defects that cause current redistribution out of the active region. Such current leakage impacts radiation efficiency and can reduce the lifetime of the diodes.

References

[1] A. Štaupienė et al., "Internal quantum efficiency of GaAsBi MQW structure for the active region of VECSELs", Appl. Phys. Lett., vol. 125, 2024, 221102.
[2] R. D. Richards et al. "Molecular beam epitaxy growth of GaAsBi using As_2 and As_4", J. Cryst. Growth, vol. 39, 2014, pp. 120–124.
[3] J. Puustinen et al., "Analysis of GaAsBi growth regimes in high resolution with respect to As/Ga ratio using stationary MBE growth", J. Cryst. Growth, vol. 511, 2019, pp. 33–41.
[4] B. K. Jones, "Electrical noise as a reliability indicator in electronic devices and components", IEEE Proc. Circ. Dev. Syst., vol. 149, 2002, pp. 13–22.
[5] V. Palenskis et al., "InGaAs Diodes for Terahertz Sensing - Effect of Molecular Beam Epitaxy Growth Conditions", Sensors, vol 18, 2018, 3760.

1/f Noise study in second generation of 55 nm BiCMOS Si/SiGe:C HBTs

M. Bouhouche[1], B. Sagnes[1], A. Hoffmann[1], J. Boch[1], T. Maraine[1], A. Gauthier[2], P. Chevalier[2], D. Gloria[2], F. Pascal[1]

[1]IES, University of Montpellier, CNRS, 34095 Montpellier, France
[2]STMicroelectronics, 850 rue Jean Monnet, 38926 Crolles Cedex, France

Abstract: The purpose of this work is to characterize the 1/f noise in the latest 55nm BiCMOS SiGe:C Heterojunction Bipolar Transistors (HBTs) developed by STMicroelectronics (B55x). The presence of one or more G-R components can make it difficult to study noise in 1/f. To remedy this, we undertook a statistical study of over 100 transistors on 12 dies. Low frequency noise is studied over transistors with different geometries at different base current biases. The 1/f noise level shows a quadratic evolution with base current I_B and a $1/A_e$ dependence where A_e is the emitter area. The SPICE parameter K_F related to the 1/f noise amplitude as well as the figure of merit K_B are at least a half decade lower than the previous technology (B55). For instance, excellent K_B values close to 10^{-10} µm² are found.

Keywords: Heterojunction bipolar transistor (HBT), SiGe:C,1/f noise

Introduction The studied HBTs are supplied by STMicroelectronics Crolles and are issued from the development phase of a new 55 nm SiGe BiCMOS technology dedicated to various applications such as satcom, wireless cellular infrastructures, or optical communications (including AI clusters). Compared to the previous 55 nm technology (B55) this new one (B55x) offers significant changes in the process flow [1]. Very high frequency parameters are reached with f_T/f_{MAX} = 385/500 GHz. In this work, Low Frequency Noise (LFNoise) spectral analysis and 1/f noise characterization of a large number of transistors of different emitter area (single emitter finger of different width and length) is presented.

DC characteristics DC measurements have been performed on each device before LFNoise measurements. Fig.1 shows the evolution of the base current I_B, the collector current I_C and the current gain β versus the base-emitter voltage V_{BE} for a transistor with emitter area A_e = 0.2 x 1 µm². As can be seen, very high current gain, around 2000, is reached.

Spectral analysis Base current spectral density, S_{IB}, is measured in the 1 Hz – 100 kHz frequency range. Over 100 transistors were tested, and around 35% showed an identifiable 1/f noise component, either on all four bias currents as shown in Fig. 2, or on at least two current values (Fig. 3). For the remaining 65%, one or two G-R components (cut-off frequencies around 5-20 Hz and 200-400 Hz respectively) mask the 1/f noise. These dispersive behaviors are identical to previous results obtained with B55 technology [2] and with the 130 nm technology of Infineon [3].

1/f noise SPICE modelling 1/f noise base current spectral density S_{IB} is modelled according to the SPICE model using the classical relation:

$$S_{I_B} = K_F \frac{I_B^{A_F}}{f} \quad (1)$$

First, the study of S_{IB} at 1 Hz versus base current I_B allowed us to extract the value of A_F, the expected quadratic law was observed for all the transistors showing a 1/f noise component. Then K_F is calculated from equation 1 and plotted versus emitter area as reported in Fig. 4. In this figure, all emitter areas are shown, regardless of width or length. Despite a fairly wide

dispersion of the 1/f noise levels, the trend is towards $1/A_e$. The extraction of the 1/f noise figure of merit $K_B = K_F . A_e$ (estimated K_B values can be read directly from figure 4 for A_e = 1 µm²) gives excellent results with K_B ranging from 10^{-10} to 5 10^{-10} µm².This result is half a decade better than the previous version, and this, combined with superior HF performances, makes the new architecture of the B55x technology highly promising for the production high speed analog integrated circuits.

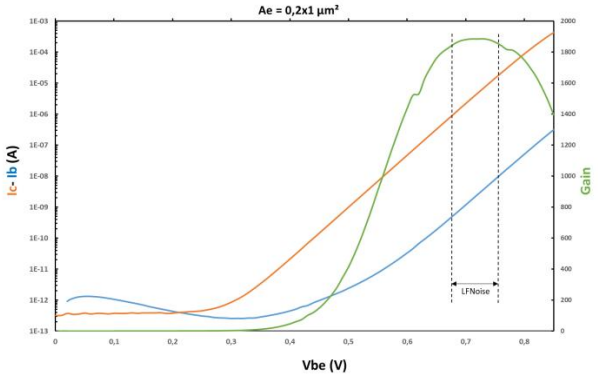

Fig. 1: Example of Gummel Plot.

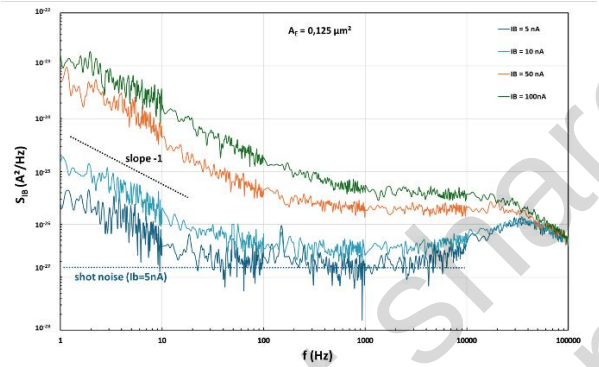

Fig. 2: G-R free S_{IB} spectra, A_e = 0.3 x 0.45 µm².

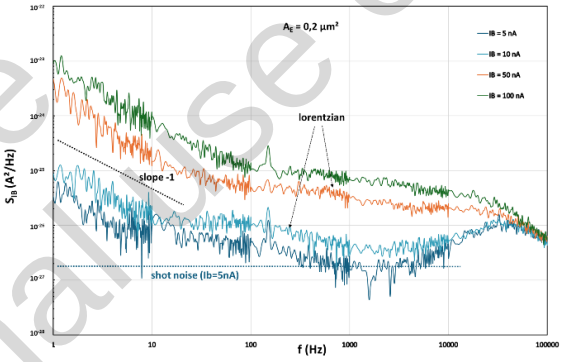

Fig. 3: S_{IB} Spectra showing the presence of one G-R component, A_e = 0.2 x 1 µm².

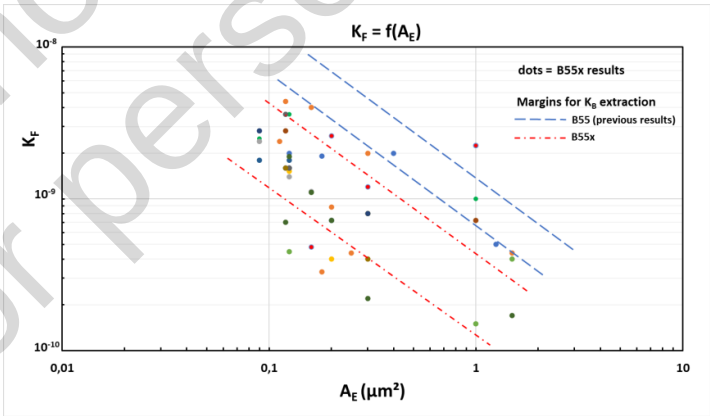

Fig. 4: Evolution of the 1/f noise parameter K_F vs emitter area A_e. Comparison with B55 [2].

References

[1] P. Chevalier et al., "A Versatile 55-nm SiGe BiCMOS Technology for Wired, Wireless, and Satcom Applications", IEEE BCICTS 2024, pp 13-17, *DOI: 10.1109/BCICTS59662.2024.10745707*

[2] J. El Beyrouthy et al.,"Low frequency noise characterization and modeling of SiGe HBT featuring LASER annealing in a 55-nm CMOS node", International Conference on Noise and Fluctuations ICNF2019, *DOI: 10.5075/epfl-ICLAB-ICNF-269248*

[3] C. Mukherjee et al., "Low-Frequency Noise in Advanced SiGe:C HBTs—Part I: Analysis", IEEE Transactions on Electron Devices, vol. 63, n° 9, pp. 3649 - 3656, 2016, *DOI: 10.1109/TED.2016.2589159*

Simple derivation of Hooge-like dependence on the number of carriers for number-fluctuation noise

A. Barsotti, M. Macucci, P. Marconcini

Dipartimento di Ingegneria dell'Informazione, Università di Pisa, 56122 Pisa, Italy

e-mail massimo@mercurio.iet.unipi.it

Abstract: Many different analyses of the dependence of the power spectral density of flicker noise on the number of carriers can be found in the literature. In particular, there are many papers describing the proportionality to the reciprocal of the square of the carrier number as a characteristic signature of number fluctuation. Here, instead, we show, for a simple case related to a bulk conductor, that a dependence on the reciprocal of the carrier number can be obtained, as in Hooge's formula.
Keywords: number fluctuations, flicker noise, Hooge's formula

Introduction: In the everlasting discussion about the origin of $1/f$ noise, one of the most debated subjects and unsolved issues is whether it is the result of mobility fluctuations or carrier number fluctuations. In many experiments, the power spectral density of flicker noise is observed to be inversely proportional to the carrier number N. From this observation, Hooge [1,2] derived his well-known empirical expression, which is often associated with mobility fluctuations. An alternative explanation for $1/f$ noise in many situations is based on carrier number fluctuations, and involves the superposition of Lorentzian generation-recombination spectra: it is usually associated with an inverse proportionality of the power spectral density to the square of the carrier number. This is the reason why, in several experimental papers, the quantity $Z = S_I N f/I^2$ or $Z' = S_I N^2 f/I^2$(where S_I is the noise current power spectral density, f is the frequency, and I is the average current through the device) is plotted vs. the number of carriers N (see Fig.1). Depending on whether the Hooge formula ($S_I = \alpha_H I^2/(fN)$, α_H being the Hooge constant) or a relationship with an inverse quadratic dependence on N ($S_I = \gamma I^2/(fN^2)$, with γ a constant) holds, a somewhat constant behavior is expected for Z (Fig. 1(a)) or for Z' (Fig. 1(b)). A similar approach is presented in Ref. 3, where the quantity $1/A$ (with $A = S_I f/I^2$) is shown, concluding that its linear increase (and therefore agreement with Hooge's formula) implies an origin of the noise connected with mobility fluctuations. Different conclusions about the dependence of the noise power spectral density on carrier number can be found in the literature, as in Ref. 4, where it is considered to be, in the case of mobility fluctuations, independent of the carrier number.
Here we report a simple calculation showing that, in the case of a bulk semiconductor with low trap occupancy, carrier number fluctuation can lead to an inverse proportionality to the total carrier number.

Results
Generation-recombination noise due to trapping and detrapping of charges leads to Lorentzian contributions, characterized by the specific time constant τ_j of the considered trap:

$$S_{I_j} = 4 n_T \Omega f_T (1 - f_T) \frac{\tau_j}{1 + (\tau_j \omega)^2} \frac{I^2}{N^2}, \tag{1}$$

where n_T is the trap concentration, Ω the volume where the traps are located (which, for a bulk semiconductor with uniform concentration of traps, coincides with the conductor volume), f_T the trap occupancy, ω the angular frequency, I the average current, and N the average carrier number. If f_T is small because the trap energy E_T is well above the Fermi level, $f_T \simeq \exp[-(E_T - E_f)/(kT)]$. The semiclassical carrier density n is given by $n = N_C \exp[-(E_C - E_f)/(kT)]$, where N_C is the effective density of states and E_C is the energy of the conduction band. Analogously, $1 - f_T \simeq 1$. Thus, we can write Eq.(1) as:

$$S_{I_j} = 4 n_T \Omega \exp\left[-\frac{E_T - E_f}{kT}\right] \frac{\exp\left[\frac{E_C - E_f}{kT}\right]}{N_C} \frac{\tau_j}{1 + (\tau_j \omega)^2} \frac{I^2}{n \Omega^2} . \tag{2}$$

If we define $\beta = (4 n_T / N_C) \exp[-(E_T - E_C)/(kT)]$, we obtain

$$S_{I_j} = \beta \frac{\tau_j}{1 + (\tau_j \omega)^2} \frac{I^2}{N} . \tag{3}$$

If we then consider the time constants of traps distributed as $1/\tau_j$ (as in the case of thermal activation [5,6]) and we integrate over the time constants of the traps, we obtain, as long as a distribution over a large enough interval of time constants is considered,

$$S_I \propto \frac{1}{\omega} \beta \frac{I^2}{N} , \tag{4}$$

and therefore a $1/f$ power spectral density inversely proportional to the total number of carriers.

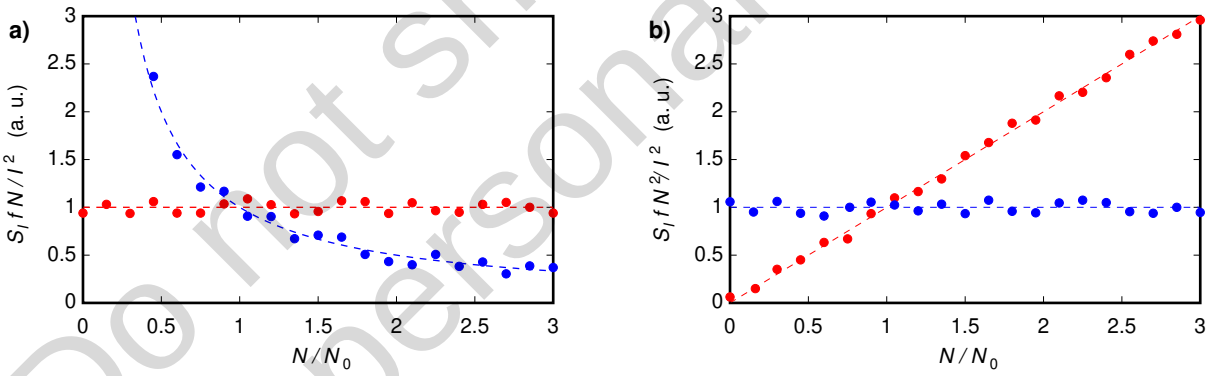

Figure 1: Plot of Z (a) and of Z' (b) vs. N/N_0, N_0 being a normalization constant. The red behavior is expected if $S_I = \alpha_H I^2/(fN)$, the blue one if $S_I = \gamma I^2/(fN^2)$.

References

1. F. N. Hooge, "$1/f$ noise is no surface effect," Phys. Lett., vol. 29 A, 1969, pp. 139-140.
2. F. N. Hooge, "$1/f$ Noise Sources," IEEE Trans. Electron Devices, vol. 41, 1994, pp. 1926-1935.
3. V. K. Sangwan, H. N. Arnold, D. Jariwala, T. J. Marks, L. J. Lauhon, M. C. Hersam, "Low-Frequency Electronic Noise in Single-Layer MoS_2 Transistors," Nano Lett., vol. 13, pp. 4351-4355.
4. A. P. Dmitriev, M. E. Levinshtein, S. L. Rumyantsev, "On the Hooge relation in semiconductors and metals," J. Appl. Phys., vol. 106, 2009, p. 024514.
5. F. K. Du Pré, "A Suggestion Regarding the Spectral Density of Flicker Noise," Phys. Rev., vol. 78, 1950, p. 615.
6. P. Dutta, P. Dimon, P. M. Horn, "Energy Scales for Noise Processes in Metals," Phys. Rev. Lett., vol. 43, 1979, pp. 646-649.

Progress status in low frequency noise AMR LSMO sensors

R. Solis Léon[1,2], L. Enger[1], S. K. Chaluvadi[3], V. Polewczyk[3], A. Y. Petrov[3], G. Vinai[3], L. Braglia[3], J. M. Diez[2], V. Pierron[1], P. Perna[2], P. Torelli[3], P. Orgiani[3], S. Flament[1], L. Méchin[1], B. Guillet[1]

[1]Université de Caen, ENSICAEN, CNRS, GREYC (UMR 6072), France
[2]IMDEA-Nanociencia, 28049 Madrid, Spain
[3]Istituto Officina dei Materiali (IOM)−CNR, Laboratorio TASC, I-34149 Trieste, Italy

bruno.guillet@unicaen.fr

Abstract: AMR sensors based on $La_xSr_{1-x}MnO_3$ thin film with different Sr composition and different shapes of the contact pads have been studied. AMR signals are improved as the Sr doping decreased while low frequency noise level increase. Optimized design could enhance the sensor performance.

Keywords: magnetoresistance, manganite, magnetic detectivity

Introduction Magnetoresistive sensors are gaining popularity due to their low cost, compact size, and enhanced performance, making them suitable for various applications such as biomedical fields, flexible electronics, position sensing, human-computer interaction, non-destructive evaluation, and navigation [1]. While giant magnetoresistance (GMR) and tunneling magnetoresistance (TMR) devices rely on resistance variations resulting from the relative magnetization directions of two distinct ferromagnetic layers, anisotropic magnetoresistance (AMR) devices exhibit electrical resistance changes based on the angle between magnetization and current density within a single layer. We previously fabricated AMR sensors using a single layer of half-metallic $La_{2/3}Sr_{1/3}MnO_3$ (LSMO) thin film, which is ferromagnetic up to 350 K and has low intrinsic noise at low frequencies. Thin films were etched in Wheatstone bridge configuration, and the magnetic easy axis was induced by using 4° vicinal $SrTiO_3$ substrates through step-induced uniaxial anisotropy, allowing for magnetotransport and noise characterization. Optimal performance were detectivity (defined as the ratio of the noise voltage spectral density by the device sensitivity) of around 1.4 $nT \cdot Hz^{-1/2}$ at 1 Hz and 240 $pT \cdot Hz^{-1/2}$ at 1 kHz at T=310 K, which corresponds to human body temperature [2].

Materials and methods The present study is focused on the impact of the Sr composition of the $La_xSr_{1-x}MnO_3$ thin film and on the shape of the contact pads in the sensor performance. The samples investigated in this study were 45 nm thick LSMO thin films grown on 4° vicinal $SrTiO_3$ (001) (STO) substrates. The strontium content varied from x=0.15 to x=0.45. Further details regarding the growth and structural analyses can be found in other publication [3]. Wheatstone bridge configurations were utilized to eliminate common mode noise and filter out colossal magnetoresistance (CMR) contributions, allowing us to retain only the AMR signal to estimate the corresponding detectivity.

Results AMR signals and low frequency noise measurements have been performed from 292 K to 330 K. The AMR signals increase with decreasing the Sr content (Fig. 1). LSMO thin films present a white noise proportional to the electrical resistivity and a 1/f noise that can be modeled via Hooge's empirical relation. The normalized Hooge parameter seems to be correlated to the Sr composition and thus to the spin magnetic moment. For low x value, the low frequency noise increase. Detectivity is thus not improved with varying the Sr composition. Different geometries of metal contact patterns and bridge arms were also studied with Optical Beam

Induced Resistance Change (OBIRCH) measurement to obtain a more homogeneous distribution of current density in the bridge arms.

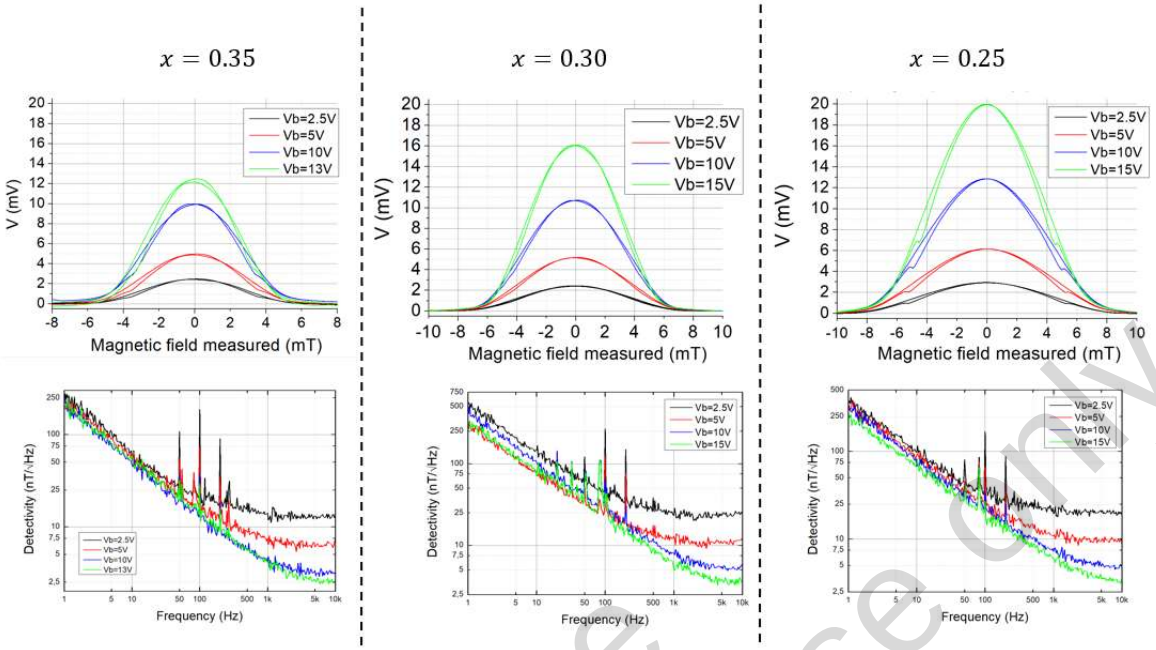

Fig. 1: Variation of the output curves of AMR sensors based on Wheatstone bridges and their associated detectivity for different applied voltages and for different Sr composition (x=0.25 to 0.35) at T=300K.

References

[1] C. Zheng et al., “Magnetoresistive Sensor Development Roadmap (Non-Recording Applications)”, IEEE Trans. Magn., 55, 4, 2019, pp. 1–30

[2] L. G. Enger et al., "Sub-nT Resolution of Single Layer Sensor Based on the AMR Effect in La2/3Sr1/3MnO3 Thin Films," IEEE Trans. Magn., 58, 2, 2022, pp. 1-4

[3] S. Chaludavi et al., “Electronic Properties of Fully Strained $La_{1-x}Sr_xMnO_3$ Thin Films Grown by Molecular Beam Epitaxy ($0.15 \leqslant x \leqslant 0.45$)”, ACS Omega, 7, 17, 2022, pp 14571-14578

Diffusion and trap-assisted tunnelling noise in low temperature reverse-biased HgCdTe diodes

M. Franco[1], N. Morisset[1,2], A. Diaz[1], C. Theodorou[1], L. Rubaldo[2], Q. Rafhay[1]

[1]Univ. Grenoble Alpes, Univ. Savoie Mont-Blanc, CNRS, Grenoble INP, CROMA, 38000 Grenoble, France
[2]LYNRED, Actipole - 364 Route de Valence, CS – 10021, 38113 Veurey-Voroize, France
email address: maeva.franco@grenoble-inp.fr

Abstract: Low temperature static current and low frequency noise measurement are carried out on a reverse-biased HgCdTe diode for infrared detection. Despite measuring a clear diffusion and trap-assisted tunneling current, a significant spectral modification is shown between the diffusion dominated regime and the TAT one. A surprising 1/f contribution is obtained for the diffusion noise, expected to feature shot noise, suggesting the influence of traps in the vicinity of the junction as the extracted activation energy match DLTS measurements.

Keywords: HgCdTe Diode, Infrared detectors, Trap Assisted Tunnelling, Diffusion Current, Low Frequency Noise

Introduction Defects in HgCdTe diodes, measured with DLTS, have been associated with flicker noise of infrared detectors [1], but no link has been obtained yet regarding their low frequency noise (LFN) characteristics at device level. In this work, LFN measurements are carried out at low temperature (200-300 K) to assess the trap activity. Using both static current measurement and LFN, transport mechanisms are identified, confirming the presence of traps, in agreement with previous DLTS results.

Sample and experimental setup The HgCdTe infrared diode measured in this work features a top n region on a bottom p region, both connected to metal layer at the top of the wafer. The diode surface is around 70000 µm². The p type region is doped by mercury vacancy and the n one by boron implantation. The device has been measured with an INSTEC probe station chamber, regulated by liquid nitrogen cycles. Measurements are made using the set up described in Fig. 1. At first, the instrumentation is characterized to assess the noise floor of the setup at several temperatures. Results demonstrate a very low noise floor, allowing the HgCdTe diode characterization (Fig. 3).

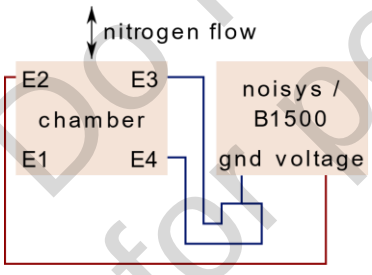

Fig. 1: Measurement setup. The E4 probe is connected to the chuck, E3 to the substrate and E2 to the diode

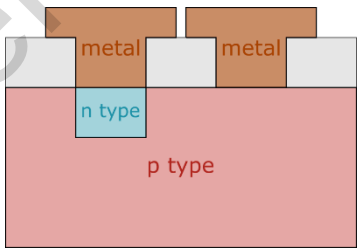

Fig. 2: Scheme of the HgCdTe diode. The gray square represent the insulator.

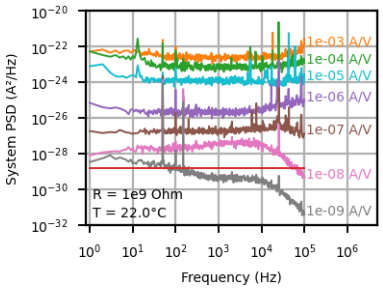

Fig. 3: Noise floor as a function of the sensitivity setup at 22°C

Static measurements IV from 293 down to 110 K are shown in Fig. 4. At 293 K, the reverse current is almost constant up to high voltages, sign of a diffusion or GR limited current. For lower T however, a larger current variation is observed, suggesting an additional transport mechanism. The current activation energy ($E_a = dln(I)/d(q/k_bT)$) shows that $E_a \sim E_g \sim 200$ mV at low voltage, tending to 0 at larger voltage. This confirms that diffusion is present at low voltage, and that trap-assisted tunnelling could explain the current increase for larger bias. Under 160 K,

current reaches a plateau and the I-V curves features an open circuit voltage in the forward regime, which denotes infrared leaks inducing a parasitic photonic current.

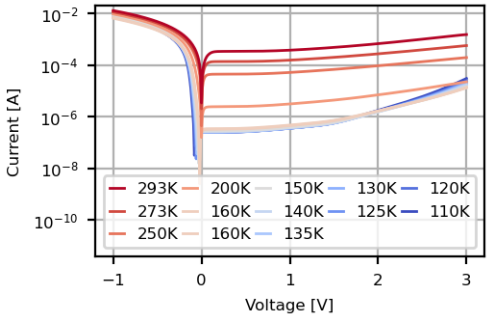

Fig. 4: Current vs voltage at several temperatures

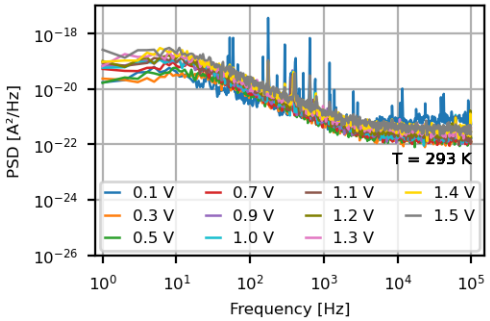

Fig. 5: Power Spectral Density (PSD) as a function of the frequency and the voltage at 293K

Noise measurements Current PSD are measured vs. frequency from 0.1 to 1.5 V, and from 293 down to 200 K, to avoid the parasitic photonic current occurring between 160 and 200 K. At 293 K, where current is diffusion limited, PSD features a clear 1/f trend, caught between two plateaus, showing small variation with bias (Fig.*5*), while a pure shot noise would have been expected. Both cut-off frequencies are shifted to lower value for decreasing temperature. At 200 K, two spectral behaviors emerge: for low voltage, PSD are almost independent of V, while 1/f noise starts to increase for higher voltage, corresponding closely to the transition from diffusion to TAT observed on the IV and in agreement with [2]. Extraction of the cut-off frequency variation with the temperature allows to deduce a trap activation energy [3] potentially associated with traps causing the 1/f contribution. The lifetime τ in Fig. 7. is extracted at low frequency and 300 mV for several temperatures. The activation energy is estimated at 146 meV with a 100% error, which partly matches complementary DLTS measurement carried out on the same device, showing traps energy at 90 meV. Finally, PSD vs. I at large frequencies confirm the presence of shot noise in the diffusion regime.

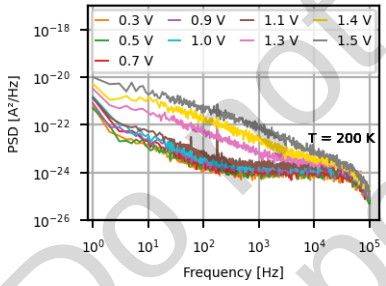

Fig. *6*: Power Spectral Density (PSD) as a function of the frequency and the voltage at 200 K

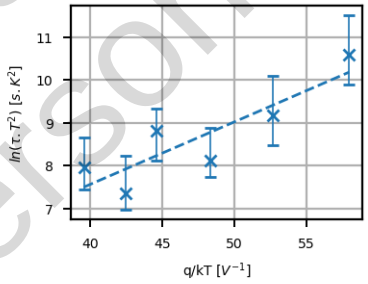

Fig. *7*: $\tau.T^2$ vs q/k_bT. The trap activation energy E_a is extracted E_a~146 meV

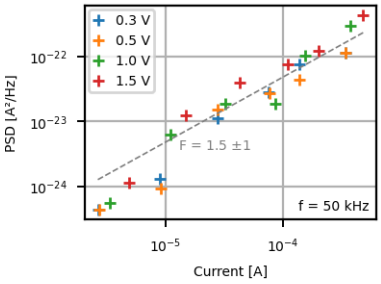

Fig. 8: PSD vs current at 50 kHz, confirming the presence of shot noise in the diffusion regime

Conclusion Low frequency noise coupled with static current measurements allow the identification of diffusion and TAT currents in an HgCdTe diode. The non-expected presence of a 1/f contribution in the diffusion noise featuring clear cut-off frequencies lead to a trap activation energy of 146 meV, in agreement with previous DLTS measurements. These experimental results open the door for improved modelling of TAT noise in diode.

Acknowledgements This work has been supported by the common lab DECID and the IPCEI Nano 2025 project DECIDED.

References [1] Guinedor, P., Brunner, A., Rubaldo, L. et al. Low-Frequency Noises and DLTS Studies in HgCdTe MWIR Photodiodes. J. Electron. Mater. 48, 6113–6117 (2019). [2] Nemirovski Y. et al, J. Vac. Sci. Technol B, 10, (1602), 1992. [3] B. Cretu et al., Semicond. Sci. Technol. 31 (2016)

Noise Analysis in Screen-Printed Carbon-Black Resistive Gauges Towards Strain Sensors

Q. Eynaud, E. Masarweh, V. Kilchytska, N. Marchal, D. Flandre, L. Van Brandt

ICTEAM Institute, UCLouvain, Louvain-la-Neuve, Belgium

Abstract: We investigate the noise performance of screen-printed carbon-black piezoresistances. The noise power spectral density of five different resistors has been measured, for seven target currents. The contributions of thermal noise and low-frequency (1/f) noise have been extracted separately. We assess the impact of the gauge resistance and supply current on the total noise power. We highlight that signal-to-noise ratios (SNR) over 100 dB can be achieved for these strain gauges in practical conditions.

Introduction Polymer Thick-Film (PTF) resistors and especially carbon-based screen-printed gauges are interesting transducer choices [1-3] for a wide range of applications, e.g. strain [1,2], thermal [2] or even gas [3] sensing, in many fields including civil engineering and flexible electronic wearables. Combining screen-printing inks to tune notable material properties is common practice [1]. Gauges studied in this work were printed with the carbon-black Micromax^{TM}7082M and the dielectric Micromax^{TM}3571 [4] polymer-based inks, resulting in high-resistivity resistors [5] as intended for strain sensing. Mechanical characteristics of a 60/40 blend of these inks show 6-8 GPa Young Modulus and low residual stresses, making it a good candidate for flexible MEMS [5]. For strain sensing, gauge factors of about 8.8 are achieved [1] but the noise characteristics of such resistors remain to be investigated. Beyond the intrinsic thermal noise, previous works reported 1/f noise [3,6,7], sometimes random telegraph noise [7].

Experimental Details Resistive bars are screen-printed using our custom blend of carbon-black-based and dielectric inks, through 200-40 Koenen steel-mesh screen on Kapton HN substrate. Next the samples are cured in an air oven at 150°C for 30 minutes. 10 nm-Cr/2 µm-Cu contact pads are subsequently thermally evaporated through a shadow mask directly on top of the printed device. Figure 1 illustrates the 1.2x0.3mm² resistive line with contacts and the resulting lengths of the five resistors. The resistive line thickness profile is measured at 4.85 ± 0.66 µm by profilometry and obtained resistances are respectively 164, 153, 397, 581 and 784 kΩ. The noise power spectral density (PSD) has been measured with an ALFNA Keysight noise analyzer as in [8]. As shown in Figure 2, seven current bias targets have been applied to each resistor, ranging from 0.5 µA to 30 µA. For all cases, the current noise PSD (S_{ir}) reveals a typical 1/f noise behavior in the low frequency range, on top of the thermal noise plateau (*4kT/R*) that is clearly dominant at higher frequency for the lowest biases.

Results and Discussion The 1/f noise is suggested to be attributed to volume/surface traps inherent to the defects in such material and manufacturing process, as in [3,6,7]. For each measurement, we fit an empirical 1/f noise model as in [8] and verify the thermal noise level *4kT/R*. Subsequently, the noise power metric σ_{ir}^2 [8] is computed according to eq. (1) in Figure 3 (a), by integrating the PSDs over [1 Hz-1 kHz]. Such frequency bandwidth is justified by the real operating conditions of the sensor. Figure 3 (a) shows that the integrated 1/f noise significantly inflates the total noise power, and that this trend is, as expected, reinforced at larger currents. One can also observe that total noise power decreases with increasing resistance value. This observation is relevant for high-resistance sensor applications. Computing the $SNR = I_r^2/\sigma_{ir}^2$ (2) points out an enhancement from 91 dB to 106 dB when increasing the current as presented in Figure 3 (b), consistently with the conventional noise/power consumption tradeoff. Finally, Figure 3 (c) depicts the trend versus the gauge resistance, confirming the potential of higher resistance devices for low-cost, flexible and noise-robust strain sensors.

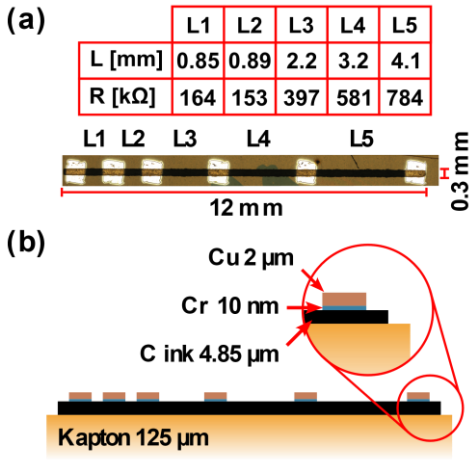

Figure 1: Printed carbon ink line with variable contact pad edge-to-edge pitch from 0.85 mm to 4.1 mm. (a) Micrograph of the studied carbon line,
(b) Schematic cross-section with materials stack.

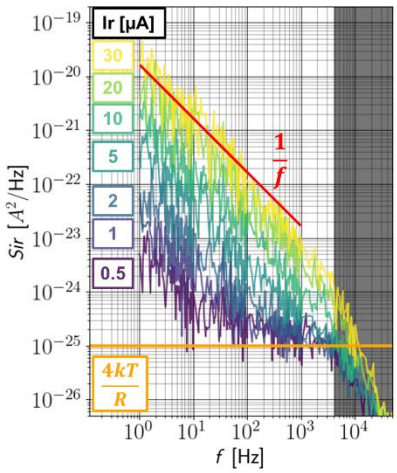

Figure 2: Current noise PSD of the 153 kΩ carbon line resistor for seven bias currents. Color lines depict the 1/f trend and the thermal noise plateau. The dark region indicates the equipment roll-off.

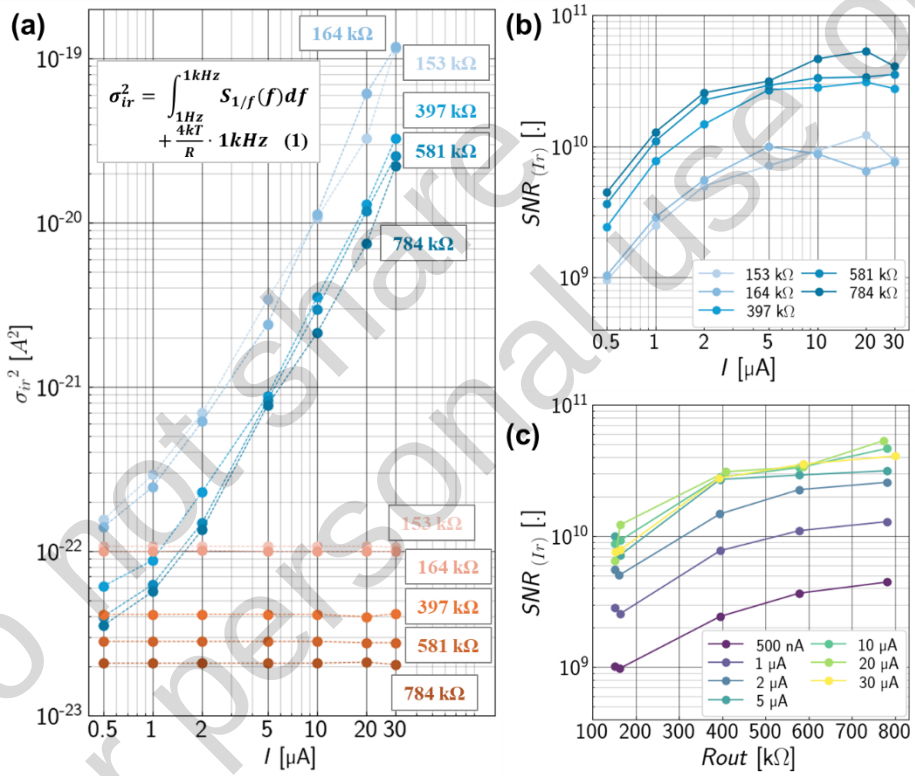

Figure 3: (a) Current noise power as a function of the target current for the five measured resistors and integrated in a practical frequency band of [1 Hz – 1 kHz]: total 1/f and thermal noise (blue) and individual thermal noise component (orange). (b) SNR vs bias and (c) SNR vs resistance values.

References

[1] N. Anderson et al., Sensors Actuators, A Phys., vol. 290, pp. 1–7, 2019
[2] C. Yuan et al., Sensors, vol. 21, no. 4, pp. 1–26, 2021
[3] K. I. Arshak et al., Thin Solid Films, vol. 495, no. 1–2, pp. 97–103, 2006
[4] E. Inks, "Micromax TM 7082M," pp. 4–7, and "MicromaxTM 3571," pp. 2024–2026, 2025.
[5] E. Masarweh et al., Appl. Res., vol. 3, no. 4, pp. 1–8, 2024
[6] A. Kolek et al., 2000 22nd Int. Conf. Microelectron. MIEL 2000 - Proc., vol. 2, pp. 531–534, 1999
[7] A. W. Stadler et al., Solder. Surf. Mt. Technol., vol. 27, no. 3, pp. 115–119, 2015
[8] L. Van Brandt et al., EUROSOI-ULIS, pp. 1-4, 2019

A current and LFN method for individually assessing layer quality in III-V multi-junctions solar cell

A. Diaz[1], C. Jouanneau[2,3], T. Bidaud[2,3], M. Darnon[4], G. Hamon[2,3], C. Theodorou[1], Q. Rafhay[1]

[1]Univ. Grenoble Alpes, Univ. Savoie Mont-Blanc, CNRS, Grenoble INP, CROMA, 38000 Grenoble, France
[2]Laboratoire Nanotechnologies Nanosystèmes (LN2)–CNRS, Université de Sherbrooke, 3000, boulevard de l'Université, Sherbrooke, Québec, J1K 0A5, Canada
[3]Institut Interdisciplinaire d'Innovation Technologique (3IT), Université de Sherbrooke, 3000, boulevard de l'Université, Sherbrooke, Québec, J1K 0A5, Canada
[4]Laboratoire Hubert Curien, Université de Lyon, UMR CNRS 5516, 42000 St Etienne, France
alexandra.diaz@grenoble-inp.fr

Keywords Low Frequency Noise, Multijunction III-V, Modelling,

Abstract Applying a Newton-Raphson algorithm, a method is developed to rebuild the full IV and PSD characteristics of a III-V multijunction solar cell, from the measurements of its separated layer, allowing the identification of defective layer and the interface dominating the low frequency noise.

Introduction Several studies [1,2,3] have demonstrated the ability of Low Frequency Noise (LFN) to analyse and identify parasitic effects leading to failures in various photovoltaics technologies, notably to determine causes of efficiency limits. Several kinds of cells have been tested, such as simple junction Si cells [4], perovskite cells [5] or III-V thin films [6]. The aim of this work is to investigate the behavior of layers that constitute III-V multijunction, which is a promising technology for concentrated solar cells, via static and LFN measurements, and assess their individual contributions and identify possible failure.

Materials and methods Static and LFN measurements have been carried out using a dedicated probe station and noise acquisition system. The III-V multijunction under study is a three layers stack of III-V materials (InGaP/InGaAs/Ge) [7]. Illustrated in Fig 1a), this device behaves as a double junction connected in series. As it features different contacts for each layer (Fig 1a), measurements of the entire stack and of each individual layer are both possible.

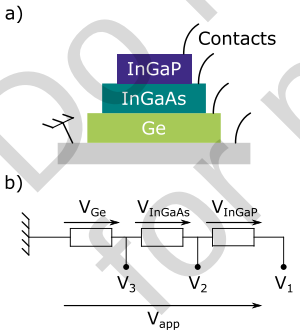

Fig 1 – (a) Design of the multijunction studied (b) Device electrical equivalent circuit

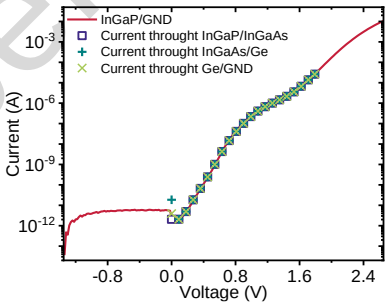

Fig 2 – IV characteristic of the entire device overlaid with current reconstruction

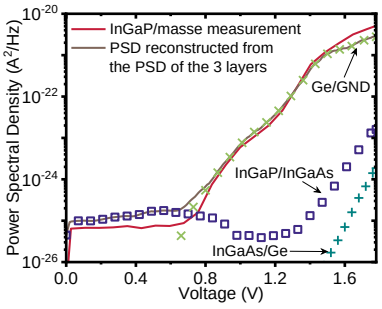

Fig 3 – PSD vs V measurement of the entire device, overlaid with layers reconstruction

IV characteristic reconstruction As each layer features a contact, reconstruction of the entire device current measurement should be possible from measurements of each pair of contacts. The multijunction is thus equivalent to 3 sub-components in series (Fig 1b), and allow to write the following system of non-linear equations:

$$\begin{cases} V_{app} = V_{Ge} + V_{InGaAs} + V_{InGaP} \\ I_{InGaP}(V_{InGaP}) = I_{InGaAs}(V_{InGaAs}) \\ I_{InGaAs}(V_{InGaAs}) = I_{Ge}(V_{Ge}) \end{cases} \quad (1)$$

To solve it, the Newton-Raphson (NR) method [8] is employed. As the continuous relations and accurate analytic models needed does not exist for each independent layer, numerical interpolations based on IV measurements and their derivative are used. The iterative resolution follows the recurrence formula $V^{k+1} = V^k - J^{-1} \cdot F(V^k)$, with:

$$V = \begin{pmatrix} V_{InGaP} = V_1 \\ V_{InGaAs} = V_2 \\ V_{Ge} = V_3 \end{pmatrix} \qquad F = \begin{pmatrix} V_1 + V_2 + V_3 - V_{app} \\ I_1(V_1) - I_2(V_2) \\ I_2(V_2) - I_3(V_3) \end{pmatrix} \qquad J = \begin{pmatrix} \frac{\partial F_1}{\partial V_1} & \frac{\partial F_1}{\partial V_2} & \frac{\partial F_1}{\partial V_3} \\ \frac{\partial F_2}{\partial V_1} & \frac{\partial F_2}{\partial V_2} & \frac{\partial F_2}{\partial V_3} \\ \frac{\partial F_3}{\partial V_1} & \frac{\partial F_3}{\partial V_2} & \frac{\partial F_3}{\partial V_3} \end{pmatrix} = \begin{pmatrix} 1 & 1 & 1 \\ \frac{\partial I_1}{\partial V_1} & -\frac{\partial I_2}{\partial V_2} & 0 \\ 0 & \frac{\partial I_2}{\partial V_2} & \frac{\partial I_3}{\partial V_3} \end{pmatrix} \quad (2)$$

The initial vector V is set to $V_i = V_{app}/3$ for i= {1,2,3}. A new vector is obtained after each iteration and the process stops when convergence is reached. The vector solution allows then to compute the current for each layer corresponding to a defined V_{app} voltage. The reconstruction obtained is illustrated in fig 2 and confirms that the current obtained from each layer and the NR method match the measurement of the total current across the whole stack.

Noise Reconstruction Since the layers are connected in series in the device (Fig 1b), the noise reconstruction should be based on the sum of the voltage PSD, and not the PSD of the current (4). Our setup however provides measurements of current PSD, therefore a transformation employing dynamic conductance is needed to write the reconstruction expression as (5):

$$S_{V_{tot}}(V_{app}) = \sum_i S_{V_i}(V_i) \quad \Rightarrow \quad \left(\frac{1}{g_{d_{tot}}}\right)^2 \cdot S_{I_{tot}}(V_{app}) = \sum_i \left(\frac{1}{g_{d_i}}\right)^2 \cdot S_{I_i}(I_i) \quad (4)$$

$$S_{I_{tot}}(V_{app}) = \sum_i \left(\frac{g_{d_{tot}}}{g_{d_i}}\right)^2 \cdot S_{I_i}(I_i) \quad \text{where} \quad g_{d_{tot}} = \frac{\partial I_{tot}}{\partial V_{app}} \quad \text{and} \quad g_{d_i} = \frac{\partial I_i}{\partial V_i} \quad (5)$$

As for the current, interpolations of measured current PSD are numerically computed to define voltage PSD. PSD reconstruction (fig 3) verifies the presented method and pinpoints a major noise contribution from top layer at low voltages and the bottom one at higher voltages.

Layer monitoring The method described above could be used as a tool to monitor the operation of the multijunction layers. IV reconstruction of an identical device reveals a mismatch on a section of the curve in fig. 4. By applying an adapted NR method and skipping the InGaAs layer from the measurement, the reconstruction finally matches the measurement (Fig 5). This hence demonstrates a defective InGaAs layer in this device and the possibility of the method to identify faulty interfaces.

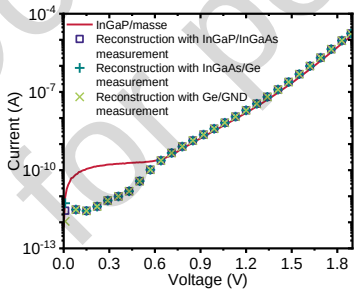

Fig 4 – IV reconstruction with InGaAs layer

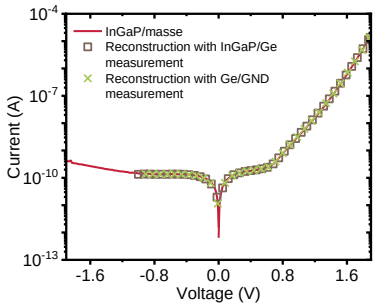

Fig 5 – IV reconstruction without InGaAs layer

References

[1] A. L. McWhorter, PhD Thesis, MIT, Cambridge, 1955.[2] T. G. M. Kleinpenning et. al, 1984, vol. 12, no 4, p. 363-370.[3] L. K. J. Vandamme et. al, Solid-State Electronics, 1983, vol. 26, no 7, p. 671-674.[4] E. Simoen et. al, Physica B: Condensed Matter, 1996, vol. 228, no 3-4, p. 219-225. [5] C. Barone et. al, Scientific Reports, 2016, vol. 6, no 1, p. 34675. [6] L. Skvarenina et al, ICNF 2017, 2017. p. 1-4. [7] T. Bidaud *et al.* Energies 2024, 17(11), 2538 [8] W.H. Press. *Numerical recipes 3rd edition: The art of scientific computing*. Cambridge univ. press, 2007.

Assessing contact quality of Si p-n diodes through series resistance noise characterization

A. Diaz[1], C. Wulles[1], M. Franco[1], A. Albouy[2], P. Leduc[2], C. Theodorou[1], Q. Rafhay[1]

[1]Univ. Grenoble Alpes, Univ. Savoie Mont-Blanc, CNRS, Grenoble INP, CROMA, 38000 Grenoble, France
[2]CEA Leti, Univ. Grenoble Alpes, 38000 Grenoble, France
alexandra.diaz@grenoble-inp.fr

Keywords: Low Frequency Noise, PN Junction, Series resistance, Modelling

Abstract: Using LFN measurement on Si p-n diodes, series resistances are shown to contribute to noise at large currents values. With adequate modelling, quantitative estimation of the contact quality is obtained, which could be employed as a tool for device reliability and process assessment.

Introduction The study of Low-Frequency Noise (LFN) [1,2] allows to identify parasitic effects and sources of degradation in semiconductor devices, such as the p-n diodes [3]. For the latter, a lack of consensus on the noise modelling leads to a poor understanding of defects, aging mechanisms and parasitic effects in diodes, such as series resistance [4], which could disrupt the measurement quality. The aim of this work is to model the total noise for Si diodes with a simple MESA architecture, with a focus on series resistance noise, in order to reach a proper understanding of its behavior, and examine its potential relation to fabrication quality.

Experimental setup and devices LFN measurements have been carried out using a dedicated isolated probe station and noise acquisition system. To properly study the noise induced by the series resistance and assess the influence of the contact, two p-n Si diodes were chosen. The first (diode A) has a top-bottom contact configuration while the second (diode B), features all contacts on the top side, with t_{Si} =70 nm and t_{BOX} =145 nm (Fig. 1).

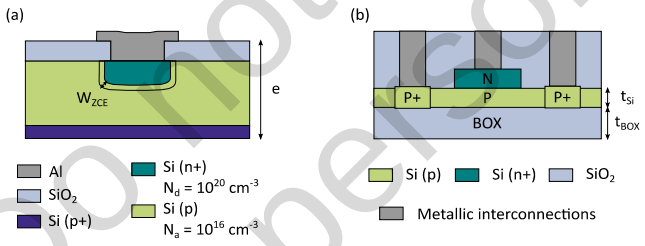

Fig 1 - Cross-sectional view of diodes: (a) diode A with rear contact on the back of the wafer, (b) SOI diode B with all contacts on front side structure

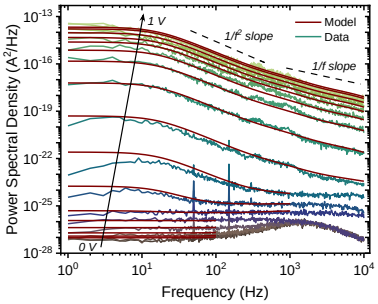

Fig 2 – PSD vs frequency for the diode A measured: comparison between data measured and model

Experimental Results and Modelling The static measurements for Diode (A) follow the double diode model [6], which is used to extract the ideality factors and the access resistance. The PSD are plotted as function of the frequency in Fig. 2, for forward voltages ranging from 0 to 1V. For low voltages, the system noise dominates, whereas for intermediate voltages a shot noise is observed, and a clear Lorentzian-like noise at higher voltages followed by 1/f spectra at high frequencies. Plotting the PSD vs I (Fig. 4) reveals that the shot noise regime is indeed linear with I, with a Fano factor of 0.66, suggesting SRH noise [6,7]. For larger values of current (>10^{-5} A), the PSD becomes proportional to I^3, which is unusual but already observed in GaN diodes and attributed to series resistance noise [4]. To model the total current noise, all three contributions are accounted for:

$$S_I^{tot} = S_{syst} + S_{shot} + S_{I_{Rs}} = S_{syst} + 2qFI + \left(\frac{\partial I}{\partial R_S}\right)^2 S_{R_s} \quad (1)$$

By using a simplified current model including an ideal diode and a series resistance, the R_s contribution to the noise can be demonstrated as follows:

$$\frac{\partial I}{\partial R_s} = \frac{\partial}{\partial R_s}\left(I_{S1} exp\left(\frac{q(V - IR_s)}{n_1 k_B T}\right)\right) \quad \Rightarrow\ldots\Rightarrow \quad S_{I_{Rs}} = \frac{I^4}{\left(\frac{n_1 k_B T}{q} + R_s I\right)^2} S_{R_s} = C(I) \times S_{R_s} \quad (2)$$

where I_{S1} is the diode saturation current with ideality factor n_1 and R_s the series resistance. The Lorentzian shape of PSD when S_{IRs} is predominant allows S_{Rs} to be fitted according to:

$$S_{R_s} = (\overline{\Delta R_s})^2 \frac{4\tau}{(1 + 2\pi f\tau)^2} \quad (3)$$

where $<\Delta R_s>^2$ the series resistance variance and τ the traps' time constant. Using (1)-(3), an excellent agreement between the model and the measurement is obtained (Fig. 4). In order to examine a potential correlation between diode parameters (R_s, n_1, I_{s1}, doping, thickness) and $<\Delta R_s>^2$ and τ, the latter were extracted, but no correlation was found, indicating a link between Lorentzian spectra and contact quality, rather than an intrinsic device parameter.

To verify the hypothesis, devices were pasted with silver lacquer on a conductive Cu plate with an insulated bottom rear face. An almost 8 times lower R_s is observed on the I-V characteristics (Fig. 3), which is confirmed by the much lower PSD, as well as a resulting pure 1/f shape. Furthermore, after pasting, PSD shows a $\sim I^2$ evolution instead of $\sim I^{3.8}$, implying a S_{IRs} suppression after pasting. Trying to fit by only dividing R_s by 8 times actually fails (Fig. 4), meaning that the noise reduction is not only due to the decrease in R_s, but also to a significant decrease of S_{Rs}, in turn revealing a connection between surface defects and R_s. Fitting the 1/f PSD obtained after pasting with the same procedure do not show the right current dependancy, suggesting that the noise is not induced anymore by series resistance.

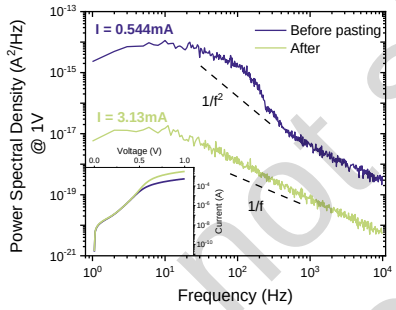

Fig 3 – PSD vs frequency for the diode A: comparison between measurements for wafer pasted and not with IV characteristics inset

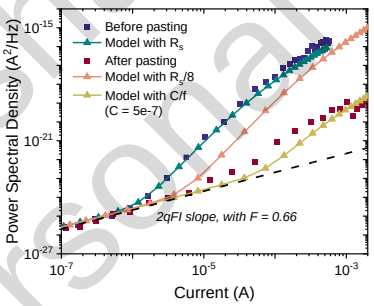

Fig 4 – PSD vs current for diode (A): comparison of model and data for different contact

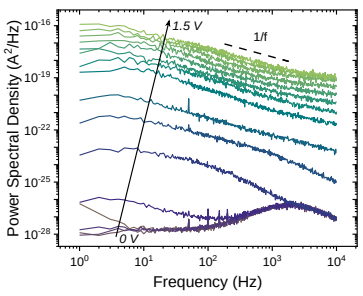

Fig 5 – PSD vs frequency for diode (B)

Results obtained for Diode (B) (more advanced architecture) (Fig. 5), confirmed the presence Lorentzian spectra related to series resistance noise, further demonstrating the potential use of the latter as an indicator of fabrication process quality.

Acknowlegment This work has been supported by the French National Research Agency through the ANR Brightside ANR-22-CE05-0027.

References

[1] T. G. M. Kleinpenning et. al, Solar Cells, 1984, vol. 12, no 4, p. 363-370.
[2] L. K. J. Vandamme et. al, Solid-State Electronics, 1983, vol. 26, no 7, p. 671-674.
[3] C. Wulles, Solar Energy Materials and Solar Cells, 2023, vol. 256, p. 112344.
[4] S. Bychikhin, et. al, Journal of Applied Physics, 2005, vol. 97, no 12.
[5] A. Kaminski et al., Conference Record of the Twenty Sixth IEEE PVSEC, 1997. p. 203-206.
[6] P. Lauritzen, IEEE TED, 1968, vol. 15, no 10, p. 770-776.
[7] K. Van Vliet, IEEE TED, 976, vol. 23, no 11, p. 1236-1246.

Impact of 1/f Noise in Scaled FeFET Devices on Hardware Neuromorphic System Performance

Ryun-Han Koo[1], Jong-Ho Lee[1], Wonjun Shin[2*]

[1]Department of Electrical and Computer Engineering and Inter-University Semiconductor Research Center (ISRC), Seoul National University, Seoul 08826, Korea (koo9797@snu.ac.kr)

[2]Department of Semiconductor Convergence Engineering, Sungkyunkwan University, Suwon 16419, Republic of Korea (swj0107@snu.ac.kr)

Abstract: We demonstrate 1/*f* noise in scaled TiN-HZO-SiO_2-Si FeFETs, dominated by carrier number fluctuation. Downscaling intensifies read noise and degrades neuromorphic accuracy (VGG-11 on CIFAR-10) by up to 3% below 100 nm.

Keywords: 1/*f* noise, FeFET, Neuromorphic

Introduction There is growing interest in hardware neuromorphic systems for efficient, parallelizable computing in artificial intelligence and machine learning. Ferroelectric field-effect transistors (FeFETs) have emerged as promising candidates due to their nonvolatile behavior, ease of CMOS integration, and low operation voltage [1]. However, as these devices are aggressively scaled to achieve high-density integration and faster processing, 1/*f* noise—especially that governed by carrier number fluctuation (CNF)—becomes increasingly significant [2]. This noise can degrade the accuracy of current-based vector-matrix multiplication (VMM) operations in neuromorphic networks. In this work, we investigate the 1/f noise characteristics of TiN-HZO-SiO_2-Si FeFETs, analyze their impact on a VGG-11 network trained on CIFAR-10, and discuss how CNF-induced noise poses challenges for FeFETs with channel lengths below 100 nm.

Results and Discussion FeFETs with a TiN-HZO (6 nm)-SiO_2 (1.2 nm)-Si stack were fabricated. Figure 1a shows a memory window of around 1 V, attributed to ferroelectric switching [1]. As seen in Figure 1b and 1c, the normalized power spectral density (S_{ID}/I_D^2) exhibits a 1/*f* dependence, and its behavior matches $(g_m/I_D)^2$, indicative of CNF as the dominant noise mechanism. Since S_{ID}/I_D^2 is proportional to $(g_m/I_D)^2$ and inversely proportional to W and L [2], smaller devices show higher noise levels, challenging compact hardware neuromorphic implementations. In Figure 1d and 1e, measurements confirm that S_{ID}/I_D^2 increases as the device area decreases, following the inverse proportionality predicted by the CNF model (Figure 1f). This rise in noise was then linked to performance degradation in a hardware neuromorphic system. Figure 2a demonstrates the long-term potentiation (LTP) and depression (LTD) characteristics of the FeFET, showing potential for neuromorphic applications. A VGG-11 network (Figure 2b) trained on CIFAR-10 was used to test how read noise affects learning accuracy. As shown in Figure 2c and 2d, increasing read noise (0 to 1.0) slows down learning and lowers final accuracy. Further analysis examined the effect of area scaling on noise. Extrapolations of S_{ID}/I_D^2 for FeFETs at lengths of 10, 1, 0.1 (100 nm), and 0.01 um (10 nm) yielded read noise sigma values of 6.3×10^{-3}, 1.8×10^{-2}, 5.6×10^{-2}, and 0.17, respectively. Simulations in Figure 2e show negligible accuracy loss above 1 um, but around 3% loss at 10 nm—highlighting the adverse impact of device noise at sub-100 nm dimensions.

Conclusion Below 100 nm, inherent CNF-induced noise in FeFETs significantly affects analog operations in hardware neuromorphic systems. These findings underscore the need for careful noise mitigation strategies in FeFET device and circuit designs to sustain high performance in next-generation neuromorphic accelerators.

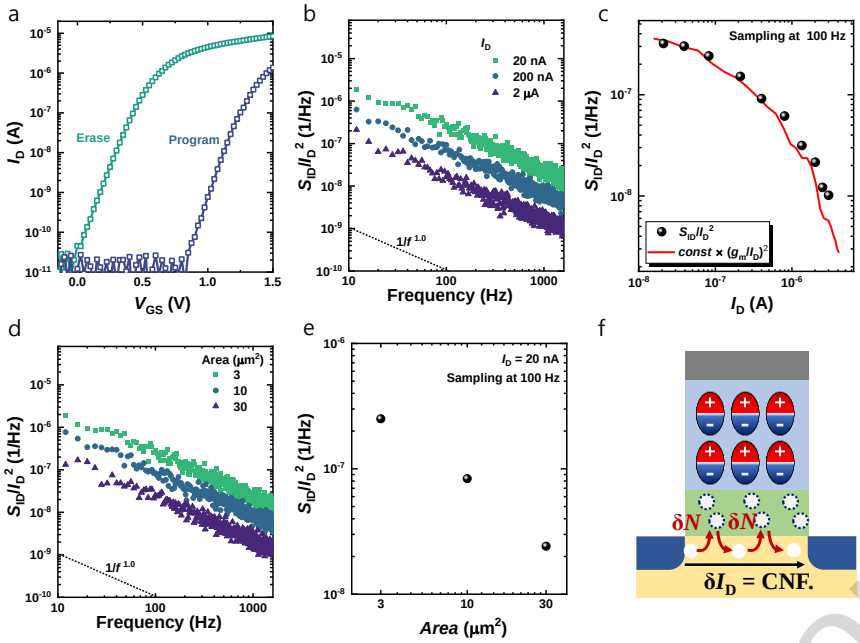

Fig. 1 (a) I_D–V_{GS} curves of the FeFET. (b) S_{ID}/I_D^2 under different drain currents. (c) S_{ID}/I_D^2 versus I_D. (d) S_{ID}/I_D^2 at identical V_{GS} for FeFETs of varying area. (e) S_{ID}/I_D^2 versus area, sampled at 100 Hz. (f) Schematic diagram illustrating the CNF-based origin of 1/*f* noise in FeFETs.

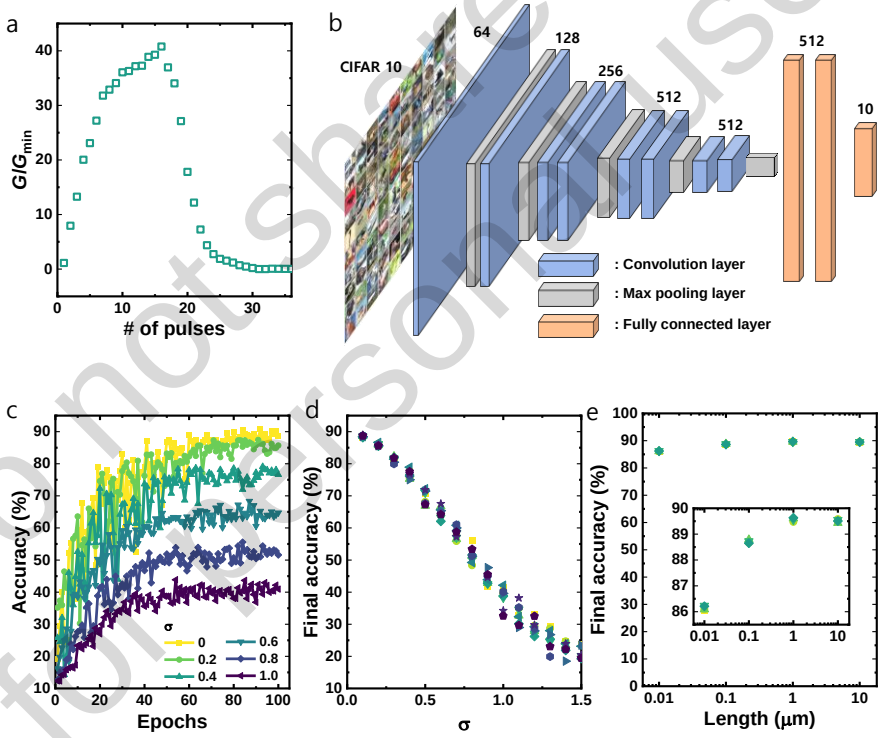

Fig. 2 (a) LTP and LTD characteristics in FeFET. (b) Schematic of the VGG-11 network trained on the CIFAR-10 dataset. (c) Test accuracy versus training epoch under different read noise levels (0 to 1.0). (d) Final accuracy (after 100 epochs) across ten trials for various noise levels. (e) Accuracy under different device scaling levels

References

[1] H. Mulaosmanovic et al., "Ferroelectric field-effect transistors based on HfO2: a review", Nanotechnology, vol. 32, no. 50, 2021, p. 502002.

[2] L. K. Vandamme et al., "1/f noise in MOS devices, mobility or number fluctuations?", IEEE Transactions on Electron Devices, vol. 41, no. 11, 1994, pp. 1936–1945.

On the instrumentation for current noise measurements in low impedance devices

G. Scandurra, E. Cardillo, L. Ferro, G. Giusi, C. Ciofi

Department of Engineering, University of Messina, Messina, Italy
gscandurra@unime.it

Abstract: Transimpedance amplifiers for current noise measurements are almost exclusively obtained starting from a high gain voltage amplifier in a shunt-shunt feedback configuration. As current noise measurements are typically performed on high impedance devices, FET input operational amplifiers are typically used in their design. However, if cross-correlation is employed, the contribution from the equivalent input current noise of the operational amplifiers is, in principle, eliminated and it is the equivalent input voltage noise that sets the limit to the background noise. Therefore, especially for moderate and low impedances, lower background noise can be obtained by resorting to BJT input operational amplifiers, at the cost of extended measurement time. In this paper we address this specific issue in an attempt to provide design guidelines for the design of cross-correlation configurations for current noise measurements when the device under test is characterized by relatively low impedance.

Keywords: Instrumentation; Transimpedance amplifiers, Cross correlation.

Introduction Most primary sources of noise in electron devices are described in terms of equivalent current sources[1], and therefore the preferred measurement configuration should be the one that allows to bias the DUT with a voltage source while a transimpedance amplifier is used to amplify the current noise, i.e. to employ a current noise measurement configuration. However, for DUTs characterized by medium to low impedances Z_D (with $|Z_D|$ below a few tens of kΩ), voltage noise measurements are more easily performed and current noise measurements are generally used only in the case of high or very high impedances [2]. In principle, if we can accurately measure the impedance of the DUT, we can obtain the current noise from the knowledge of the voltage noise and vice-versa, but the characterization of the impedance of the DUT can be difficult, prone to error and time consuming. Therefore, finding ways to perform direct current noise measurements on devices with low impedance is a relevant task even if it implies some additional cost in terms of instrumentation and measurement time.

Cross correlation current noise measurements In a cross correlation current noise measurement configuration (Fig. 1), the DUT bias is set to V_B by the virtual short between the inputs of O_{A1} and O_{A2}[3]. The discussion on the dimensioning of the feedback resistances R_{R1} and R_{R2} (with R_{R1}=R_{R2}=R_R) due to DC bias and bandwidth limitation will be included in the full paper. By following a quite standard procedure and assuming (since we deal with moderate to low DUT impedances) that we can make R_R>> $|Z_D|$ (so that $R_R||\ Z_D \approx Z_D$) we have, for the PSD S_{vo11} at the output of the first channel and for the cross correlation S_{vo12} between the two outputs:

$$S_{vO11} = R_R^2\left(S_{iD} + S_{in} + \frac{4kT}{R_R} + 2\frac{S_{en}}{|Z_D|^2}\right) \quad ; \quad |S_{vO12}| = R_R^2\left(S_{iD} + 2\frac{S_{en}}{|Z_D|^2}\right) \qquad (1)$$

where S_{iD} and S_{in} are the *PSD* of the sources i_D and $i_{n1,2}$ in Fig1, k is the Boltzmann constant, T the absolute temperature and *Sen* is the PSD of the equivalent voltage noise sources $v_{en1,2}$ in Fig. 1. Eq. 1 clearly confirms that the background noise that can be achieved depends on the equivalent input voltage noise of the operational amplifiers. What Eq. 1 does not tell, however, is the measurement time that is required to bring the uncorrelated noise below the correlated one. In the numerical process used for cross spectra estimation, the uncorrelated noise decreases with the square root of the number M of adjacent records being elaborated and averaged [4]. When using DFT spectrum analyzers, the duration of each single record is the inverse of the

resolution bandwidth RBW, so that, given a total measurement time T_M, we have $M=RBW\ T_M$. Indeed, in a sense, we can think of the estimated cross spectrum S_{voe} (T_M) obtained from actual measurements after a sufficient long time T_M as representative of the quantity:

$$|S_{voe}(T_M)| = R_R^2\left[S_{iD} + 2\frac{S_{en}}{|Z_D|^2} + \frac{1}{\sqrt{RBW\ T_M}}\left(S_{in} + \frac{4kT}{R_R}\right)\right];\ |S_{voe}(T_M \to \infty)| = |S_{vO12}| \quad (2)$$

Eq. 2 can be used to estimate the feasibility of current noise measurement for given measurement conditions and can be used as a guide in the selection of the proper operational amplifiers. Suppose we want to measure the thermal current noise of a resistor $Z_D=R_D=10$ kΩ at room temperature ($S_{iD}=1.66\times10^{-24}$ A^2/Hz). With $R_R=1$ MΩ we obtain a negligible contribution from R_R. Suppose we have the LT1793 (JFET input) and the OP27 (BJT input) OA available. At 100 Hz, the overall contribution of the LT1793 and the OP27 to So_{11} are almost the same. However, while in the case of the LT1793 this contribution comes mostly from S_{en}, in the case of the OP27 the contribution comes mostly from S_{in}. Indeed, from Eq. 2 we can estimate that with RBW=100 Hz, the DUT noise becomes predominant after a few seconds. The method can be effective down to a fraction of 1 Hz, provided that one is willing to wait significantly longer times. The data in Fig. 2 have been obtained with an average time of 1 hour with different RBWs, depending on the frequency range.

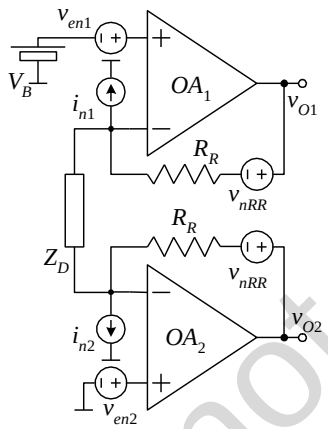

Fig. 1 Configuration for cross-correlation current noise measurements.

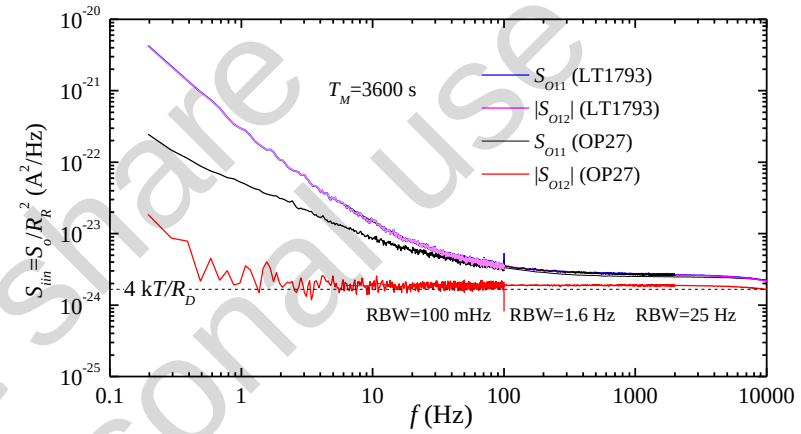

Fig.2: Results from Fig. 1 with $Z_D=R_D=10$ kΩ. Better performances are obtained using a BJT input operational amplifier since cross-correlation cancels out the effect of the OA current noise sources.

References

[1] A. Van der Ziel, "Noise in Solid State Devices and Circuits," John Wiley & Sons, Inc., New York, 1986.
[2] G. Scandurra et al., "A review of design approaches for the implementation of low-frequency noise measurement systems", Rev. Sci. Instrum. 1 November 2022; 93 (11): 111101.
[3] G. Ferrari, M. Sampietro; "Correlation spectrum analyzer for direct measurement of device current noise", Rev. Sci. Instrum. 1 July 2002; 73 (7): 2717–2723.
[4] E. Rubiola, "The magic of cross-spectrum measurement from DC to optics, Proc. 22 Euro-pean Frequency and Time Forum (EFTF)", art. no.186, Toulouse, France, 23-25 April 2008.

BJT-Input transimpedance amplifier for current noise measurements in low impedance devices.

K. Achtenberg[1], C. Ciofi[2], G. Scandurra[2]

[1]Institute of Optoelectronics, Military University of Technology, Warsaw, Poland, krzysztof.achtenberg@wat.edu.pl
[2]Department of Engineering, University of Messina, Messina, Italy, carmine.ciofi@unime.it, graziella.scandurra@unime.it

Abstract: We propose the design of an ultra-low noise, discrete BJT input based operational amplifier as the main building block for a transimpedance amplifier intended for current noise measurements in low impedance devices (impedance below 1 kΩ). Indeed, when dealing with low impedance devices, a very low level of equivalent input voltage noise for the operational amplifier may result in a lower contribution to the overall background noise, even in the presence of a large equivalent input noise. Preliminary measurements on a prototype that has been built and tested demonstrate that the approach we propose can current noise measurements in a wide range of bias in advanced low impedance photodetectors.

Keywords: transimpedance amplifier, noise, infrared detector

Introduction Current noise measurements are performed almost exclusively by resorting to a TransImpedance Amplifier (TIA) based on a low-noise Operational Amplifier (OA) in a shunt-shunt feedback configuration. When dealing with high impedance devices, the background noise, at least at low frequencies, is set by the thermal noise of the feedback resistance (often in the range of tens of MΩ or more [1]), provided that the Equivalent Input Current Noise (EICN) is sufficiently low. In these cases, we resort to FET input operational amplifiers to minimize the EICN, even at the cost of large values of Equivalent Input Voltage Noise (EIVN), since the noise introduced by the feedback resistance remains dominant. However, when the DUT impedance decreases, the weight of the EIVN increases and it may become convenient to minimize the EIVN even at the cost of increasing S_{in}. This can be understood with reference to the circuit in Fig. 1 and the corresponding expression for the equivalent input noise given by:

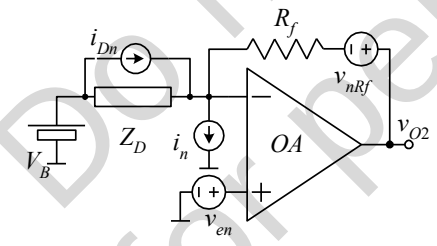

Fig. 1: Transimpedance amplifier for current noise measurements.

$$S_{ieq} = S_{id} + S_{in} + \frac{S_{en}}{|R_f//Z_D|^2} + \frac{4kT}{R_f} \qquad (1)$$

where S_{id} is the PSD of the current noise introduced by the DUT, S_{in} and S_{en} are the PSD of the EICN and EIVN of the OA, k is the Boltzmann constant and T the absolute temperature. What may not be immediately obvious from Eq. 1 is the fact that, as the DUT impedance decreases, the current noise level associated to its resistance also increases. In other works, we expect to measure larger level of current noise from lower DUT impedances, so that we may tolerate larger levels of S_{in}. On the other hand, the effect of S_{en} is inversely proportional to the DUT impedance squared (typically we have $|Z_f| << R_f$ in all cases), so that as $|Z_D|$ decreases, Sen rapidly becomes the dominant term in Eq. 1. For very low input impedances, it may become convenient to resort to OAs characterized by very low EIVN even if this comes at the cost at a very high level of EICN. Indeed, in this work we explored the possibility of realizing a TIA around a OA characterized by an extremely low level of voltage noise, obtained by resorting to a discrete BJT input stage. Clearly, a discrete BJT input stage results in a relatively large level of EICN, larger than what is normally found in

many integrated low-noise BJT input operational amplifiers. However, with impedances well below 1 kΩ, and thanks to the excellent EIVN, we obtain a background noise level that is sufficient to perform sensible noise measurements in a range of different bias for the investigated devices.

Results The schematic of the TIA we have built and tested is reported in Fig. 2. When testing the amplifier using low impedances (resistances) as DUTs (Fig. 3), it is apparent that the measured noise is much closer to the expected noise with respect to the case of a low-noise solid monolithic OA such as the LT1028. This is especially true at very low frequencies, that is the most interesting frequency range for the investigation of the $1/f$ noise produced by the devices under test. Current noise measurements on an actual device (uncooled HgCdTe long-wave infrared detector [2]) are reported in Fig. 4. The resistance of the DUT in all operating conditions is below 100 Ω. The noise generated by the DUT is well above the background noise in a large bias interval.

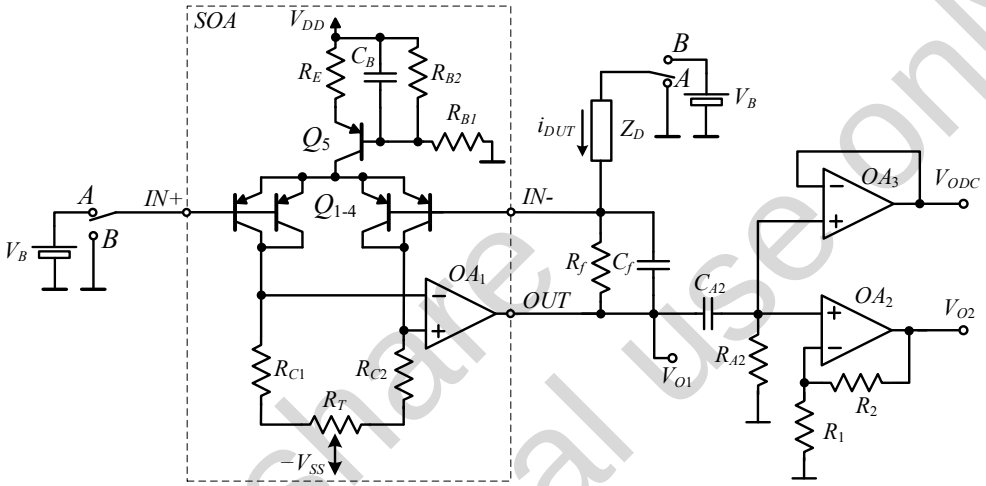

Fig. 2: Schematic of the proposed transimpedance amplifier.

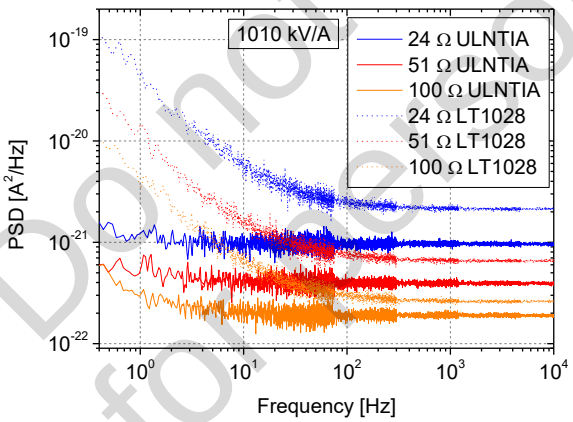

Fig. 3: Equivalent input noise using unbiased resistances as DUT.

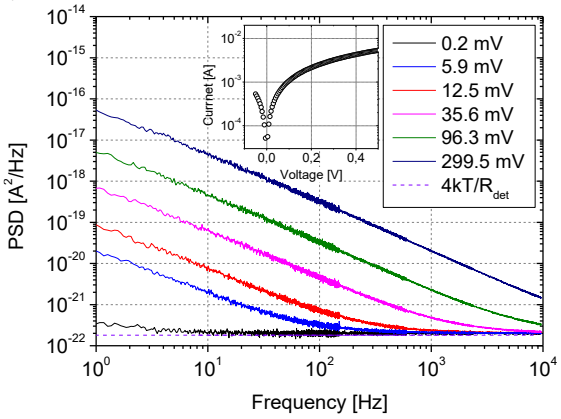

Fig. 4: Equivalent input noise on an actual HgCdTe detector at 300 K. The I-V characteristic of the device is reported in the inset

References

[1] M. Carminati, G. Ferrari, M. Sampietro, A. P. Ivanov, and T. Albrecht, "Low-noise dual-channel current amplifier for DNA sensing with solid-state nanopores," in 2012 19th IEEE International Conference on Electronics, Circuits, and Systems (ICECS 2012), IEEE, Dec. 2012, pp. 817–820.

[2] J. Piotrowski, "Uncooled operation of IR photodetectors," in Opto-Electronics Review, 2004. 12(1), pp. 111–122

Analysis of the effect of phase noise in the reference oscillator of a qubit control system

A. Barsotti, P. Marconcini, G. Procissi, M. Macucci

Dipartimento di Ingegneria dell'Informazione, Università di Pisa, 56122 Pisa, Italy

e-mail massimo@mercurio.iet.unipi.it

Abstract: The control of superconducting qubit states and the implementation of essential quantum computer operations, defined quantum gates, are achieved through the application of precise radio frequency (RF) pulses, inevitably affected by phase noise. This phenomenon can cause unintended rotations of the qubit state on the Bloch sphere and induces dephasing. However, the effect of phase noise in control operations has not yet been extensively studied. In this work, we propose a mathematical method for generating a phase noise model to perform simulations with phase-noise-affected control signals.
Keywords: superconducting qubit, phase noise, control

Introduction: A major non-ideality in the generation of control and readout signals for superconducting qubits is phase noise: it results in the spreading of signal energy into side-bands around the center frequency. The level of phase noise is a fundamental quality parameter for any signal-generating circuit, and its containment is critical for the proper operation of control systems for superconducting qubits.
In order to more precisely understand the effect of phase noise on the achievable fidelity of quantum gates, numerical simulations of the time evolution of a qubit state in the presence of noise are performed. We develop a numerical procedure to generate sequences of baseband phase noise values with an arbitrarily shaped power spectral density. This procedure, illustrated in Fig.1, starts with the generation of a sequence of pseudorandom noise values characterized by a gaussian amplitude distribution and a white spectrum. The process involves synthesizing the response of a finite impulse response filter, defined by the desired frequency behavior. The white Gaussian noise sequence is then convolved with this impulse response to obtain the desired phase noise sequence. To accelerate the computation of the convolution, the method leverages the fast Fourier transform to convert the operation into a multiplication in the frequency domain, performing proper zero-padding to ensure vector lengths are powers of 2.
Initial tests using this model with rectangular pulses affected by $1/f$ phase noise show a significant loss of fidelity over a series of pulses, highlighting the importance of low phase noise levels for maintaining high fidelity.

Results
The power spectral densities for flicker-like phase noise at different corner frequencies, obtained by means of the numerical method explained in the previous paragraph, are shown in Fig. 2(a). Starting from the phase noise values achieved with this procedure, we studied the contribution of different spectral noise components in Qiskit-Dynamics simulations. These simulations allow us to study the time evolution of the state of the qubit, initially set to the ground state $|0\rangle$. Rectangular control pulses, implementing NOT gates, are initially tuned for the ideal scenario to achieve near-perfect fidelity in the absence of noise. Finally, the generated phase noise values are

applied to the control pulses, affecting the real and imaginary components of the pulse envelopes. The fidelity of the resulting states is then evaluated to quantify the impact of phase noise on quantum operation. From the results shown in Fig.2(b), we conclude that a well-defined spectral range provides the main contribution to the fidelity degradation, depending on the duration of the experiment and the coupling with the qubit. This contrasts with conclusions by Ball et al. [1], based on expressions derived from Green et al. [2], where they conclude that higher-frequency components of phase noise make the largest contribution.

References

1. H. Ball et al, npj Quantum Information **2**, 16033, (2016), doi:10.1038/npjqi.2016.33
2. T. J. Green et al, New J. Phys. **15**, 905004 (2013), doi:10.1088/1367-2630/15/9/095004

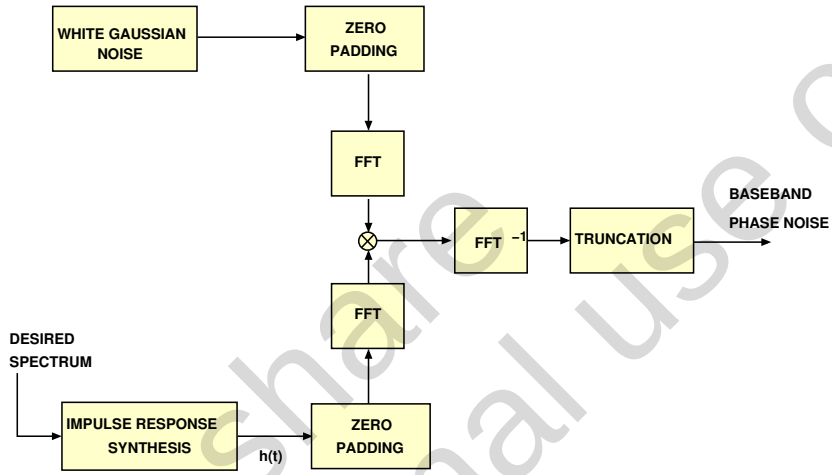

Figure 1: Block diagram of the numerical procedure to generate baseband phase noise.

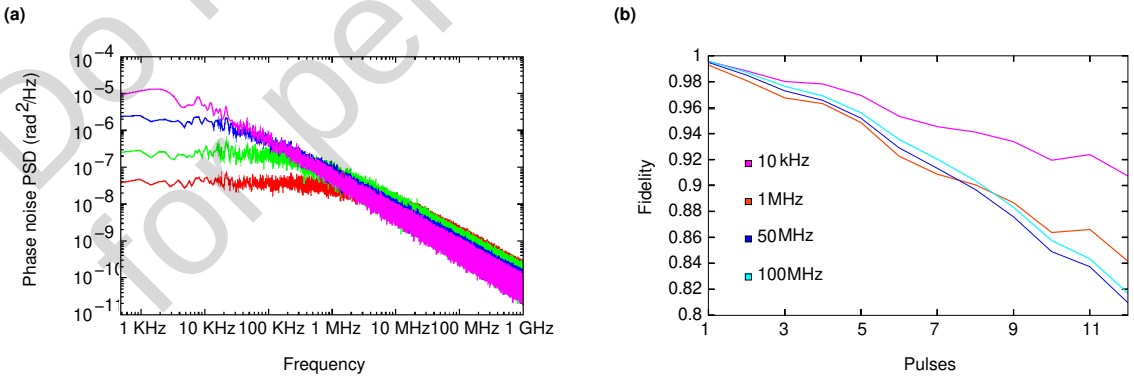

Figure 2: (a) Power spectral density of flicker-like noise for different corner frequencies: 1.59 kHz (magenta), 15.9 kHz (blue), 159 kHz (green), and 1.59 MHz (red). (b) Fidelity as a function of the corner frequency of the finite impulse response filter used to model phase noise.

ICNF-2025 June 17-20, 2025 – Taormina, Italy

What sounds make noises ?

Jean-Marc Routoure[1], Sylvain Lebargy[1], Julien Gasnier[1], Lucas Bessin[1], Nicolas Germain[2]

[1]GREYC Université de Caen-Normandie, Caen, France

[2]el TiGeR CoMiCs GRoUP http://www.jujuart.com

Corresponding author: jean-marc.routoure@unicaen.fr

Abstract:
An electronic setup dedicated to an artistic installation is described. The noise of a resistor is used as the primary signal for sound and image creation; therefore, care must be taken to avoid saturations in the amplifier.
Keywords: DC coupled amplifier, noise measurements, very low frequency measurements

Introduction:

In the context of the 2025 edition of *Interstices*—an artistic festival held in Caen, France, and one of the key events celebrating the city's millennium—five artist-scientist duos were selected by the festival committee to produce five original creations. This paper describes the electronic setup developed for the installation *What Sounds Make Noises?* (preliminary title) created by Nicolas Germain in collaboration with Jean-Marc Routoure as the scientific partner. The artist's intention is to use the noise signal produced by a solid-state electronic device as a source for real-time sound and image synthesis. Since solid-state devices are fabricated from mineral materials, the sound and image creations will be related to soundscapes as described in [1].

Given the real-time and sound quality constraints, the electronic setup was carefully designed to prevent any saturation or bumps of the noise signal as the DC voltage applied to the device varies.

Circuit description:

The device of interest is a resistor (*Rmesure*). A first voltage amplification stage, with gain G, is achieved using an AD8421 instrumentation amplifier, and a second amplification stage is implemented with a standard inverting amplifier. The total voltage gain, G_T, is approximately one thousand. The DC current flowing through the resistor is set using a voltage divider (R, *Rmesure*) and a digital-to-analog converter (DAC1). A second DAC (DAC2) provides a DC voltage applied to the REF input of the AD8421 to prevent saturation. Using 16-bit resolution provides sufficient accuracy to achieve proper DC compensation. The DC output value of the AD8421 is measured using an analog-to-digital converter (ADS110). Finally, an M5Stack module is used to control the two DACs and the ADC via an I2C bus.

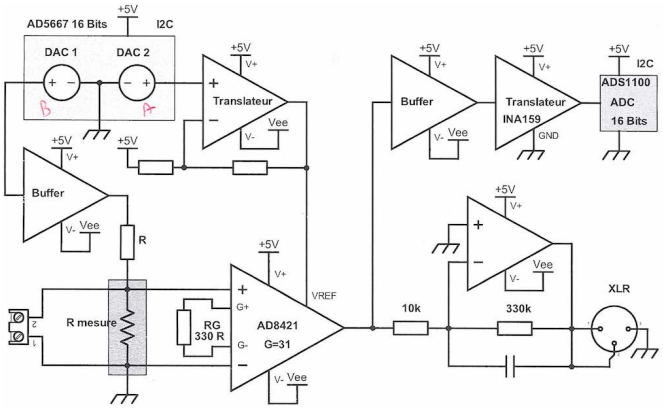

The voltage divider is not ideal for rejecting the noise of the bias system. A more sophisticated current source (for instance, as described in [2]) could have been used, but the performance was sufficient for the artist's requirements.

The system allows real-time DC current changes. Care must be taken to ensure that, after calculating the values, the voltages applied by DAC1 and DAC2 are set simultaneously. The DC-compensated voltage is given by:

$$DAC2 = G_T \cdot DAC1 \cdot \frac{Rmesure}{R + Rmesure} \tag{1}$$

Results:

The figure below shows the noise spectral density at the output of the amplifier for two values of the DC current flowing through the resistor: $I = 0$ and $I = 116$ μA, over a frequency range from 10 Hz to 100 kHz. The setup was completed with a PC connected to the M5Stack module.

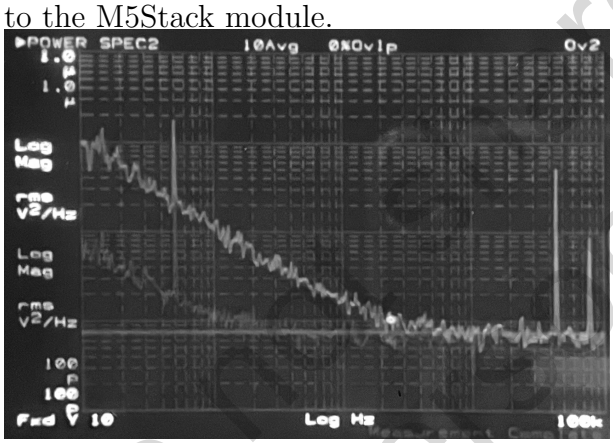

noise power spectral density at the output of the amplifier

For $I = 0$ (light grey curve), the white noise level is close to the expected value ($G_T^2 \cdot 4k_BTR_{\text{mesure}}$). The only parasitic line in the audio domain appears at 50 Hz. For $I = 116$ μA, a $1/f$ noise contribution is clearly visible, with a corner frequency around 10 kHz. For the artist's purpose, these results are sufficient for sound and image creation, as there are no significant parasitic lines and the $1/f$ noise falls within the audio frequency range.

Conclusions and perspectives: pruto

An electronic setup dedicated to noise amplification for an artistic installation has been presented. It fulfills the artist's requirements. With a dedicated low-noise bias system, the setup could be adapted to perform very low-frequency noise measurements, thanks to the DC-coupled behavior of the amplifier.

Jean-Marc Routoure would like to thank Luc Brou and David Dronet for the opportunity to work on this enthusiastic project.

References

1. Schafer, R. Murray "The soundscape : our sonic environment and the tuning of the world". 1994. ochester, Vt. : Destiny Books
2. Routoure et al. "A Low-Noise and Quasi-Ideal DC Current Source Dedicated to Four-Probe Low-Frequency Noise Measurements".IEEE Transactions on Instrumentation and Measurement (Volume: 69, Issue: 1, January 2020).

Control noise and control accuracy in gravitational wave detectors

M. Pinto[1], P. Ruggi[1], M. Mantovani[1], D. Bersanetti[2], J. Casanueva[1], M. Boldrini[3]
[1]European Gravitational Observatory
[2]INFN Sezione di Genova
[3]INFN Sezione di Roma1
manuel.pinto@ego-gw.it

Abstract: In the present work a short overview of the problem of the control noise in the low frequency range of the Gravitational Wave (GW) detectors sensitivity is tackled. Specific attention is given to the example of Virgo interferometer. An overview of the main source of technical noises will be given, considering the coupling mechanisms to GW signal, i.e. DARM, for both the longitudinal auxiliary DoFs and the angular DoFs. Techniques adopted to reduce the impact of control noise in the detection band will be presented, concluding with what are the current technical limitations and the future perspectives in order to reach further sensitivity with new generation gravitational wave detectors.

Keywords: gravitational wave, sensitivity, control noise.

Introduction Modern GW detectors, such as Advanced Virgo+ (AdV+), use a Michelson-based interferometer with a laser source and two 3 km long Fabry-Perot optical cavities [1]. The detector is operated in the so-called dark fringe condition, where destructive interference is achieved between the two recombined beams reflected by the interferometer arms. Using an interferometer to detect gravitational waves (GW) requires measuring the variation of length of the two arms (DARM). To detect extragalactic GW, the position of the main optical components needs to be controlled with very high accuracy, from 10^{-16} m to 10^{-12} m for longitudinal and 10^{-9} rad for angular DoFs. Given that the natural fluctuations of the mirrors, sustained by seismic background, would be several order of magnitude larger than the requirements, implies the necessity of actively control the whole set of optical elements composing the main degrees of freedom. The drawback of the implementation of active controls is the reinjection of residual control noise within the detection band, affecting the detector sensitivity.

Coupling to DARM Noisy components of the auxiliary DoFs coupled to DARM in the detection band, are due to the noise of the in-loop sensors used to control the degrees of freedom. The coupling is present also among the auxiliary DoFs and is affected by the presence of optical defects of the detector. We can limit the impact of this coupling acting on the hardware, to improve the sensing noise of photodiodes; performing sensing diagonalization between aux DoFs in order to reduce the interplay among them; implement subtraction with feed-forward techniques if the coupling is linear; refine control filter. Concerning the angular DoFs, when the beam is centered to the optics, angular noise is not coupled to the sensitivity. The angular noise coupling depends on the miscentering of the beam, which causes a change in the optical path length, resulting in longitudinal noise within the GW detection band.

Control filter optimization and low-frequency noise budget To reduce the impact of control noise in the detection band, one solution is to reduce the bandwidth (UGF) of the control loops (Fig. 1). By doing so, the achieved roll-off allows to reduce the coupling with the sensitivity within the detection band. However, a trade-off between noise roll-off and good low-frequency control accuracy imposes limitations to this technique. At low frequency, the overall residual motion is dominated by the residual ground motion, transmitted along the seismic attenuation chain (Fig. 2). The control actuators must compensate the residual motion of the optical components, without reintroducing too much noise and be strong enough not to saturate. To tackle the problem of the actuation noise, the hierarchical control (HC) strategy is adopted.

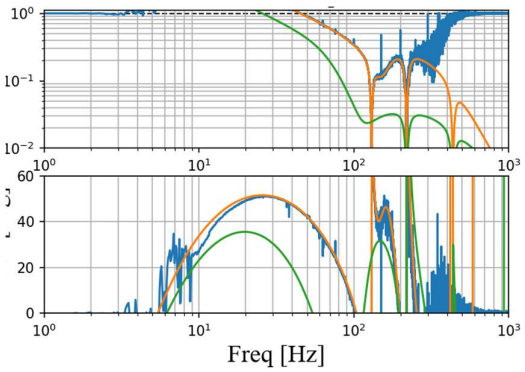

Fig. 1: Example of control bandwidth optimization for PRCL DoF.

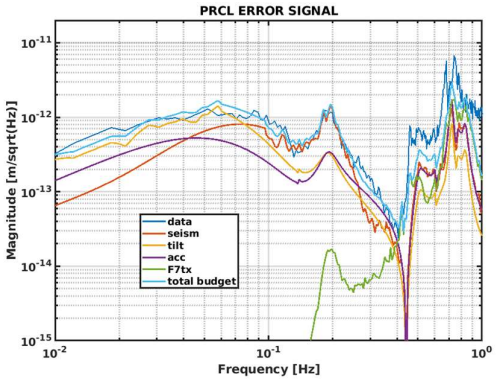

Fig. 2: Reconstructed LF noise budget for PRCL DoF. Ground motion is the main RMS contribution.

Actuation noise and hierarchical control In order to keep the TMs locked in the correct working point, it is necessary to exert a specific actuation force. This is a specific source of noise, whose level mainly depends on: i) the force required to compensate the residual motion of the mirrors/suspension; ii) the dynamic range of the actuation device. In Virgo, hierarchical control of the top-stage is adopted. It allows to optimally control the top stage, to filter the seismic disturbances transmitted from the ground to the mirrors, and so to reduce the needed dynamic range of the actuators (low-noise actuators) for the locking control of the test masses. To reduce the impact of the actuation strength on the test-mass residual motion, the needed locking correction frequency band is split and allocated at the available actuation points [2] (Fig. 3,4).

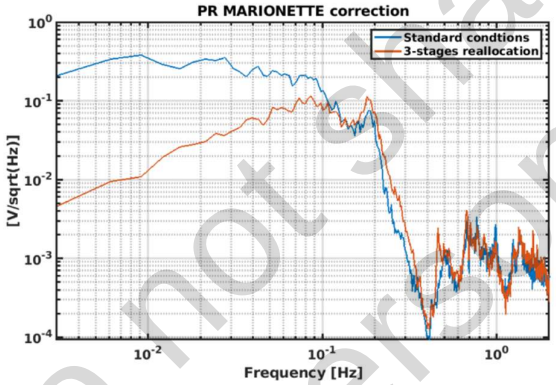

Fig. 3: Implementation of HC strategy to split PRCL correction between bottom stage and top stage.

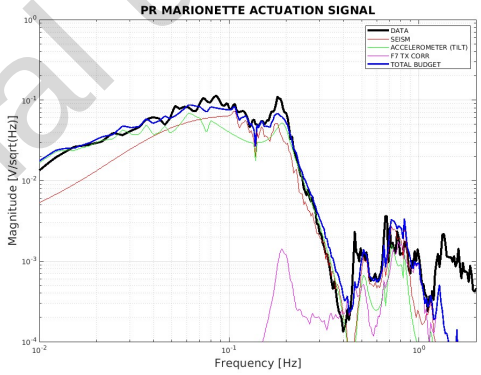

Fig. 4: Reconstructed PR Marionette LF locking correction signal.

Concluding remarks Reaching the low frequency design sensitivity is a challenge for the present detectors, which have as main limitations control noise. For next generation detectors the low frequency sensitivity will be even more challenging. Several orders of magnitude of improvement in the low frequency region are required. R&D activities towards new frontier of science are currently explored: strong R&D on seismic isolation system and its control strategy; possibility of working underground to limit the impact of seismic noise and in cryogenic environment to limit the impact of suspension thermal noise (just to name a few).

References

[1] F. Acernese et al. (Virgo), Advanced Virgo: a second-generation interferometric gravitational wave detector, Classical and quantum gravity 32, 024001 (2015).
[2] P. Ruggi, M. Pinto, E. Majorana, G. Losurdo - Advanced hierarchical control for Virgo and ET SA: modeling and experimental results. 3rd ET annual meeting, Warsaw November 13th 2024.

Low Frequency Noise and Resistivity of Hybrid MWCNT/Ni@C/Epoxy Composites

F. Mireckas[1], D. Meisak[1], S. Pralgauskaitė[1], J. Macutkevič[1], J. Matukas[1], J. Banys[1]

[1]Institute of Applied Electrodynamics and Telecommunications, Vilnius University, Vilnius, Lithuania
frydrichas.mireckas@ff.vu.lt

Abstract: Low frequency noise (20 Hz – 20 kHz) and electrical resistivity characteristics of hybrid composites with multi-walled carbon nanotubes and carbonized nickel were investigated to identify the characteristics of charge carrier transport. Electrical fluctuations in the investigated composite materials are comprised mainly of 1/*f* type components, arising due to the fluctuation of the number of free charge carriers. The carbon nanotube content more strongly influences the resistivity of the hybrid carbon nanotube and carbonized nickel composites, and the inclusion of different concentrations of carbonized nickel either increases or reduces the resistivity.

Keywords: carbon-coated Ni, carbon nanotubes, composite, low frequency noise

Introduction Composite materials with conductive carbon nanoparticle fillers have garnered great interest in science and industry due to their electrical, thermal and mechanical properties, as well as the tunability of their features using functionalization or varying filler concentration. However, such composites are vulnerable to agglomeration arising from Van der Waals interactions between individual filler particles [1]. Therefore, it is crucial to identify optimal filler concentrations for maintaining desirable properties. A possible solution is the fabrication of hybrid composites, as the inclusion of more than one type of filler can induce synergistic effects and help form a percolation network at lower concentrations of filler [2].

Low frequency noise measurements provide a means to non-destructively investigate charge carrier transport and electrical conductivity characteristics in composite materials [3]. The level of low frequency noise can be used as a measure of material quality, as materials with more structural defects generally exhibit higher noise levels. The level of 1/*f* noise is particularly notable, as it limits the sensitivity and selectivity of electrical sensors [4].

In this report we present an investigation of low frequency noise and electrical resistivity of hybrid MWCNT/Ni@C/epoxy composites, the purpose of which was to identify the characteristics of charge carrier transport in these composites.

Materials and methods Composites were prepared using standard filler dispersion protocols [5]. Single-filler Ni@C composites with 15, 25, and 30 vol.% of Ni@C, as well as hybrid MWCNT/Ni@C composites with 0.09 vol.% of MWCNT and 0, 0.025, 0.2, and 5 vol.% of Ni@C, were investigated. Bulk samples were investigated, with an average surface area of 16.8 mm^2 and an average thickness of 1.83 mm. Low frequency (20 Hz – 20 kHz) electrical fluctuations and electrical resistivity were measured at room temperature and in the temperature range of (75 – 365) K.

Results Resistivity of the investigated hybrid composites exhibits almost no dependence on voltage (Fig. 1). Lowest resistivity values are observed in composite samples with 30 vol.% and 15 vol.% Ni@C. The composite sample with 25 vol.% Ni@C exhibits a resistivity much higher than the other single-filler Ni@C composites, possibly due to a higher degree of

agglomeration in this composite (Fig. 1). The resistivity of hybrid MWCNT/Ni@C composites is generally more strongly influenced by the MWCNT content and shows no clear dependence on Ni@C concentration: the concentration of Ni@C where resistivity is lowest is found to be 0.2 vol.% Ni@C.

The noise spectra of the studied composites are essentially of 1/*f* type. At the lowest investigated concentration of Ni@C (0.025 vol.% Ni@C), the level of noise in the hybrid MWCNT/Ni@C composites is reduced in comparison to the single-filler MWCNT composite, possibly due to an improved distribution of filler particles by impeding agglomeration (Fig. 2). As the concentration of Ni@C is increased, the noise level increases, and the noise level of the hybrid 0.09 vol.% MWCNT and 5 vol.% Ni@C composite is almost equivalent to that of the single-filler 0.09 vol.% MWCNT composite (Fig. 2). The composite sample with 25 vol.% Ni@C is again an outlier – its noise level is very high when contrasted with the other composites, which suggests a high prevalence of aggregated particles acting as defect sites [1].

For the proportionality of voltage fluctuation spectral density to voltage $S_U \sim U^b$, exponent b is generally lower than two, which indicates a more significant contribution of tunneling processes to the conductivity in the material (Fig. 2). One exception is seen in the case of the composite with 15% Ni@C, where $b = 2$, characteristic of noise arising from fluctuations of resistance as a result of fluctuations of the number of charge carriers in the composite.

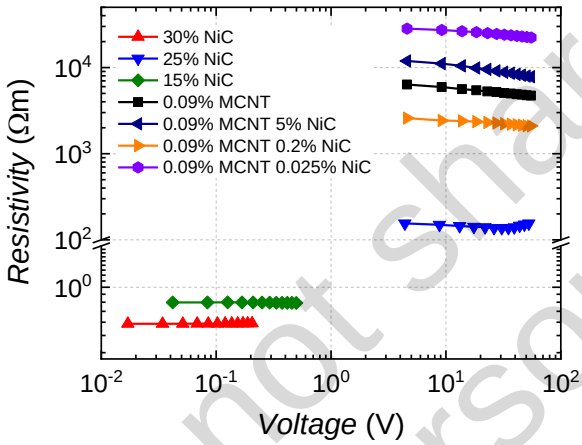

Fig. 1: Resistivity dependence on voltage at room temperature.

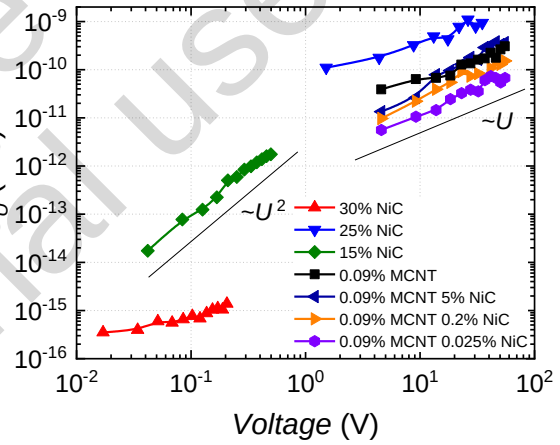

Fig. 2: Voltage noise spectral density dependence on sample voltage at room temperature, 86 Hz.

References

[1] V. Choudhary et al., "Carbon nanotubes and their composites", in Syntheses and Applications of Carbon Nanotubes and Their Composites, IntechOpen, 2013, pp. 193-222.
[2] U. Szeluga et al., "Synergy in hybrid polymer/nanocarbon composites. A review", Composites Part A, vol. 73, 2015, pp. 204-231.
[3] S. Pralgauskaitė et al., "Resistivity and low-frequency noise characteristics of epoxy-carbon composites", Journal of Applied Physics, vol. 121(11), 2017, pp. 114303.
[4] A.A. Balandin, "Low-frequency 1/f noise in graphene devices", Nature Nanotechnology, vol. 8(8), 2013, pp. 549–555.
[5] D. Meisak et al., "Dielectric relaxation spectroscopy and synergy effects in epoxy/MWCNT/Ni@C composites", Nanomaterials, vol. 11(2), 2021, p. 555.

Robustness of GaAs and GaN LNAs in X- and Ku-band: performances and strategies of protection under jamming or destructive signal

J.G. Tartarin[1,2], D. Saugnon[1]

[1]LAAS-CNRS, Toulouse, France
[2]University of Toulouse, Toulouse, France
tartarin@laas.fr

Abstract: Modern Radio communications or radar receivers can be subject to unintentional (jamming) or intentional (jamming or destruction) aggressions. Low Noise Amplifiers (LNA) are generally provided with an upstream protection system to prevent such effects, at the cost of a significant degradation of the noise factor (around 1dB of typical degradation in X- and Ku-band). This paper compares LNAs from two low noise technologies GaAs and GaN, on their electrical performances (parameters [S] and P_{1dB}) and in high frequency noise before (during) and after the application of RF step stress. Different protection strategies are used depending on the respective bandgap potential of GaAs and GaN technologies regarding the RF power to be supported. The advantages and weaknesses of these technologies are identified and discussed at the LNA level and its integration with possibly a limiter.

Keywords: Robust LNA, GaAs and GaN, MMIC, X-band and Ku-band step-stress, jamming.

Introduction: Enhancing Low Noise Amplifier (LNA) resilience using dedicated design or protective devices against RF jamming or high-power destructive signals is a real challenge as LNAs are very susceptible to these interferences, which can degrade performance or even cause permanent damage. Obviously, more than these reliability considerations, LNAs are primarily essential components of RF reception chains, responsible for amplifying weak signals while providing low noise levels. In this study, we propose a comparison of different protection strategies on LNAs made in GaAs and GaN technology, by comparing their electrical and noise performances in X- and Ku-band, before and after the application of RF step-stresses specific to each of the technologies. In addition to the intrinsic ability of the LNA to withstand high RF dynamic levels, protection devices (such as diode-based limiter or adaptive filter circuit) are typically used to improve the robustness of the LNA in hostile RF environments, at the expense of significant degradation of the noise figure (of the order of the noise figure of the LNA itself).

Step-stress configuration and measurement procedure:
Depending on the low or high bandgap technology used (resp. GaAs and GaN), the stress conditions are adapted to evaluate a stress zone compatible with the operational maintenance of the LNAs after the application of RF constraints. A batch of three LNAs is measured for each technology, but only one case study representative of each batch is illustrated in this work. The experimental bench uses a PNA-X N5244B from Keysight with option 029 for low noise measurement under 50 ohms (NF50). Each LNA is measured regarding S-parameters, DC bias and NF_{50} before the application of the stress and after each step-stress sequence ($LNA_{\#A}$) or at the end of the stress sequence ($LNA_{\#B}$ and $LNA_{\#C}$). During the RF stress sequence, one strategy uses an unbiased LNA to avoid early compression and management of incident RF powers that would cause severe degradation (GaAs), while the other strategy maintains the DC bias of the LNA which so continues to be operational (GaN). GaAs-based LNAs are subjected to step stresses up to 10 dBm (the DC bias of the amplifier is disabled during stress), while GaN-based LNAs (from 2 technologies) experience RF stresses up to 35 or 38 dBm until destruction (DC bias enabled).

Robustness of GaAs LNA$_{\#A}$ (3 stage, 26 dB gain) up to 10 dBm @ 13.5 GHz:
For this protection strategy, the DC bias is disabled during the step stress sequence (1 h per step, 2 dB per increment). After the 10 dBm RF stress step, S parameters remain almost unchanged, with a slight improvement of the gain S_{21} by +0.5 dB (IP_{1dB} simultaneously decreases by 0.5 dB) as a result of an increase in the transconductance gain g_m when the I_{DS} bias current decreases (by 3% in this case). The NF50 initially measured at 1.2 dB degrades by 0.6 dB after the RF stress sequence. After 34 hours of rest, the LNA recovers 80% of its initial DC/RF electrical performance, but the noise figure remains slightly degraded by +0.6 dB. The low RF power (+10 dBm for this study) is not sufficient to be considered for robust jamming or destruction applications. Even with the DC bias disabled during the attack as measured in this work, a limiter must be added to ensure LNA survival: the protection devices limit power levels above 10 dBm, but adding a limiter degrades the overall noise figure by 0.8 dB to 1.5 dB, which is a major drawback of this design strategy in terms of receiver sensitivity. Moreover, the limiter should be integrated on the same chip to save space. For this purpose, wide bandgap technologies such as Nitride technologies are used.

Robustness of GaN LNA$_{\#B}$ (3 stage, 24 dB gain) up to 38 dBm @ 13.5 GHz:
For this protection strategy, the DC bias is maintained as when no unwanted RF signal occurs, during the step stress sequence (1 h per step, 3 dB per increment). No degradation is revealed on S-parameters up to 35 dBm input power, but a degradation on S_{11} and S_{22} occurs at +38 dBm. A degradation by 12 dB on S_{21} (destruction of some finger gates/diodes of the first stage of LNA$_{\#B}$) translates into a 12 dB degradation on the NF_{50}=2 dB initially measured (Fig. 1). This LNA$_{\#B}$ design keeps all [S] and NF_{50} parameters stable up to 35 dBm input RF signal. Another GaN foundry is used to design a third LNA$_{\#C}$, whose protection strategy is based on its self-reconfiguration from low noise mode (no RF aggression) to high linearity mode (under critical RF signal) as described in [1] for a single-stage version. This rugged 2-stage LNA$_{\#C}$ features 21 dB gain and lower 1.5 dB noise figure. Discussions of electrical and noise evolution during stress will be covered in more detail, and figures will complete this 2-page version.

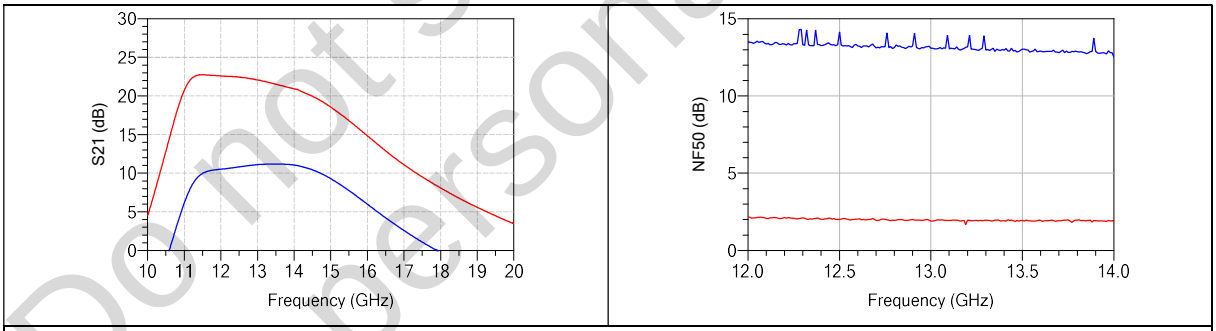

Fig. 1: S_{21} and NF_{50} for LNA$_{\#B}$ before (red line) and after (blue line) the step-stress sequence up to 38 dBm.

Conclusions

Different strategies for robust LNAs are presented through their ability to sustain elevated RF jamming or destructive signals, based on GaAs or GaN technologies. GaAs requires a limiter while GaN can withstand stress levels over 100 times higher without degradation, without turning off the DC bias, and without needing a limiter. Comparisons between these design strategies allow us to better appreciate the competition now available to LNA designers in a global approach, beyond the usual characterizations which do not take into account the application of aggressive constraints.

References

[1] B. Pinault et al., “Impact of RF stress on different topologies of 100 nm X-band robust GaN LNAs”, Microelectronics Reliability Journal, Elsevier, vol. 150, nov. 2023, 115126.

Statistical Modeling of Timing Variability due to Random Telegraph Noise

G. I. Wirth[1], T. H. Both[2], M. B. Silva[3] and L. Van Brandt[4]

[1] Electrical Eng., UFRGS, Porto Alegre, Brazil
[2] NXP Semiconductors, Eindhoven, Netherlands
[3] Department of Electronics and Computing, UFSM, Santa Maria, Brazil
[4] Inst. for Information and Communication Techn., UCLouvain, Louvain-la-Neuve, Belgium
wirth@inf.ufrgs.br

Abstract: In MOSFETs of nanometer dimensions, stochastic performance variations are produced by factors other than variability of physical dimensions and doping profiles, which remain static over lifetime. Besides these time-zero variability effects, other factors that lead to performance variation from one instant in time to the other start playing a significant role. Random Telegraph Noise (RTN) is among these relevant time-dependent variability sources. Due to the intrinsic nature of RTN each device has a different probability of time-fluctuations on the threshold voltage ($V_T(t)$), by consequence each device has a different variance for threshold voltage fluctuations. In this work we model the variability of these variances, induced by RTN. The area scaling of this variability effect is detailed and discussed, supporting designers in transistors sizing towards a more reliable design. Additionally, it is demonstrated that it is possible to employ sensitivity analysis, in conjunction with the analytical model presented, to implement automated, fast and accurate estimations of the time-dependent performance variability of devices, logic gates and circuits composed of MOSFETs. Monte Carlo (MC) simulations are run to corroborate the model and illustrate its applicability.

Keywords: Device variability, random telegraph noise, time-dependent variations.

Introduction Yield and reliability of integrated circuits depend on the variability of the transistor parameters and on noise power. Both parameter variability and noise scale inversely with area [1]. Conversely, cost scales directly with area, and increasing area may also increase capacitive load, decreasing performance and increasing power. For the designer to find an adequate balance between cost, reliability and performance, statistical models are needed.
Static (time-zero) sources of variability, are not expected to induce jitter of signals, which are a result of time-varying parameters. In digital circuits RTN may cause propagation delay fluctuations. Each device has a different RTN behavior. This is of particular importance for nanometer-size devices in which time dependent within-device fluctuations is impacted by device to device variability [1]. Thus, a fully stochastic model that encompasses within-device fluctuations accounting for device to device variations is required.
We provide an analytical model for the time dependent threshold voltage fluctuation produced by RTN. We address not only the average value, but also its variability among devices. Besides analytical modeling, Monte Carlo simulations are run and corroborate the analytical model. The area scaling of RTN induced time dependent threshold voltage fluctuation and its variability among devices is detailed and discussed. The applicability of the model to the evaluation of logic gates and circuits is demonstrated by the case study of inverters and ring oscillators.

Threshold Voltage Variance The variance of $V_T(t)$ of a single device, i.e. the time dependent within device fluctuation, here called $V_{Tjitter}^2$, is evaluated as (1), while the ensemble variance of $V_{Tjitter}^2$ can be evaluated as (2) [2]

$$E\left[V_{Tjitter}^2\right] = E[n]E[A^2] \quad (1) \qquad Var\left[V_{Tjitter}^2\right] = E[n]E[A^4] \quad (2)$$

Where A is the RTN amplitude due to a trap and n is the number of traps per device.

From (1) and (2), normalized standard deviation is inversely proportional to square root of area:

$$\sigma\left[V_{Tjitter}^2\right]/E\left[V_{Tjitter}^2\right] = \sqrt{E[n]E[A^4]}/E[n]E[A^2] \propto 1/\sqrt{WL} \quad (3)$$

Area downscaling not only increases the expected value of $V_{Tjitter}^2$ (within-device time-dependent fluctuations) but also increases the variability of $V_{Tjitter}^2$ (device-to-device variation).

Variance (Jitter) of CMOS Logic Gate Delay RTN causes fluctuations of the drive (drain) current, affecting the propagation delay. Using propagation of uncertainty, the variance of the propagation delay of an inverter ($\sigma_{t_p}^2$) can be estimated using

$$\sigma_{t_p}^2 = \frac{1}{2}\left(\frac{\partial t_{pHL}}{\partial \Delta V_{T_N}}\right)^2 V_{Tjitter,N}^2 + \frac{1}{2}\left(\frac{\partial t_{pLH}}{\partial \Delta V_{T_P}}\right)^2 V_{Tjitter,P}^2 \quad (4)$$

Jitter in Ring Oscillators Once the delay jitter of an inverter has been derived, one can derive the jitter in circuits composed of inverters. For a ring oscillator of *M* stages

$$E[\sigma_{Trosc}^2] = M\left(\frac{\partial t_{pHL}}{\partial \Delta V_{T_N}}\right)^2 E\left[V_{Tjitter}^2, N\right] + M\left(\frac{\partial t_{pLH}}{\partial \Delta V_{T_P}}\right)^2 E\left[V_{Tjitter}^2, P\right] \quad (5)$$

$$Var[\sigma_{Trosc}^2] = M\left(\frac{\partial t_{pHL}}{\partial \Delta V_{T_N}}\right)^4 Var\left[V_{Tjitter}^2, N\right] + M\left(\frac{\partial t_{pLH}}{\partial \Delta V_{T_P}}\right)^4 Var\left[V_{Tjitter}^2, P\right] \quad (6)$$

From (5) and (6), $E[\sigma_{Trosc}^2]$ scales with $1/(WL)$ and $Var[\sigma_{Trosc}^2]$ scales with $1/(WL)^3$. Hence, the normalized standard deviation, $\sqrt{Var[\sigma_{Trosc}^2]}/E[\sigma_{Trosc}^2]$, scales with $1/\sqrt{WL}$.

Fig. 1 shows the results of MC simulation of ring oscillator period jitter, run using NGSPICE and a modified set of BSIM4 equations [3]. Trap kinetics were implemented within the BSIM4 model. The transistor model employed is Predictive Technology Model for the 22-nm node.

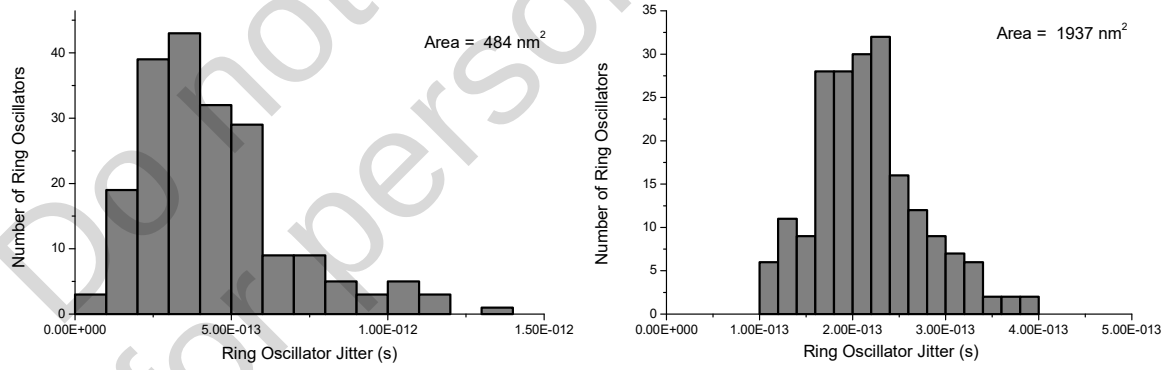

Fig. 1. Histogram of Monte Carlo simulations of ring osc. period jitter $\sigma_{T,Ring}$ for different device sizes. With area downscaling, not only the average value increases from 2.2E-13 s to 5.0E-13 s, but also the normalized standard deviation (variation among devices; spread of the jitter distribution) increases from 0.53 to 1.16. MC results are in close agreement with the analytical model (in the full paper, analytical calculations will be detailed and all values presented). This increase in variability with decreasing device size has been experimentally observed [e.g. 4].

References

[1] M. Simicic et al. IEEE Trans. on VLSI Systems, pp. 601-610, 2019. DOI: 10.1109/TVLSI.2018.2878841
[2] G. Wirth. IEEE Trans. on Electron Devices, pp. 17-23, 2021. DOI: 10.1109/TED.2020.3039204
[3] T. H. Both et al. Microelectronics Reliab., pp. 278-283, 2018. DOI: 10.1016/j.microrel.2017.11.009
[4] T. Matsumoto et al. 2012 International Electron Dev. Meeting, DOI: 10.1109/IEDM.2012.6479104.

Quantum Channel FETs for Advanced Biosensors

D. Pustovyi[1], M.Petrychuk[1,3], A.Fujiwara[2], Y.Zhang[1], H.Long[1], V.Chekubasheva[1], S.Vitusevich[1]

[1]Institute of Biological Information Processing (IBI-3), Forschungszentrum Jülich, Jülich, Germany
[2]NTT Basic Research Laboratories, NTT Corporation, Atsugi, Kanagawa, Japan
[3]Taras Shevchenko National University of Kyiv, Ukraine
Email address: s.vitusevich@fz-juelich.de

Abstract: Highly sensitive high-speed biosensors are key devices for precise diagnostics and for the application of medical treatment in good time. In this paper, noise spectra and characteristic time constants are studied in nanotransistors with channel sizes below 30nm. The quantization effect due to the formation of a quantum dot channel is analyzed based on the transport and noise properties of the device structures. Ultra-low flicker noise at the quantum level with a Hooge parameter of about 10^{-8} is registered. A strong dependence of the characteristic switching time on the modulation effect is revealed with a slope (-6) that considerably exceeds the value of 1, which is typically obtained in large-area device structures. This reflects the fact that an amplification of 600% can be obtained in nanotransistor biosensors.

Keywords: Quantum dot channel, modulation effect, nanotransistor biosensor

Introduction Reducing the size of metal–oxide–semiconductor field-effect transistor (MOSFET) structures not only enables high-speed transport regimes to be achieved in the structures, but also enhances the role of quantum conduction mechanisms. These mechanisms include the ballistic transport regime, resonant tunneling conduction, and Coulomb blockade transport in channels. These mechanisms are also manifested in the nature of low-frequency noise. The flicker noise caused by the correlation of quantum states is considered to be quantum noise [1]. Recently, new characteristic times have been suggested to amplify the biosensitivity of biosensors [2 and references therein] due to the modulation effect in nanowire FET device structures. However, such a modulation effect for biosensing applications remains unexplored in FET structures with a quantum dot (QD) channel for the possible design of biosensors utilizing quantization in the channel. In this work, the transport and noise properties of QD FETs, fabricated using a silicon-on-insulator wafer, are studied. The structures also have a Coulomb blockade transport regime with a Hooge parameter of 10^{-8}, which is crucially important for a lot of quantum applications. An extremely low flicker noise in the structures allows for the analysis of generation–recombination (GR) components and two-level signals (TLSs) corresponding to the GR bumps in QD FETs. The characteristic time constant is revealed to have a strong dependence on gate voltage. The obtained results open up prospects for the amplification of very small biological signals using QD FET biosensors.

Materials and methods The transport and noise properties of nanotransitors, fabricated using silicon-on-insulator wafers (SOI) with nanochannel sizes below 60nm, were studied. I–V characteristics were measured using an in-house experimental setup with computer-controlled software, which ensured a high level of repeatability for the measurement data. The setup allows for the current to be measured at a level down to $4 \cdot 10^{-10}$ A. The applied voltages ranged from -0.5 V to +3 V for the drain and gate voltages. The main measuring instruments were Keithley 2400 devices. Families of output and transient characteristics were measured in a single cycle. Noise spectra were measured in a frequency range from 1Hz to 100 kHz using an in-house measurement setup, which also allowed for studies of current fluctuations as time traces.

Results and discussion The typical noise spectrum of QD FETs is shown in Fig.1A. It should be emphasized that an extremely low 1/f noise level is registered in the QD channel at room temperature. The Hooge parameter is estimated using the following equation:

$$\alpha_H = \frac{S_I}{I^2}\frac{1}{fN} \quad (1)$$

where S_I is the spectral current noise density of the $1/f$ component, f is the frequency, I is the current drain, and N is the total number of current carriers.

The value of the Hooge parameter is estimated to be about 10^{-8}. The value is four orders of magnitude smaller $\alpha_H \sim 10^{-4}$ than values that are typically obtained for large-area Si MOSFETs. A well-resolved GR components and corresponding two-level signals in time traces are analyzed (Fig.1B). Characteristic capture time plotted as a function of gate voltage demonstrates a logarithmic slope equal to (-6) (Fig.1C), which considerably exceeds the value of (1) that is typically registered and described within the Shockley–Read–Hall (SRH) model for the bulk silicon channel. Such strong slopes, which were obtained for several nanoFET samples, indicate a promising future for the implementation of nanoFETs as highly sensitive sensors, including biosensing applications.

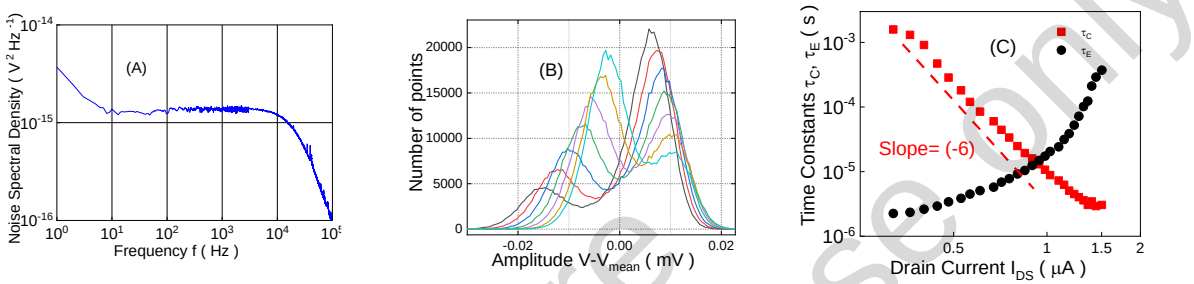

Fig. 1(A) Typical noise spectrum, measured for a gate voltage of 3.0 V; (B) histograms derived from two-level time traces clearly illustrate separated Gaussians peaks with an increase in V_{GS} (mV):43.4, 50.3, 53.5, 58.3, 63.4, 69.6, 73.6 ; (C) capture time constants vs current in the channel of the QD FET structure, Slope equal to (-6) is revealed, reflecting that 600 % amplification in sensitivity can be obtained for biosensing applications.

The strong behavior of the time constants in Fig. 1C can be explained by the fact that electron transport occurs here with participation of quantum energy levels in a quantum dot formed between source and drain barriers. When the gate voltage changes, not only quantum energy level changes, but also energies of barrier regions, which leads to significant changes in the quantum transmissions in nano FETs. The probability of such transmissions is controlled by Coulomb Blockade effect, which is why the values of both time constants can be tuned by drain current controlled by applied gate voltage. Thus, ultra-low noise nano FETs allow for the implementation of the QD itself to generate TLSs, useful for utilization in advanced biosensors.

Conclusions Our results demonstrate that quantum dot channels are promising systems to reach the limits in 1/f noise with Hooge parameter values of about 10^{-8}, which corresponds to the quantum noise level. Moreover, the quantization in energy states due to the QD enables a two-level signal to be realized with characteristic time constants corresponding to the capture–decapture of charge carrier, which is strongly dependent on the gate voltage. In contrast to bulk materials, which exhibit a slope (1) as a function of characteristic time vs gate voltage, QD FETs demonstrate a slope (-6) as a function of gate voltage. This reflects the fact that a 600% amplification in the sensitivity of biosensors can be achieved.

References

[1] C. M. Van Vliet, “Quantum Electrodynamical Theory of Infrared Effects in Condensed Matter II: Radiative Corrections of Cross Sections and Scattering Rates and Quantum 1/f Noise”, Physica A , vol. 165, 1990, pp. 126-155.

[2] M.Petrychuk et al, “New approach for enhancing sensitivity in liquid-gated nanowire FET biosensors under optical excitation”. Advanced Materials Technologies, vol.9,2024, pp. 2301303-1-9.

Fundamental quantum and relativistic formulation of noise and conductance in a 1D quasi-particle ensemble under ballistic transport-regime at thermal equilibrium

L. Reggiani[1], E. Alfinito[1], F. Intini[2], L. Varani[3]

[1]Department of Mathematics and Physics "Ennio de Giorgi", University of Salento, Lecce, Italy

[2]Department of Engineering "Enzo Ferrari", University of Modena and Reggio Emilia, Modena, Italy

[3]Institut d'Electronique et des Systèmes, University of Montpellier, Montpellier, France

luca.varani@umontpellier.fr

Abstract

Starting from the classical noise model of Nyquist (1926) [1] for a 3D conducting sample at thermal equilibrium, we generalize the spectral density of current fluctuations to the case of quantum-relativistic conditions that avoid vacuum catastrophe associated with zero-point energy contributions at increasing frequencies of the electromagnetic spectrum. Then, at low frequencies, we generalize the electrical current fluctuations for the case of a 1D ballistic transport-regime that, by recovering Landauer results (1956), generalizes current fluctuations to the case of a set of non interacting quasi-particles like: particle number N, neutral particle mass m, independent from the kind of statistics, but far from Bose Einstein condensation. The 1D ballistic regime is required to assure the existence of a single time scale for the system, that is the ballistic transit time. Finally the relativistic-quantum condition is analyzed for the simple 1D blackbody model.

Keywords: Vacuum catastrophe, quasi-particle, one-dimensional conductance, ballistic transport regime.

Introduction: We briefly discuss the problem of the zero-point contribution to the fluctuations and propose to solve the vacuum catastrophe prediction by introducing the quantum Casimir force and its effects on the boundary introduced by the presence of a finite dimension due to the presence of a physical device of finite volume. Then we present the case of the 1D, ballistic conductor and briefly discuss the classical, quantum and quantum relativistic expressions for the spectral density of current fluctuations and the linear response conductance in the conditions of near static frequency domain. The different 1D ballistic cases are summarized in Table 1.

Casimir effect: From Callen-Welton [2] and Kubo [3] (1951-1945) the frequency-dependent spectral density of current fluctuations $S_I(f)$ can be written as :

$$S_I(f) = 4k_BT\mathrm{Re}\left[Y(f)\right]\frac{x}{e^x-1} + \frac{1}{2}hf \tag{1}$$

with k_B the Boltzmann constant, T the absolute temperatur, Y the device admittance and h the Planck constant. By summing over all the frequencies the second term in eq.(1) gives $1/2\sum_f hf = \infty$ i.e. the so-called vacuum catastrophe.

Reggiani and Alfinito [3] in 2018 proposed to put $1/2\sum_f hf = U_{Casimir}$ with $U_{Casimir}$ the energy associated with the Casimir effect thus obtaining, instead of a divergence, a finite value. Indeed $U_{Casimir}$ does not contribute to fluctuations but to the stability of the physical system thus washing out the vacuum catastrophe.

quasi-particle (qp)	Diffusion $D_{\rm qp}$	Conductance $G_{\rm qp}$
N	h/m	$1/h$
e	h/m	e^2/h
m	h/m	m^2/h
ϵ	h/m_r	ϵ^2/h
th	h/m	$\frac{\pi^2}{3}\frac{k_BT}{h}$
pht	cL	$\frac{\pi^5}{15\zeta(3)}k_B\frac{c}{L}$
phn	sL	$\frac{\pi^5}{15\zeta(3)}k_B\frac{s}{L}$
em – vacuum	cL	$\epsilon_0 c$

Table 1: Diffusion and universal units of quantum conductance for a 1D ballistic conductor of length L for a quantum gas of non-interacting quasi-particle (qp) of given spin/polarization: number (N), electrical (e), massive (m), single photon-energy (ϵ), thermal carrier-energy (th), black-body photon-energy (pht), phonon-energy (phn), electro-magnetic (em)). Here h is the Planck constant, c the light velocity in vacuum, $m_r c^2 = \epsilon$ the relativistic equivalent mass-energy, k_B the Boltzmann constant, T the absolute temperature, s an average acoustic phonon velocity, ϵ_0 the vacuum permittivity.

1D ballistic classical: For 1D ballistic (b) quasi-particles (qp) at $f \to 0$ it is:

$$S^{\rm b}_{\rm Iqp} = 4k_BTG^{\rm b}_{\rm qp} = \frac{4\overline{\delta N^2}({\rm qp})^2}{\tau_T} \tag{2}$$

that implies an extended Drude model for the ballistic generalized qp conductance $G^{\rm b}$:

$$G^{\rm b} = \frac{G^{\rm b}_{\rm qp}}{({\rm qp})^2} = \frac{\overline{\delta N^2}}{h_c} = \frac{\overline{N}}{h_c} \tag{3}$$

with $h_c = m\sqrt{\overline{u_x'^2}}L$ the classical action, $\tau_T = L/\sqrt{\overline{u_x'^2}}$ the transit time and $\delta N^2 = \overline{N}$.
1D ballistic quantum: The quantum case is obtained by setting: $h_c = h, \overline{N} = 2$ and $G^{\rm b}$ becomes the fundamental unit of the 1D quantum ballistic generalized conductance of any quasi-particle gas, since the Planck constant h is a universal constant independent of the kind of quasi-particle.
1D ballistic quantum-relativistic: More interesting is the case of photons with energy hf that being quantum-relativistic by considering a 1D black-body structure gives:

$$S_{ph} = \frac{4(hf)^2\overline{\delta N^2}}{\tau_T} \tag{4}$$

with $\tau_T = L/c$

$$G_{ph} = \frac{(hf)^2\overline{N}}{h} \tag{5}$$

Conclusions We have reported a general survey of the quantum-relativistic relations of noise and conductance in 1D ballistic devices. Experimental results for the conductances are present in the literature since the pioneer work of Landauer in 1945 and still continue for the case of neutral massive quasi-particles. To our knowledge, no experiments are yet available for the case of photon gas conductance and noise.

References

1. H. Nyquist, Thermal agitation of electric charge in conductors, Phys. Rev. vol. 32, 1928, p. 110
2. H. Callen and T. Welton, Irreversibility and generalized noise, Phys. Rev. vol. 83, 1951, p. 34
3. R. Kubo, Statistical-Mechanical Theory of Irreversible Processes, I. Phys. Soc. Japan vol. 12, 1957, p. 570; ibidem, The Fluctuation-Dissipation Theorem, Rep. Prog. Phys. vol. 29, 1966, p. 255
4. Reggiani L and Alfinito E (2020). Beyond the Formulations of the Fluctuation Dissipation Theorem Given by Callen and Welton (1951) and Expanded by Kubo (1966). Front. Phys. 8:238. doi: 10.3389/fphy.2020.00238

Absence of skewness in the voltage fluctuations of a tunnel junction in the quantum regime

C. Farley[1], B. Reulet[1]

[1]Département de physique, Institut Quantique, Université de Sherbrooke, Sherbrooke QC, Canada

clovis.farley@usherbrooke.ca

bertrand.reulet@usherbrooke.ca

Abstract: Current fluctuations in a tunnel junction have a remarkable property: on one hand their variance corresponds to vacuum fluctuations at low voltage bias V, when the electron energy eV is smaller than the photon detection energy hf. On the other hand their skewness, i.e. their third moment, is frequency independent, equal to e^2I as if electron transport was simply Poissonian. We address the following question: Could it be that at low voltage, the vacuum fluctuations generated by the junction have a finite skewness, i.e. that the junction generates skewed vacuum ? To answer this question we calculate the effect of an arbitrary electromagnetic environment at zero temperature and show that the bispectrum of third moment of voltage fluctuations is always zero at frequencies larger than the voltage. We also show experimental data in the quantum regime that agree with our calculation.
Keywords: Quantum Noise, electron transport, skewness, electromagnetic environment, high frequency noise

Introduction.
The third moment of current/voltage fluctuations in an electrical device is known to be dependent on the electromagnetic environment of the sample, i.e. the circuit to which it is connected. This happens as soon as the variance of current/voltage fluctuations depends on the bias voltage of the device, i.e. for all components but a linear resistor. This comes from two factors: i) external voltage fluctuations modulate the noise of the device, and ii) current fluctuations generated by the device generate voltage fluctuations on the device itself through the external impedance to which the device is connected. These contributions add to the intrinsic skewness of the component.
A general problem of quantum noise of an electronic conductor is to understand how electronic fluctuations imprint their statistical properties in the electromagnetic radiation they generate. In the case of the variance of fluctuations, the link between current fluctuations and electromagnetic power detected at frequency f is well understood and depends on the detection scheme (photon detector, voltage detector, etc.). In the case of a classical detector, the averaged square voltage measured at frequency f is proportionnal to $n(f)+\frac{1}{2}$ with $n(f)$ the number of photons per second emitted in the detection bandwidth. The $1/2$ background corresponds to vacuum fluctuations. If electrons are given an energy $eV < hf$ they cannot emit photons so $n(f) = 0$ and the detected noise is that of vacuum fluctuations.
Here we want to probe what happens to the bispectrum $\langle v(f_1)v(f_2)v(f_3)\rangle$ in the limit where all frequencies f_i are greater than eV/h, i.e. in the full quantum regime where the variance of the noise is that of vacuum. Could it be that the vacuum generated by a quantum conductor at low bias is skewed ? Or is it that the environmental contributions always conspire to make the skewness vanish in this regime ?

Theory. We consider the general case depicted in Fig. 1: a quantum conductor of resistance R

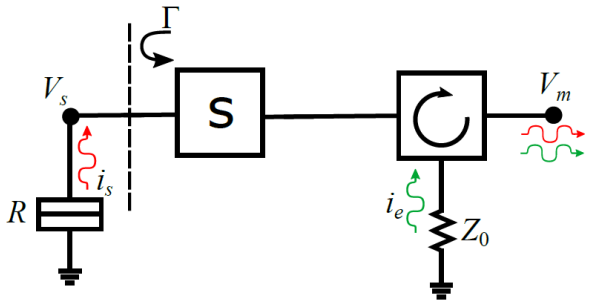

Figure 1: Detection scheme. Green arrows represent the vacuum fluctutaions generated by the load Z_0. Red arrows represent the noise generated by the sample.

is connected to a perfect amplifier via an arbitrary scattering matrix S. The perfect amplifier is made of a circulator with a load Z_0 at zero temperature, followed by a real amplifier. With such a scheme, the fluctuations generated by both the conductor and the vacuum fluctuations generated by the load of the circulator are partially reflected by the environment and partially transmitted to the amplifier. All parasitic capacitances, inductances, delay lines, etc are incorporated in the S-matrix of the environment.

More precisely, the detected voltage is given by $v(f) = t_e Z_0 i_e + t_s R i_s$ and the voltage fluctuations experienced by the sample $v_s = \alpha_e Z_0 i_e + \alpha_s R i_s$. The amplitudes $t_{e,i}$ and $\alpha_{e,s}$ are calculated according to the circuit of Fig.1 and are related to the matrix S and the voltage reflection coefficient $\Gamma = (R - Z_0)/(R + Z_0)$ of a wave on the sample. The skewness spectral density involves correlators of the form $\langle i_e(f_1) i_s(f_2) i_s(f_3)\rangle$ which corresponds to the modulation of the sample noise by the external vacuum fluctuations. These are proportional to the noise susceptibility times $\langle i_e(f_1) i_e(-f_1)\rangle$. Correlator $\langle i_s(f_1) i_s(f_2) i_s(f_3)\rangle$ contains the intrinsic third moment and the feedback terms which involves the noise generated by the sample times its noise suscpetibility.

By adding all those terms we find that $\langle v(f_1) v(f_2) v(f_3)\rangle = 0$ at low voltage: the quantum conductor does not generated skewed vacuum.

Experiment. We have performed measurements of the skewness of voltage fluctuations generated by a tunnel junction measured at frequencies $f_2 = f_2 = f$, $f_3 = -2f$ with $f = 5.05$ GHz. We have measured a tunnel junction of resistance $R = 93\Omega$, i.e. relatively matched to the detection setup ($Z_0 = 50\Omega$) as well as a much more resistive sample of resistance $R = 505\Omega$. For the latter, the detection is almost a perfect ammeter for which environmental corrections are small, so for which the intrinsic contributions $e^2 I$ is expected to dominate, leading to nonzero third moment. In both cases we observe that the skewness vanishes at zero voltage, in agreement with our calculations.

Perspectives. We have shown that the skewness of the electromagnetic field radiated by a quantum conductor at low voltage always vanishes. While this makes sense physically, it demands for a physical interpretation in terms of detection and raises the question of what would happen for another type of detection, that e.g. involves correlation between a voltage amplifier and a photon counter.

Autonomous Steady-State Entanglement in Two-Mode Bosonic Systems Coupled to Uncorrelated Baths

K. Kawa[1,2], K. Roszak[1], R. Filip[3], T. Novotný[2]

[1]Institute of Physics of the Czech Academy of Sciences, Prague, Czech Republic
[2]Department of Condensed Matter Physics, Faculty of Mathematics and Physics, Charles University, Prague, Czech Republic
[3]Department of Optics, Palacky University Olomouc, Olomouc, Czech Republic
tomas.novotny@matfyz.cuni.cz

Abstract: We study the generation of autonomous entanglement present in the nonequilibrium steady state of two bosonic modes each coupled to their own independent and uncorrelated thermal baths held at different temperatures. We show that, counter-intuitively, under suitably engineered coupling between the modes and their reservoirs, finite entanglement can be achieved.

Keywords: entanglement, quantum dissipative systems, nonequilibrium steady state

Introduction Theory of open quantum systems, i.e., systems coupled to thermal bath(s) in the quantum regime [1] despite of its age still constitutes a vivid research field addressing various aspects of the general question how the dissipative coupling to a bath, which inevitably also brings quantum noise, influences the quantum dynamics of the studied system. The question is particularly important in the context of quantum information setups where quantum resources such as coherence or entanglement should be prevented from the (supposedly) detrimental effects of the noise. However, as has turned out recently, the sole dissipative coupling of quantum systems without any further external control (such as driving fields) can, in fact, also be used for generation of such quantum resources, which are then called *autonomous* [2,3].

Results Entanglement generation in open quantum systems is typically hindered by decoherence effects because of the inevitable contact of the quantum system to the environment. However, we demonstrate that a properly engineered interaction with the environment can autonomously drive a system into an entangled steady state. We analyze theoretically a setup where two bosonic modes are each coupled to their own independent, uncorrelated thermal baths (see Fig. 1) and investigate two distinct scenarios: (i) non-zero coupling between the modes, that is, $v \neq 0$ and (ii) dissipation-induced squeezing for each of the modes with $v = 0$ followed by passive optical operations [4]. In particular, previous studies [5] predicted the impossibility of steady-state entanglement in such setups, but these analyses were restricted to the Markov approximation and neglected anomalous coupling terms, which we take into account in a full non-equilibrium treatment. In contrast, our results show that entanglement, quantified by logarithmic negativity, can be robustly achieved in both scenarios. Fig. 2 shows the dependence of entanglement on the mode energy and bath temperatures, revealing the parameter regimes where steady-state entanglement is achieved. Our work provides an experimentally accessible pathway to the realization of autonomous entanglement generation

in photonic systems [6]. By demonstrating how entanglement emerges purely from system-bath interactions, we offer new tools for reservoir engineering in quantum technologies.

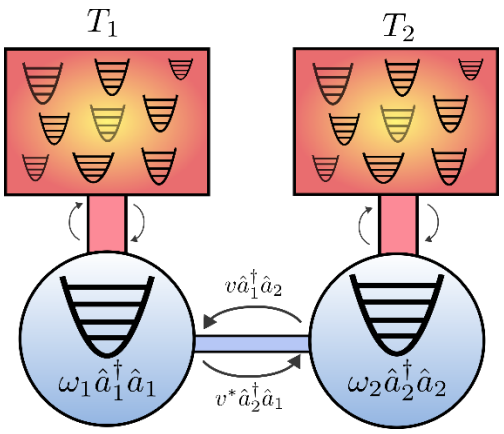

Fig. 1: Schematic representation of the investigated system

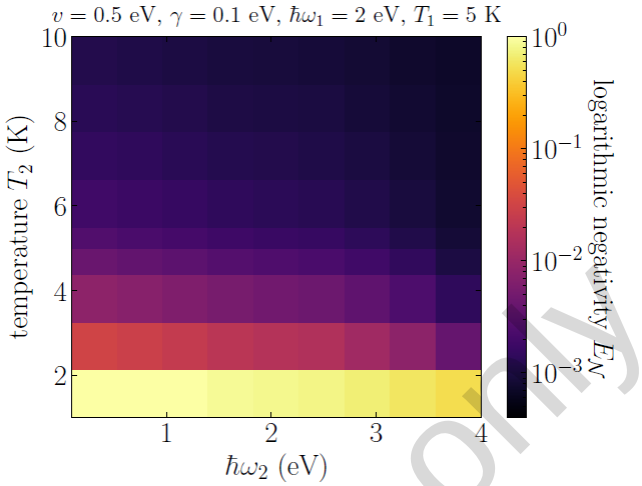

Fig. 2: Logarithmic negativity as a function of the second mode energy and its bath temperature

References

[1] Ulrich Weiss, *Quantum Dissipative Systems*, 4th Edition (World Scientific, Singapore, 2012); H.-P. Breuer and F. Petruccione, *The Theory of Open Quantum Systems* (Oxford University Press, New York, 2002).
[2] Giacomo Guarnieri, Michal Kolář, and Radim Filip, *Steady-State Coherences by Composite System-Bath Interactions*, Phys. Rev. Lett. **121**, 070401 (2018); A. Purkayastha, G. Guarnieri, M. T. Mitchison, R. Filip, and J. Goold, *Tunable phonon-induced steady-state coherence in a double-quantum-dot charge qubit*, npj Quantum Information **6**, 27 (2020).
[3] Artur Slobodeniuk, Tomáš Novotný, and Radim Filip, *Extraction of autonomous quantum coherences*, Quantum **6**, 689 (2022); *Synthesizing and multiplexing autonomous quantum coherences*, Quantum **8**, 1386 (2024).
[4] M. M. Wolf, J. Eisert, and M. B. Plenio, *Phys. Rev. Lett.* **90**, 047904 (2003).
[5] Bradley Longstaff, Michael G. Jabbour, and Jonatan Bohr Brask, *Impossibility of bosonic autonomous entanglement engines in the weak-coupling limit*, Phys. Rev. A **108**, 032209 (2023).
[6] J. Laurat et al *J. Opt. B: Quantum Semiclass. Opt.* **7** S577 (2005).

Time-dependent study of anyonic excitations in the Fractional Quantum Hall effect

T. Jonckheere[1], K. Iyer[1], F. Ronetti[1], B. Grémaud[1], T. Martin[1], J. Rech[1], E. Baudin[2], J.-M. Berroir[2], G. Fève[2], E. Frigerio[2], G. Ménard[2], B. Plaçais[2], M. Ruelle[2], A. Cavanna[3], U. Gennser[3], Y. Jin[3]

[1]Centre de Physique Théorique, Aix-Marseille Université, CNRS, 13009 Marseille France

[2] Laboratoire de Physique de l'Ecole normale supérieure, ENS, Université PSL, CNRS, Sorbonne Université, Université Paris Cité, F-75005 Paris, France

[3] Centre de Nanosciences et de Nanotechnologies, CNRS, Université Paris-Saclay, 91120 Palaiseau, France

thibaut.jonckheere -at- cpt.univ-mrs.fr

07 February 2025

Abstract: Anyons are 2D particles intermediate between fermions and bosons, characterized by a nontrivial exchange phase, yielding remarkable braiding statistics that could have important applications in quantum information schemes. The fractional quantum Hall effect (FQHE) has fundamental excitations that are anyons, and noise measurements in transport experiments have recently demonstrated their remarkable statistical properties. In this work, I will discuss how the study of current noise in a time-dependent setup in the FQHE gives unique access to the statistical properties of these anyonic excitations. I will also show how the finite width of the anyonic excitations can, in some cases, have a huge impact on the observed statistics.
Keywords: anyons, electronic transport, fractional quantum Hall effect, braiding

Introduction:
The last few years have seen tremendous developments in the study of anyonic excitations, starting with the unambiguous observation in 2020 of anyonic statistics in transport experiments in the Fractional quantum Hall effect (FQHE) [1,2]. Anyons are 2D particles intermediate between fermions and bosons, characterized by a nontrivial exchange phase, yielding remarkable braiding statistics. In the so-called *anyon collider* [1], two edge states of the FQHE, each containing a dilute stream of anyonic excitations, meet at a quantum point contact (QPC). The measurement of the current cross-correlations at the output of the QPC provides direct evidence compatible only with anyonic statistics.

Results
We consider a Hall bar in the fractional regime, equipped with a QPC where tunneling between the opposite edge states can occur (fig. 1). The edge states are treated in a bosonized Hamiltonian formalism, and calculations are done in the weak tunneling regime. When an anyonic excitation reaches the QPC, non-trivial anyonic exchange between the incoming anyon and the spontaneous anyon/anti-anyon pair at the QPC leads to *time-domain braiding*, giving a non-zero tunneling current on a long timescale (much larger than the temporal width of the incoming excitation). For a dilute stream of uncorrelated anyons, this leads to the tunneling current shown in figure 2, where the large current between the arrival of successive anyons is a direct manifestation of

anyonic statistics. This contrasts with the case of a dilute stream containing electrons rather than anyons, where the current is zero between the arrival of successive electrons, as shown by the inset of figure 2.

As the measurement of time-dependent current on such a rapid timescale is very difficult to achieve, we show that the same physical information about the time dependence can be obtained by a noise measurement when sending periodic voltage pulses containing a fractional charge e^*. The pulses are sent to both inputs of the QPC, with a controllable time shift δt, similar to the Hong-Ou-Mandel setup in optics (fig. 1). The current correlations at the output of the QPC show a typical HOM dip, with a minimum for $\delta t = 0$. However, the width of the dip shows a dramatic change depending on the charge of the incoming pulses. When the pulses contain a full electron charge, there is no anyonic braiding at the QPC, and the dip width is directly related to the width of the incoming pulses. However, when the pulses contain a fractional charge, the width of the dip is fixed by the much longer timescale due to non-trivial anyonic braiding, leading to a much wider HOM dip (fig. 2) [3]. This method to measure the statistical properties of anyonic braiding has been recently confirmed experimentally for the FQHE [4], leading to a precise measurement of the statistical angle of anyonic braiding for the FQHE at filling factor $1/3$.

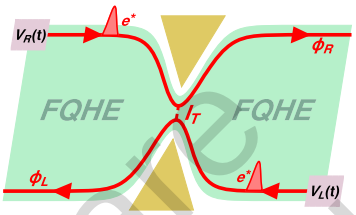

Figure 1: The setup. A Hall bar in the FQHE, equipped with a quantum point contact where tunneling between the opposites edge states occurs. Voltage pulses containing a fractional charge e^* are sent with a controllable time delay, and the current correlations are measured at the output as a function of the time delay.

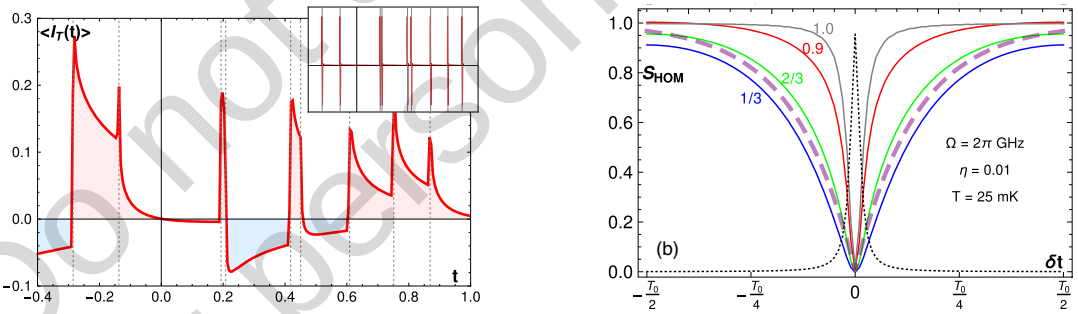

Figure 2: (left) Tunneling current at the quantum point contact (QPC) as a function of time when a dilute stream of anyon is incoming on the QPC. The arrival time of the anyons at the QPC are shown as the dashed lines. Unit of time is the thermal time $\hbar/k_BT$. The inset shows the case of incoming electrons. (right) Current correlations S_{HOM} as a function of the time delay δt when sending periodically pulses with a charge qe. The different curves correspond to different values of q. The black dotted line shows the shape of the incoming pulses.

References

1. H. Bartolomei, M. Kumar, R. Bisognin, A. Marguerite, J.-M. Berroir, E. Bocquillon, B. Plaçais, A. Cavanna, Q. Dong, U. Gennser et al., Science **368**, 173 (2020).
2. J. Nakamura, S. Liang, G. C. Gardner, and M. J. Manfra, Nat. Phys. **16**, 931 (2020)
3. T. Jonckheere, J. Rech, B. Grémaud, and T. Martin, Phys. Rev. Lett. **130**, 186203 (2023); K. Iyer, F. Ronetti, B. Grémaud, T. Martin, J. Rech, and T. Jonckheere, Phys. Rev. Lett. **132**, 216601 (2024)
4. M. Ruelle, E. Frigerio, E. Baudin, J.-M. Berroir, B. Plaçais, B. Grémaud, T. Jonckheere, T. Martin, J. Rech, A. Cavanna, U. Gennser, Y. Jin, G. Ménard, and G. Fève, arXiv:2409.08685, accepted for publication in Science

ΔT-noise in hybrid superconducting nanodevices.

L. Pierattelli[1], F. Taddei[1], A. Braggio[1]

[1] NEST, Istituto Nanoscienze-CNR and Scuola Normale Superiore, Piazza San Silvestro 12, I-56127 Pisa, Italy

leonardo.pierattelli@sns.it,fabio.taddei@nano.cnr.it,alessandro.braggio@nano.cnr.it

February 7, 2025

Abstract: We study the behavior of current correlations in hybrid normal-superconducting mesoscopic scattering systems in the presence of temperature biases between the terminals. Using the standard scattering theory of transport, we compute the noise expressions at zero frequency, and we identify two distinct contributions therein, according to their dependence on scattering matrices, which we call background and excess noise. We find unexpectedly that the background noise of self-correlations in hybrid systems, in the presence of a thermal gradient, depends on a quantity strictly related to heat conductance, not the electrical one. On the other hand, excess noise shows expected additional interference terms due to current partitioning between normal and Andreev reflection channels. Then, we apply the results to two physical examples, an NSN device and a Quantum Hall bar at $\nu = 2$ with spin-resolved edge states. We focus primarily on the properties of what we call "thermal" shot noise, i.e., the excess noise behavior in the presence of significant temperature biases, contrasting it to the "electrical" shot noise, i.e., the excess noise at large voltage biases. These results show again the difference in nature between electrically- and thermally-induced charge fluctuations, which can be uniquely highlighted by the simultaneous presence of superconductors in the system. These results may be relevant for the field of quantum technologies both theoretically and applicately.
Keywords: Quantum noise, Hybrid superconducting systems, Temperature biases

Introduction: Current correlations are a valuable source of information used to probe various effects and observables in electronic systems, such as temperature, carriers' charge, and statistics [1,2]. Thanks to recent advances in the fabrication of quantum devices, the study of noise properties is becoming increasingly relevant. It will likely enable new and promising technologies, for example, using interferometric effects in Quantum Hall systems [3] or the features of quasiparticles in normal-superconducting hybrid systems [4]. Historically, the most interest has been devoted to studying noise in electrically biased systems [5]. However, it has been shown recently that relevant information can also be obtained by applying thermal biases [6], for instance, regarding the presence of interactions in scattering systems [7]. We then devote ourselves to thoroughly reviewing the noise properties of thermally biased hybrid systems, contrasting them with those of electrically biased cases. We find that hybrid systems possess unique properties that emerge thanks to the presence of superconductors and that thermally induced fluctuations have distinctly different properties from electrically induced ones.

Theory and Methods

We use Landauer-Büttiker's theory of electron transport to compute all our relevant quantities. Being $s_{ij}^{\alpha\beta}(E)$ the scattering matrix, by rederiving the standard formulae for currents and correlations, we identify two prominent transmission functions $\ell_{ik}^{\pm}(E)$:

$$\ell_{ik}^{\pm}(E) = N_i\delta_{ik} - \mathrm{Tr}[s_{ik}^{ee\dagger}(E)s_{ik}^{ee}(E)] \pm \mathrm{Tr}[s_{ik}^{he\dagger}(E)s_{ik}^{he}(E)], \tag{1}$$

and we notice that the ℓ^+ enter the definition of the charge conductance, while the ℓ^- of the heat one. Then we rewrite the expression of the charge current correlations at zero frequency $S_{ij}(0)$ dividing them in two contributions, i.e., $S_{ij}(0) = \bar{S}_{ij} + \tilde{S}_{ij}$. We call the first, $\bar{S}_{ij}$, *background noise*, which is the only surviving term in linear regime ($F_i^e(E) \equiv 2f_i^e(E)\left[1 - f_i^e(E)\right]$):

$$\bar{S}_{ij} = G_0 \int dE \left[F_j^e(E)\ell_{ij}^+(E) + F_i^e(E)\ell_{ji}^+(E) - \delta_{ij} \sum_k F_k^e(E)\ell_{ik}^-(E) \right], \tag{2}$$

and we notice that, unlike in normal systems, self-correlations ($i = j$) also depend on the heat conductance-related quantities ℓ^-, instead of just ℓ^+, and that such dependence *only* emerges when temperature biases are applied. We call instead the second term $\tilde{S}_{ij}$ of the correlations *excess noise*, which is of higher order in the biases and describes the noise due to current partitioning processes, which in hybrid systems can also occur between transport channels of quasiparticles of different type due to Andreev processes.

Finally, we apply the above results to two specific physical systems, an NSN device and a Quantum Hall bar in $\nu = 2$ regime with spin-resolved edge states proximitized with a superconducting insertion along their path. We compute their excess noises when large voltage or temperature biases are applied, identifying two regimes that we call for clarity: "electrical" and "thermal" shot limits. For example, we report the NSN excess noises in the two limits in the energy-independent scattering matrix case. In the electrical shot limit, the $\tilde{S}_{22}$ and $\tilde{S}_{12}$ excess noises read:

$$\frac{\tilde{S}_{22}}{2G_0|e\Delta V|} \approx \left[-\ell_{21}^- - \ell_{21}^{+2}\right]; \quad \frac{\tilde{S}_{12}}{2G_0|e\Delta V|} \approx \left[\left(1 - \ell_{11}^+\right)\ell_{21}^+\right], \tag{3}$$

Results Our first main result is to derive the first-order corrections to the Johnson-Nyquist noise in hybrid systems, which are proportional to the heat conductance instead of the electrical one, as one naively expects from applying the fluctuation-dissipation theorem. Then, by investigating the various shot limits, we show that electrically- and thermally-induced charge current fluctuations behave very differently, but such differences strongly emerge in the presence of superconductors. When voltage biases are applied, the charge of the carriers is probed. In contrast, when temperature biases are prominent, we can probe quasiparticles' partitioning effects irrespective of their charge, and this can also give rise to additional interference terms in the cross-correlations' excess noise. These results are crucial to superconducting quantum technologies, identifying new noise channels, minimizing the sensitivities of quantum sensors, and optimizing superconducting quantum circuit performances.

References

1. R. Landauer, "The noise is the signal", Nature 392, 1998, pp. 658.
2. R. de Picciotto et al., "Direct observation of a fractional charge", Nature 389, 1997, pp. 162.
3. Y. Ji et al., "An electronic Mach–Zehnder interferometer", Nature 422, 2003, pp. 415.
4. C. Beenakker, "Annihilation of Colliding Bogoliubov Quasiparticles Reveals their Majorana Nature", Phys. Rev. Lett. 112, 2014, pp. 070604.
5. W. Schottky, "Über spontane Stromschwankungen in verschiedenen Elektrizitätsleitern", Ann. Phys. 362, 1918, pp. 541.
6. O. S. Lumbroso et al., "Electronic noise due to temperature differences in atomic-scale junctions", Nature 562, 2018, pp. 240.
7. A. Braggio et al., "Nonlocal thermoelectric detection of interaction and correlations in edge states", Phys. Rev. Res. 6, 2024, pp. L012049

Revisting minimal excitations in non-linear conductors

Inès Safi
Laboratoire de Physique des Solides, CNRS UMR 5802-University Paris-Saclay, France
ines.safi@polytechnique.org

Abstract: We revisit minimal excitations in nonlinear conductors by analyzing photo-assisted shot noise (PASN) under AC driving within the unifying non-equilibrium perturbative (UNEP) theory. For arbitrary nonequilibrium distributions—arising, e.g., from non-Gaussian reservoirs or temperature gradients—we show that the PASN lower bound is set by the photo-assisted current, not the DC noise, as Levitov's theorem assumes for linear conductors. For a thermal distribution, Poissonian PASN emerges only for Lorentzian pulses at zero temperature. We explicitly demonstrate Levitov's theorem breakdown and the emergence of super-Poissonian PASN in both superconductor–insulator–superconductor junctions and fractional quantum Hall (FQHE) quantum point contacts modeled as Tomonaga-Luttinger liquids (TLLs).
In the TLL case, equilibrium noise persists when the DC voltage matches the AC frequency, requiring finite temperature to maintain perturbative validity—rendering PASN super-Poissonian even with Lorentzian pulses. This shows the inadequacy of the zero-temperature limit often assumed in prior theories, including Wen's. Our results are relevant for coherent conductors, Josephson and phase-slip junctions (Shapiro steps), strongly coupled to Ohmic environments.
Keywords: nonequilibrium electron transport, photo-assisted noise, minimal excitations, Fractional Quantum Hall Effect (FQHE)

Introduction: Injection and manipulation of controlled quantum electronic or photonic states are central to two rapidly growing and fascinating fields: electronic quantum optics (EQO) and the quantum electrodynamics (QED) of mesoscopic circuits. Quantum Hall systems provide an ideal platform for EQO, where Coulomb interactions are key to the emergence of FQHE with fractional charges [1] and statistics [2], and have been addressed via a plasmon-scattering approach [3], foundational to nonequilibrium bosonization. EQO has been advanced by key theoretical and experimental breakthroughs [4]. Single-electron sources have used mesoscopic capacitors [4] or minimal excitations generated by Lorentzian pulses [5], enabling injection into interferometers (Hanbury-Brown–Twiss, Hong-Ou-Mandel), with applications to charge fractionalization, quantum statistics [5], and tomography.
Mesoscopic QED explores radiation-matter interactions via artificial atoms (e.g., Josephson junctions), where the environment acts as a photonic bath. These lead to dynamical Coulomb blockade effects that simulate 1D correlated conductors [6]. Photon and electron statistics, and squeezed states, have been studied via finite-frequency noise under AC drive [9], with Lorentzian pulses providing a favorable profile [10]. These approaches, however, often assume independent electrons. The UNEP theory offers a unified framework for strongly correlated, time-dependent transport systems in both EQO and QED.

The Unifying Non-Equilibrium Perturbative (UNEP) theory: UNEP applies to systems with Hamiltonian $\mathcal{H}(t) = \mathcal{H}_0 + e^{-i\omega_J t} p(t) A + e^{i\omega_J t} p^*(t) A^\dagger$, where $\omega_J = e^* V/\hbar$ is a Josephson-type drive frequency, and $p(t)$ is an arbitrary complex function [7]. In Josephson junctions $e^* = 2e$,

while for FQHE at $\nu = 1/(2k+1)$, $e^* = \nu e$. The theory allows for a nonequilibrium initial state ρ_{neq} commuting with $\mathcal{H}_0$, without assuming a bipartite structure. The current operator $I(t) = -ie^*/\hbar \left(e^{-i\omega_J t} p(t)\ A - e^{i\omega_J t} p^*(t) A^\dagger\right)$ can describe charge, Josephson, or spin transport. Its average and fluctuations follow universal relations and are solely determined by the DC current $I(\omega_J)$ and noise $S(\omega_J)$. For periodic $p(t)$ with frequency ω_{ph}, we have [7]: $O_{ph}(\omega_J) = \sum_{l=-\infty}^{+\infty} P_l O(\omega_J + l\omega_{ph})$, with $O = I, S$, and $P_l = |p_l|^2$, where $p_l = \omega_{ph} \int_0^{2\pi/\omega_{ph}} e^{il\omega_{ph}t} p(t) dt/2\pi$. When $|p(t)| = 1$, P_l gives the probability of exchanging l photons. This generalizes Tien-Gordon theory to correlated many-body systems. For non-periodic $p(t)$, the sum becomes an integral, analogous to dynamical Coulomb blockade [7].
UNEP provides robust methods to measure fractional charge via ω_J, without relying on TLL models [7] that have been implemented experimentally [11].

Revisiting minimal excitations: For any non-equilibrium ρ_{neq}, the DC noise satisfies [7, 8]: $S(\omega_J) \geq e^* |I(\omega_J)|$ which leads to the universal super-Poissonian PASN [7]:

$$S_{ph}(\omega_J) \geq e^* |I_{ph}(\omega_J)|. \tag{1}$$

This also holds for non-periodic $p(t)$. For a thermal initial state $\rho_{eq} \propto e^{-\beta \mathcal{H}_0}$, this provides an alternative to Levitov's theorem [5], which states $S_{ph}(\omega_J) \geq S(\omega_J)$ under linear current and periodic $p(t) = e^{-i\varphi(t)}$. We have shown its breakdown in superconductor-insulator-superconductor junctions [7] and in FQHE QPCs, where PASN instead follows Eq. (1). While Lorentzian pulses yield Poissonian PASN at $T = 0$, this limit fails in TLL models: equilibrium contributions persist even in the quantum regime [8], and the Poissonian limit is never attained.

Perspectives: UNEP offers universal fluctuation relations for finite-frequency PASN [7], relevant for analyzing squeezing. Optimizing $p(t)$ and selecting appropriate correlated models via $I(\omega_J)$ can guide the design of minimal excitations in quantum devices.

References

[1] L. Saminadayar *et al*, Phys. Rev. Lett. **79**, 2526 (1997).

[2] H. Bartolomei *et al*, Science **368**, 173 (2020).

[3] I. Safi, Eur. Phys. J. B **12**, 451 (1999). H. Kamata *et al*, Nat. Nanotechnol. **9**, 177 (2014). I.P. Levkivskyi and E.V. Sukhorukov, Phys. Rev. Lett. **103**, 036801 (2009).

[4] G. Fève *et al*, Science **316**, 1169 (2007). C. Grenier *et al*, Mod. Phys. Lett. B **25**, 1053–1073 (2011).

[5] I. Klich and L. Levitov, Phys. Rev. Lett. **102**, 100502 (2009). J. Dubois *et al*, Nature **502**, 659 (2013).

[6] I. Safi and H. Saleur, Phys. Rev. Lett. **93**, 126602 (2004).

[7] I. Safi, arxiv:1401.5950. Phys. Rev. B **99**, 045101 (2019); **102**, 041113 (2020); **106**, 205130 (2022).

[8] Imen Taktak and Inès Safi, arxiv:2402.07622 (2025).

[9] G. Gasse, C. Lupien, and B. Reulet, Phys. Rev. Lett. **111**, 136601 (2013).

[10] C. Mora, C. Altimiras, P. Joyez, and F. Portier, Phys. Rev. B **95**, 125311 (2017).

[11] M. Kapfer *et al*, Science **363**, 846 (2019). R. Bisognin *et al*, Nat. Comm. **10**, 1708 (2019).

Quantum Noise-assisted phase-flip rate in a biased parametric oscillator

Wolfgang Belzig[1], Daniel Boness[1], Mark Dykman[2]

[1]Department of Physics, University of Konstanz, 78464 Konstanz, Germany
[2]Michigan State University, East Lansing, MI 48824, USA
wolfgang.belzig@uni-konstanz.de

Abstract: A parametrically driven oscillator has two stable vibrational states at half the modulation frequency. The states have opposite phase and equal amplitudes. An extra drive at half the modulation frequency provides an effective bias that lifts the state symmetry. Quantum fluctuations lead to switching between the states, i.e., to phase-flip transitions. We develop a semiclassical approach that allows us to find the dependence of the switching rates on the amplitude of the bias and the parameters of the modulating field. We find that the rate of switching from a "shallow" state can become anomalously small at certain parameter values, leading to an efficient localization in this state. This is a consequence of the change of the topology of the oscillator phase trajectories. The results pave the way for implementing nonreciprocal quantum Ising systems based on parametric oscillators.

Keywords: Quantum noise, Parametric Oscillators, Quantum Switching

References:

M. Marthaler and M. I. Dykman, Switching via quantum activation: A parametrically modulated oscillator, Phys. Rev. A 73, 042108 (2006); Quantum interference in the classically forbidden region: A parametric oscillator, 76, 010102R (2007).

D. K. J. Boneß., W. Belzig, and M. I. Dykman, Resonant force-induced symmetry breaking in a quantum parametric oscillator, Physical Review Research 6, 033240 (2024).

Daniel K. J. Boneß, Wolfgang Belzig, Mark I. Dykman, Zero-temperature phase-flip rate in a biased parametric oscillator, arXiv:2501.07562

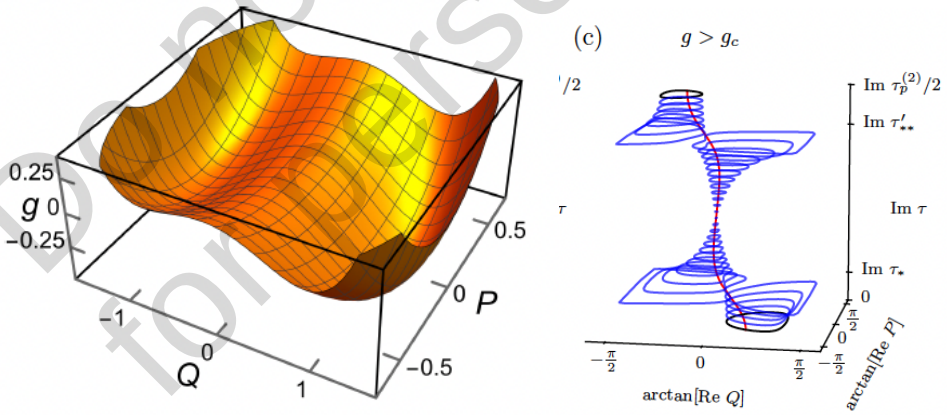

Left: Pseudo-energy landscape in phase space with broken symmetry between the phase states. Right: Switching trajectory

This page is intentionally left blank

The fine-structure constant as equilibrium photon-number shot-noise of a black-body

L. Varani[1], F. Intini[2], L. Reggiani[3]

[1]Institut d'Electronique et des Systèmes, University of Montpellier, Montpellier, France

[2]Department of Engineering "Enzo Ferrari", University of Modena and Reggio Emilia, Modena, Italy

[3]Department of Mathematics and Physics "Ennio de Giorgi", University of Salento, Lecce, Italy

luca.varani@umontpellier.fr

Abstract: We present a new exact statistical formulation of the inverse of the fine-structure constant, $1/\alpha$, based on Planck's law for a photon gas in a black-body. The authors demonstrate a relationship between $1/\alpha$ and the statistical properties of the photon gas, specifically the variance and the average value of the photon number. The result is obtained through an analysis that connects the fine-structure constant to thermodynamic parameters of the black body, such as temperature and volume. The accuracy of the model is limited only by the precision of the fundamental physical constants used. Finally, the article discusses the physical interpretation of the fine-structure constant in terms of the statistical properties of a quantum-relativistic system.

Keywords: fine-structure constant, black-body, Planck's law

Introduction: The fine-structure constant is considered one of the most important physical constants due to its relevance in numerous aspects of modern physics and its fundamental properties [1]. It is accepted that this dimensionless constant quantifies the strength of the electromagnetic interaction between elementary charged particles but, despite its importance, the reason why the fine-structure constant has this specific value and its physical meaning are not yet well understood [2].

Indeed, Michelson and Morley's 1887 experiments highlighted the fine structure of a single line in the emission spectrum of the hydrogen atom [3] and later on Sommerfeld's work in 1916 introduced the fine-structure constant, α, a dimensionless quantity, to improve the atomic model of hydrogen [4].

The inverse of the fine-structure constant, $1/\alpha$, can be expressed as a combination of four fundamental physical constants: the elementary charge e, Planck's constant h, the vacuum permittivity ϵ_0, and the speed of light in vacuum c. The relationship is:

$$\frac{1}{\alpha} = \frac{2h\epsilon_0 c}{e^2} \approx 137 \tag{1}$$

At present, the numerical value of the inverse of the fine-structure constant is known with an experimental accuracy of 12 digits as $\frac{1}{\alpha} = 137.035999177$ [5].

Theory Being dimensionless, $\frac{1}{\alpha}$ can be interpreted as the ratio between two physical quantities, possibly coupled to some numbers, representing different theoretical models but having the same physical dimensions. However, to the best of our knowledge, the fine-structure constant has never been related to the statistical properties of a photon gas.

In this communication we propose an exact statistical expression of the inverse of the fine-structure constant, $\frac{1}{\alpha}$, as the variance of an instantaneous number of photons pertaining to a black-body of given cubic volume $V_{\frac{1}{\alpha}}$ of side $L_{\frac{1}{\alpha}}$ and temperature $T_{\frac{1}{\alpha}}$ described by Planck's distribution law. In particular, if the side and temperature of the black-body are linked as

$$L_{\frac{1}{\alpha}} T_{\frac{1}{\alpha}} = 1.702677 \text{ cm K} \tag{2}$$

we find

$$\frac{1}{\alpha} = \overline{\delta N^2}_{\frac{1}{\alpha}} = \gamma \overline{\delta N}_{\frac{1}{\alpha}} \approx 137.0360 \tag{3}$$

with $\overline{\delta N^2}_{\frac{1}{\alpha}}$ and $\overline{\delta N}_{\frac{1}{\alpha}}$, respectively the variance and the average values of the photon number inside the given black-body for the given experimental values of $\frac{1}{\alpha} = 137.0360$.
In eq. (3) the Fano factor γ, defined as the variance to mean ratio of a counting process, can be expressed in terms of the Riemann function ζ as $\gamma = \zeta(2)/\zeta(3) \approx 1.368433$. This value of the Fano Factor associated with the Planck's law is compatible with the fine structure constant to the best of its given accuracy that has been limited here to 7 digits due to the known accuracy of the Boltzmann's constant.
It is noteworthy that, analogously to the well-known shot-noise associated with the discreteness of the electric charge, the concept of a spectral density of particles number fluctuations S describing the shot-noise associated with fluctuations of the photon-number can be introduced as:

$$S = \frac{4\overline{\delta N^2}}{\tau} \tag{4}$$

with $\tau = L/c$ the photon transit-time between opposite walls. This spectral density can be related directly to the fine-structure constant since, by choosing the variance of photon number as $\overline{\delta N^2}_{\frac{1}{\alpha}}$, it satisfies the relation:

$$\frac{\tau}{4} S_{\frac{1}{\alpha}} = \frac{1}{\alpha}. \tag{5}$$

References

1. P. Kundu, Sommerfeld fine structure constant and its physical interpretation, Annales de la Fondation Louis de Broglie, vol. 18, 1993, p. 391
2. R. P. Feynman, QED: The Strange Theory of Light and Matter. Princeton University Press, 1985, p. 129
3. A. Michelson and E. Morley, On a method of making the wave-length of sodium light the actual practical standard of length, American Journal of Science, vol. 34, 1887, p. 427
4. A. Sommerfeld, Zur Quantentheorie der Spek- trallinien, Annalen der Physik, vol. 51, 1916, pp. 1-52
5. P. J. Mohr, D. B. Newell, B. N. Taylor and E. Tiesinga 2022 CODATA Value: fine-structure constant, The NIST Reference on Constants, Units, and Uncertainty. DOI: 10.48550/arXiv.2409.03787

Simulation of Fluctuations with *1/f* Spectrum

Z. Kolodiy

Lviv Polytechnic National University, Institute of Computer Technologies, Automatics and Metrology
Lviv, Ukraine
kzenoviy@gmail.com

Abstract: The results of computer modeling of the chaotic motion of elements in balanced and unbalanced systems are presented, which shows that equilibrium fluctuations (white noise) are inherent in a balanced system. In an unbalanced system, there are equilibrium and non-equilibrium fluctuations, and non-equilibrium fluctuations appear at low frequencies and are proportional to *1/f*. It is shown that in general, the level of the *1/f* component of fluctuations can be reduced by increasing the balance of the system under study. A formula for approximating the energy spectrum of fluctuations is presented, the parameters of which are the level of equilibrium fluctuations (thermal noise for electronic elements) and the degree of deviation from the balanced state of the system under study, which is expressed in terms of the relaxation time. Therefore, the proposed formula can be used to approximate fluctuations of type *1/f* in any real system: electrical fluctuations, fluctuations in biology, fluctuations in geophysics, etc. The approximation formula allows us to estimate the level of fluctuations in the low-frequency range.

Keywords: fluctuations, energy spectrum, flicker noise, relaxation time.

Introduction. The purpose of this work is to analyze the results of modeling the chaotic motion of elements in models of balanced and unbalanced systems to test the hypothesis that *1/f* type fluctuations are a consequence of the internal dynamics of an unbalanced system associated with the chaotic motion of its elements.

Conducted research and results. Fig. 1a shows the appearance of the computer model [1] and the time series of measurement results Δn (Fig. 1b).

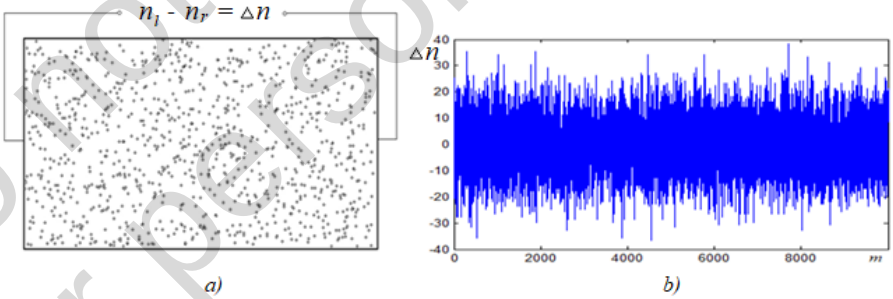

Fig.1. Appearance of the computer model (a) and the time series of measurement results (b)

Fig. 2 shows the appearance of the models of equilibrium M0 and stationary non-equilibrium systems M1, M2 and the corresponding histograms of measurement results Δn and their energy spectrum *W(f)*.

A common feature of the energy spectra shown in Fig. 2 is their practically identical value at frequencies above 30 Hz and is equal to the value of the energy spectrum W_0 for the equilibrium system model M0:

$$W_1(f \geq 30) = W_2(f \geq 30) = W_0 = const.$$

The energy spectra for models M1, and M2 (Fig. 2) can be represented as the sum:

$$W_n(f) = W_0 + W_n'(f), \quad (1)$$

where the value of $W_n'(f)$ is noticeable only at low frequencies.

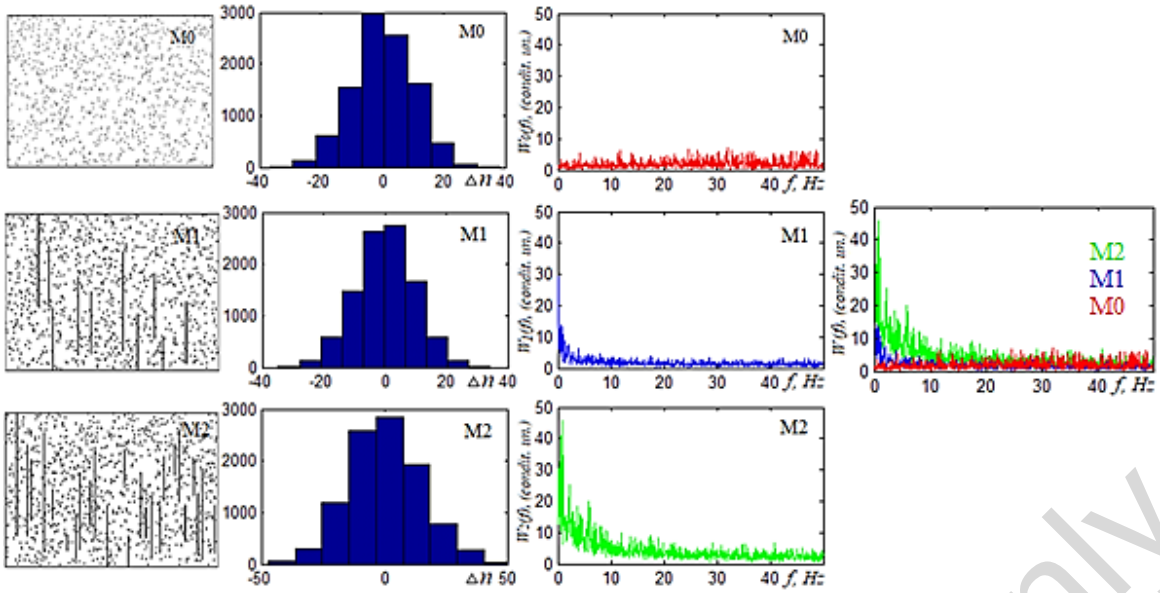

Fig.2. View, histograms and energy spectrum of equilibrium M0 and stationary non-equilibrium systems M1 and M2.

The increase in the level of fluctuations at lower frequencies in models M1 and M2 can be interpreted as an increase in the probability of non-equilibrium fluctuations with decreasing frequency $P(f \to f_L) = e^{-f \cdot \alpha}$, where α is a coefficient that takes into account the state of the system.

Formula (1) can be represented as:

$$W_n(f) - W_n'(f) = W_0, \quad (2)$$

where $W_n'(f) = W_n(f) \cdot P(f \to f_L) = W_n(f) \cdot e^{-f \cdot \alpha}$ – the fraction of non-equilibrium fluctuations in the total fluctuations of the non-equilibrium system. From (2):

$$W_n(f) - W_n(f) \cdot e^{-f \cdot \alpha} = W_n(f)(1 - e^{-f \cdot \alpha}) = W_n(f) \cdot P(f) = W_0, \quad (3)$$

where *P(f)* - is the probability of fluctuations in the entire frequency range for non-equilibrium systems.

The dependence on the features of the non-equilibrium system can be reflected by some parameter that would be universal for the systems under study, regardless of their nature: electrical, chemical, etc. Such a parameter can be the relaxation time τ. Therefore, the coefficient α, which takes into account the state of the system: α = τ and formula (3) can be represented as:

$$W_n(f) = W(f) = \frac{W_0}{P(f)} = \frac{W_0}{1 - e^{-f \cdot \tau}} = \frac{e^{f \cdot \tau}}{e^{f \cdot \tau} - 1} \cdot W_0 \quad (4)$$

From (4) at $0 < \tau < \infty$ at medium and high frequencies ($f \cdot \tau \gg 1$) the energy spectrum $W(f) \to W_0$. At low frequencies, formula (4) takes the form:

a) at $f \cdot \tau \leq 1$: $W(f) \approx \left[\frac{1}{f \cdot \tau + \frac{1}{2} f^2 \cdot \tau^2} + \frac{1}{1 + \frac{1}{2} f \cdot \tau} + \frac{f \cdot \tau}{2 \cdot \left(1 + \frac{1}{2} f \cdot \tau\right)}\right] \cdot W_0$

b) at $f \cdot \tau \ll 1$: $W(f) \approx \left[1 + \frac{1}{f} \cdot \frac{1}{\tau}\right] \cdot W_0 = W_0 + \frac{1}{f} \cdot \frac{W_0}{\tau}$, a flicker component appears in the fluctuation spectrum: $\frac{1}{f} \cdot \frac{W_0}{\tau}$.

From (4) the value of τ corresponds to the time interval during which *W(f)* decreases to the level of 1.58 W_0. It can be determined from the experimentally determined energy spectrum of fluctuations of the studied system: $\tau = \frac{1}{f_\tau}$, де f_τ – частота, на якій $W(f_\tau) = 1.58\ W_0$.

References

[1] K. Przystupa, Z. Kolodiy, S. Yatsyshyn, et al., "Standard deviation in the simulation of statistical measurements", Metrol. Meas. Syst., vol. 30, No. 1, 2023, pp. 17-30, DOI: 10.24425/mms.2023.144403.

Thermal Noise Communication: Low Power or Hot Air?

C. Chamon[1]

[1]Department of Electrical and Computer Engineering, Virginia Tech, Blacksburg, VA, USA
ccgarcia@vt.edu

Abstract: The Kirchhoff-Law-Johnson-Noise (KLJN) secure key exchange scheme leverages statistical physics to enable secure communication with zero average power flow in a wired channel. While the original KLJN scheme requires significant power for operation, a recent wireless modification proposed by Basar claims a "low power" implementation. This paper critically examines and refutes this claim. We demonstrate that the additional components inherent in Basar's wireless adaptation substantially increase power consumption, rendering the "low power" assertion inaccurate. Furthermore, we clarify that the security claims of the original KLJN scheme do not directly translate to this wireless adaptation, highlighting potential vulnerabilities. Our analysis underscores the inherent power requirements of KLJN-based schemes and challenges the feasibility of low-power implementations in wireless contexts.

Keywords: unconditional security, wireless modification, power consumption

Introduction The Kirchhoff-Law-Johnson-Noise (KLJN) secure key exchange scheme, introduced by Kish in 2005, utilizes statistical physics principles to achieve secure communication over a wired channel with zero average power flow [1-3]. The core of the KLJN scheme is shown in Fig. 1. This system employs resistors, switches, and noise generators to create a secure key exchange mechanism that claims unconditional security. Recently, Basar proposed a wireless modification of the KLJN scheme, shown in Fig. 2, asserting a "low power" implementation [4]. However, this claim is misleading and requires critical examination.

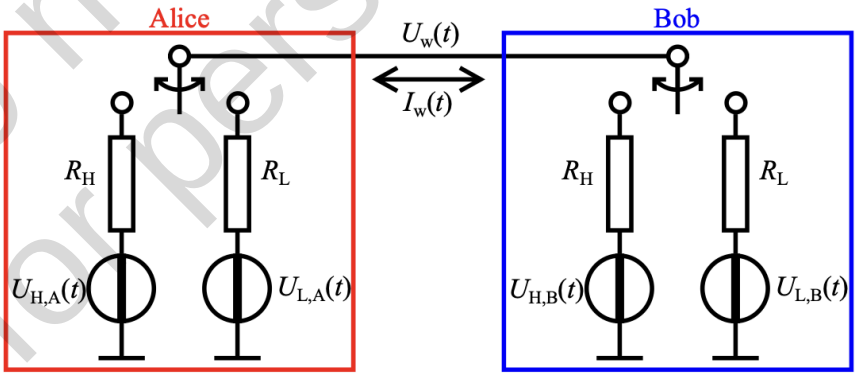

Fig. 1: The core of the KLJN scheme.

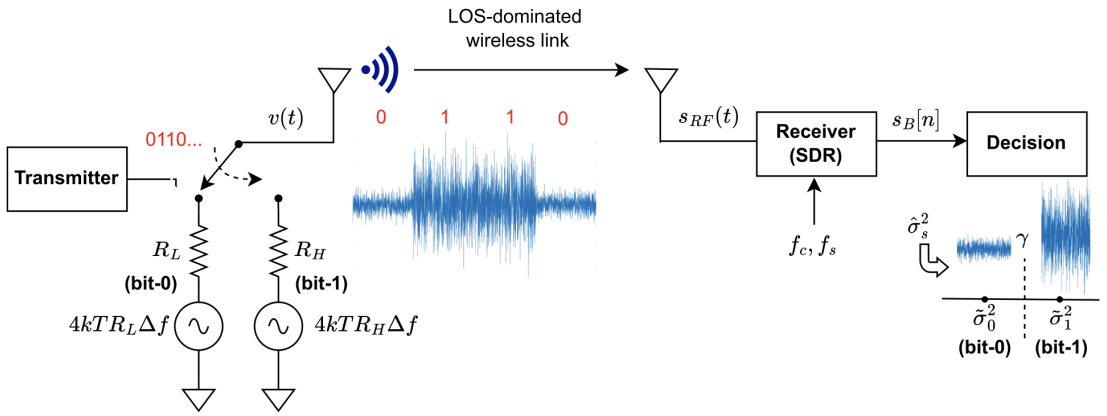

Fig. 2: The core of the proposed TherMod scheme.

Refutation While the KLJN scheme indeed maintains zero average power flow in the information channel, it still requires significant power for operation. The system necessitates random number generators to produce the noise, switches to alternate between resistor values, and measuring devices to detect the voltage and current fluctuations. These components consume power independently of the information channel's net energy transfer. Furthermore, Basar's wireless adaptation introduces additional components that further increase power consumption. The transition from a wired to a wireless medium requires signal amplification and more sophisticated measurement techniques, which inherently demand more energy.

Conclusion It is crucial to note that the security guarantees of the original KLJN scheme do not directly translate to this wireless adaptation. The wireless environment introduces new potential vulnerabilities that need careful consideration. While the KLJN scheme offers an innovative approach to secure key exchange, claims of "low power" implementations, especially in wireless contexts, should be approached with skepticism. The inherent power requirements of the system's components make truly low-power realizations challenging, if not infeasible.

References

[1] C. Chamon and L.B. Kish. "Perspective–On the Thermodynamics of Perfect Unconditional Security", Applied Physics Letters, vol. 119, 2021, pp. 010501.
[2] L. B. Kish, "Totally secure classical communication utilizing Johnson (-like) noise and Kirchhoff's law", Physics Letters A, 2006.
[3] L. B. Kish, "Enhanced secure key exchange system based on the Johnson(-like) noise", Fluctuation and Noise Letters, 2007.
[4] E. Basar, "Communication by Means of Thermal Noise: Toward Networks With Extremely Low Power Consumption", IEEE Communications, 2022.

Duality on the Thermodynamics of the Kirchhoff-Law-Johnson-Noise (KLJN) Secure Key Exchange Scheme

S. A. Flanery[1], A. Trapani, C. Chamon[2], L. Nazhandali[2]

[1]Department of Electrical and Computer Engineering,
Texas A&M University, College Station, TX, USA
sflanery@tamu.edu
[2]Department of Electrical and Computer Engineering, Virginia Tech, Blacksburg, VA, USA
{ansont20, ccgarcia, leyla}@vt.edu

Abstract: This study investigates a duality approach to information leak detection in the generalized Kirchhoff-Law-Johnson-Noise (KLJN) secure key exchange scheme. While previous work by Chamon and Kish sampled voltages at zero-current instances, this research explores sampling currents at zero-voltage crossings. The objective is to determine if this dual approach can reveal information leaks in non-equilibrium KLJN systems. Results indicate that the duality method successfully detects information leaks, further supporting the necessity of thermal equilibrium for unconditional security in KLJN systems.

Keywords: unconditional security, thermal equilibrium, duality

Introduction The KLJN secure key exchange scheme, based on classical statistical physics, has been proposed as an alternative to quantum key distribution for unconditionally secure communication [1-3]. The core of the KLJN scheme is shown in Fig. 1. Recent modifications to the original KLJN scheme suggested that perfect security might be achievable in non-equilibrium conditions [1]. However, Chamon and Kish demonstrated an information leak in this generalized scheme by sampling voltages at zero-current crossings [2]. This study aims to explore a dual approach to their method, potentially providing additional insights into the security vulnerabilities of non-equilibrium KLJN systems.

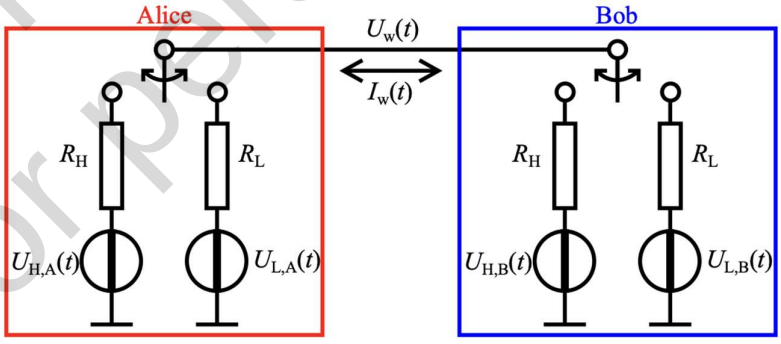

Fig. 1: The core of the KLJN scheme.

Methodology The duality approach involves the following steps:

1. Set up a simulated non-equilibrium KLJN system based on the generalized scheme.
2. Implement a sampling mechanism to capture channel current values at instances when the channel voltage crosses zero.

3. Square the sampled current values and calculate the mean (zero-crossing mean-square current).
4. Analyze the resulting data to detect any patterns or information leaks.
5. Compare the results with those obtained by Chamon and Kish's voltage sampling method.

Results As shown in Table 1, the duality approach of sampling currents at zero-voltage crossings revealed:

1. A detectable information leak in the non-equilibrium KLJN system, similar to the findings of Chamon and Kish [2].
2. The zero-crossing mean-square current showed statistically significant differences between different resistor configurations, indicating a vulnerability to eavesdropping attacks.
3. The magnitude of the information leak was comparable to that observed in the voltage sampling method, suggesting that both approaches are equally effective in detecting security vulnerabilities.
4. When thermal equilibrium was restored, the information leak disappeared, confirming the importance of equilibrium conditions for unconditional security [2, 3].

Table 1: Results from the duality of the zero-crossing attack.

Scheme	bit	R_A [Ω]	R_B [Ω]	P_{AB} [10^{-3} W]	p	σ_p
KLJN	LH	1k	10k	0	0.5002	0.0091
	HL	10k	1k			
VMG-KLJN	LH	100	16.7k	0.026	0.5885	0.0022
	HL	16.7k	278			
	LH	278	278	0.471	0.7006	0.0053
	HL	46.4k	100			
	LH	100	6k	0.156	0.6281	0.0021
	HL	360k	2.2k			
FCK1-VMG-KLJN	LH	10k	10k	0	0.5028	0.0091
	HL	100k	1k			

Conclusion This study demonstrates that the duality approach of sampling currents at zero-voltage crossings is an effective method for detecting information leaks in non-equilibrium KLJN systems. The results corroborate Chamon and Kish's findings and provide further evidence that thermal equilibrium is crucial for maintaining unconditional security in KLJN key exchange protocols. This work emphasizes the importance of rigorous security analysis in cryptographic systems and highlights the need for caution when modifying established security protocols.

References

[1] G. Vadai, R. Mingesz, and Z. Gingl. "Generalized Kirchhoff-Law-Johnson-Noise (KLJN) Secure Key Exchange System using Arbitrary Resistors", Scientific Reports, vol. 5, 2015.
[2] C. Chamon and L.B. Kish. "Perspective–On the Thermodynamics of Perfect Unconditional Security", Applied Physics Letters, vol. 119, 2021, pp. 010501.
[3] S. Ferdous, C. Chamon, and L.B. Kish. "Comments on the 'Generalized' KLJN Key Exchanger with Arbitrary Resistors: Power, Impedance, Security", Fluctuation and Noise Letters, vol. 20, 2021, pp. 2150009.

Beyond Security: Leveraging Noise-Based Watermarking for Power Source Identification in Smart Grids

Robert Balog, Chanan Singh, Kate Davis, Laszlo B. Kish

Department of Electrical and Computer Engineering, Texas A&M University, College Station, TX 77843-3128, USA

Abstract: Our previous cryptanalyses of watermarked security in smart grids revealed that noise-based ("dynamic") watermarking cannot ensure unconditional security unless the communication within the grid system is itself unconditionally secure. This conclusion was supported by using a digital twin. We demonstrated a straightforward attack, inspired by the digital twin approach, which effectively compromised the security of dynamic watermarking without requiring knowledge of the private watermarking signal. The attacker could fully expose the grid while avoiding detection, even in the presence of internal grid noise. In this current work, we highlight a beneficial application of dynamic watermarking: identifying the sources of mixed power. This capability can be leveraged for practical purposes, such as billing.

Keywords: Smart grids; dynamic watermarking, power source identification.

Smart grid security [1-3] is important to maintain the confidentiality, integrity, and availability of smart grid infrastructures by preventing threats that can lead to business and operational disruptions. It involves safeguarding resources from unauthorized access, modifications, and ensuring the availability of the grid. Cybersecurity in the smart grid is essential due to the increased use of IT-based electric power systems, which increases cybersecurity vulnerabilities, leading to the need for resilient cybersecurity solutions. It is also important to protect smart grids against potential terrorist threats, espionage threats, and vulnerabilities caused by natural disasters, equipment failures, and user errors. The security of the smart grid involves ensuring that all risks are managed when things go wrong, making it a learning process and essential for the overall resilience of the smart grid. When supplier-managed demand response is employed, customer privacy and cybersecurity become crucial concerns for both the customer and the supplier. This is also true for the communication of meters to accountants.

In 2011, a novel technique, noise-based watermarking, known as Dynamic Watermarking (DW) was introduced [4] to protect the integrity of control systems within networked cyber-physical systems. Dynamic watermarking [4] in the context of smart grids involves the addition of continuous noise to the control system of the grid to enhance its security, see Figure 1.

Building upon our previous findings [5] that dynamic watermarking cannot offer unconditional security, we developed a simple yet effective attack [6]. Similar to the previous attack involving a digital twin [5], the new attack did not require knowledge of the private watermarking signal used by the grid controller. Due to the Controller's inability to detect the ongoing breach, the attacker could fully expose the grid.

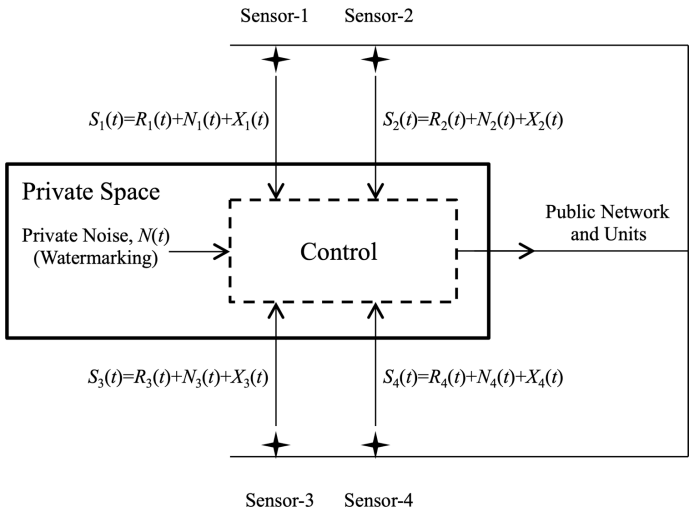

Fig. 1. Watermarking at the Controller; and its impact on the sensor signals. In the linear situation, the sensor signal $S_i(t)$ is the sum of the regular sensor signal $R_i(t)$ and the $N_i(t)$ which is the watermarking signal after linear operations. When nonlinearity cannot be neglected, the nonlinear component $X_i(t)$, including cross terms with the original sensor signal also appear. Note: in practical situations, nonlinearities should be negligible to avoid undesired interactions between the watermarking signal and the normal operation of the grid.

In this talk, after a brief survey of the active attack against dynamic watermarking [5,6], we introduce a beneficial application of dynamic watermarking: identifying the sources of mixed power by a cross-correlation technique. This capability can be leveraged for practical purposes, such as billing. Such a tool capable of identifying various power sources and their contributions in a mixed power situation within a smart grid can be highly valuable. It can help optimize energy distribution by accurately tracking the output of different sources, such as solar, wind, and traditional power plants, allowing for real-time adjustments to ensure efficient and reliable energy supply. This capability would facilitate better integration of renewable energy sources, reduce reliance on fossil fuels, and enhance grid resilience by predicting and managing power fluctuations more effectively. Additionally, such a tool could support dynamic pricing models and demand response systems, enabling consumers to adjust their energy usage based on the availability and cost of different power sources.

References

[1] K. R. Davis, K. L. Morrow, R. Bobba, E. Heine, Power flow cyber attacks and perturbation-based defense, in 2012 IEEE Third International Conference on Smart Grid Communications (SmartGridComm). IEEE (2012) 342–347.
[2] C. Singh, P. Jirutitijaroen, J. Mitra, "Electric Power Grid Reliability Evaluation: Models and Methods", IEEE Press, Wiley & Sons, New Jersey (2019).
[3] E. Gonzalez, L.B. Kish, R. Balog, P. Enjeti, "Information theoretically secure, enhanced Johnson noise based key distribution over the smart grid with switched filters", PLoS ONE 8 (2013) e70206.
[4] T. Huang, J. Ramos-Ruiz, W.-H. Ko, J. Kim, P. Enjeti, P. R. Kumar, and L. Xie, Enabling Secure Peer-to-Peer Energy Transactions Through Dynamic Watermarking in Electric Distribution Grids, IEEE Electrification Magazine 9 (2011) 55-64. DOI: 10.1109/MELE.2021.3093600.
[5] K. Davis, L. B. Kish, C. Singh, Smart Grids Secured by Dynamic Watermarking: How Secure?, Fluct. Noise Lett. 23 (2024) 2450043, DOI: 10.1142/S0219477524500433 .
[6] M. Yildirim, N. Kenarangui, R. Balog, L.B. Kish, C. Singh, "Simple Cracking of (Noise-Based) Dynamic Watermarking in Smart Grids", Fluct. Noise Lett. (2024) 2450059; DOI: 10.1142/S0219477524500597